Experimental and Simulation Study on the Improvement of Heat Transfer Coefficient Using Sintered Porous Materials

Santiago Galicia Edgar

電気通信大学

機械知能システム学専攻

A Dissertation
submitted to the Graduate School of Informatics and Engineering,
The University of Electro-Communications
in partial fulfillment of the requirements
for the degree of
Doctor of Philosophy
in
Engineering

Tokyo, Japan
January, 2022

Experimental and Simulation Study on the Improvement of Heat Transfer Coefficient Using Sintered Porous Materials

Examining Committee:

Supervisor:	Assoc. Prof. Enoki Koji
Members:	Prof. Okawa Tomio
	Assoc. Prof. Inoue Yohei
	Prof. Matuttis Hans-Georg
	Assoc. Prof. Mamori Hiroya
	Prof. Chiba Kazuhisa

To my uncles, Roberto Galicia Tulteca (Muñante) and Joel Galicia Tulteca (Chanfle), who always encouraged me to follow my dreams and unfortunately, they could not see this beautiful achievement in my life.

概要

金属繊維多孔質体を用いた熱伝達効率向上に関する実験およびシミュレーション研究

サンティアゴ　ガリシア　エドガー

多くの研究者は、過去20年間に熱流束を向上するための新しい技術を研究してきた。特に、金属繊維多孔質体の実装は、発泡点の密度を高め、壁面過熱度を減らし、より大きな直径の気泡の存在を増やすという特性があり、特に注目を集めている。熱流束を高めるための受動的方法として表面に取り付けられた焼結多孔質繊維を使用するサブクールは、ベア壁面と比較して２倍高い熱流束を有することが示されている。

この論文は、表面に付着した高気孔率焼結繊維の熱伝達とベア壁面の熱伝達を比較するための実験的研究を行うことを目的としている。蒸留水を使用したサブクールで、両方の壁面を加熱表面として使用した。流体入口のサブクール度、質量流束、および焼結銅の厚さをパラメータとして考慮した。高速度カメラを使用して、気泡の形成、気泡の直径、および気泡の発生率を視覚化して記録した。熱流束を比べるために、4つの異なる金属繊維多孔質体の厚さ（0.2、0.5、1、および　2 mm）とベア壁面0 mmを作成した。

本論文は、あらゆる機械機器に搭載される熱交換器の高性能化の一案として、三菱マテリアル株式会社中央研究所との共同研究により、申請人が独自に取得した実験的および計算的結果を主としてまとめている。熱交換器の高性能化の中でも、いかに高い熱流束を低い伝熱面温度で除去できるかが重要な設計パラメータとなり、そして限界熱流束CHFの向上を目指す必要があった。そこで、本博士論文では、数百マイクロメートルオーダーの金属繊維で構成される多孔質体を伝熱面に取り付けた場合の、サブクール沸騰熱伝達メカニズム特性について実験的に調べ、そして、通常は非常に難しい金属繊維多孔質体の数値シミュレーションモデルを構築したもので全6章から構成される。　第1章は序論、第2章は過去に実施されてきた論文をまとめ、従来の問題点と今回の提案提案手法の違いおよび優位性を論理的に記述している。第3章は実験装置について説明している。　第4章では、矩形流路で、下面からのみの加熱に対する実験的結果をまとめている。矩形流路で下面からの加熱は実機では、例えば応用先として電気自動車などの電池やインバータ冷却など広く使用されるもので、これらの熱交換器の高性能化は必須である。そこで、下面の伝熱面加熱部に、通常のベアを基準として実験を行い、金属多孔質体の高さをパラメータとし、0.2mm、0.5mm、1.0mm、2.0mmで空隙率86％において実験的研究を実施した結果を

まとめている。この結果、全ての条件で、0.2mmと0.5mmの充填高さが高性能であり、それ以上の充填高さでは、逆に伝熱が悪くなることを明らかにした。また、実験では液単相の場合とサブクール沸騰熱伝達の場合で実験を行っているが、特にサブクール沸騰熱伝達は可視化が可能であるため、高速度カメラによって伝熱が良好になるメカニズムと劣化するメカニズムをそれぞれ検証している。　第5章では、金属繊維多孔質体の数値シミュレーションを実施し、その結果を示した。金属繊維多孔質体の数値シミュレーションは非常に難しいとされていて、これまでにこのような数値シミュレーションは世界的に実施しようと試みた形跡はあるものの、実験結果をお再現するに至っていない。そこで、円管内に金属繊維多孔質体を25mm充填したのCTスキャンモデルがあったため、手始めにこのCTスキャンを数値シミュレーション解析ソフトに入力した結果、定量的にも定性的にも実験結果と良い一致を示し、200℃の乾燥空気が空気流速によって出口温度が上昇する様子を再現したことを明らかにしている。

第6章は全体のまとめと今後の展望である。

Abstract

Many researchers have studied new technologies to enhance the heat flux in the last two decades. In particular, the implementation of porous materials has attracted special attention due to their characteristics to increase the nucleation sites density, reduce the wall superheat, and increase the bubble generation and depature rate. In particular, the subcooled flow boiling using high-porosity sintered fibers attached to a surface as a passive method to enhance the heat flux has been shown to have a heat flux which is higher by a factor of two compared to the bare surface.

This thesis aims to conduct an experimental study to compare the heat transfer of high-porosity sintered fibers attached to the surface and the heat transfer on the bare surface. Both surfaces were used as heating surface, under subcooled flow boiling using distilled water as the working fluid. Inlet subcooled temperature, mass flux, and thickness of the copper porous layer thickness were considered as parameters. Bubble formation, bubble diameter, and bubble departure rate were visualized and recorded using a high-speed camera. For this purpose, four different thickness of the porous layer (0.2, 0.5, 1, and 2 mm) and a bare surface (0 mm) were considered.

The effects of the high-porosity sintered fibers attached to the surface were discussed after analyzing the results of all the porous thicknesses. The bubble formation mechanism was also recorded and discussed for single-phase and two-phase flow boiling. The results showed an enhancement in the heat flux and a reduction in the wall superheat temperature when the porous body was used as the heating surface. The mass flux also plays an essential role in the Onset Nucleate Boiling (ONB) point, shifting the ONB to a higher wall superheat temperature at higher mass fluxes. In addition, at higher inlet subcooling degree the Critical Heat Flux (CHF) was reached at lower heat fluxes.

It is also essential to describe the effects of the oxidation of the copper surface where an oxidation layer was formed which covers the nucleation sites. Thus, the oxidation layer

promoted a deterioration of the heat flux and increased the wall superheat temperature by around 27%.

In addition to the experimental research, a simulation analysis using the computational fluid dynamics (CFD) software "STREAM" was performed to validate and confirm the heat flux enhancement using the high-porosity sintered fibers.

The present thesis is structured as follows: Chapter 1 introduces an overview of the heat boiling methods, definition, and characteristics. Secondly, Chapter 2 presents a general literature review of the passive methods and techniques to enhance the heat flux. In Chapter 3, the experimental setup, test loop, materials, and procedure are presented. In addition, the characteristics of the high-porosity sintered fibers made of copper are explained. In Chapter 4 the experimental results of the heat flux enhancement using the high-porosity sintered fibers in the single-phase and two-phase subcooled flow boiling. Chapter 5 presents the results obtained on the CFD simulation on the single-phase using the porous materials on a full-filled heat tube. Finally a summary of the outcome and discussion presented in previous chapters, as well as future direction of the current research, are presented in Chapter 6.

Contents

List of Figures

List of Tables

List of notations

List of Acronyms

BHT	Boiling Heat Transfer
CHF	Critical Heat Flux
CTS	Computed Tomography Scan
DNS	Direct Numerical Simulation
FDB	Fully Developed Boiling
FEM	Finite Element Method
MHF	Minimum Heat Flux
NVG	Net Vapor Generation
ONB	Onset Nucleate Boiling
CFD	Computational Fluid Dynamics

Greek Symbols

λ_l	Liquid thermal conductivity [W·m^{-1}·K^{-1}]
μ_l	Liquid viscosity [Pa·s]
ρ_g	Vapor density [kg·m^{-3}]
ρ_l	Liquid density [kg·m^{-3}]
σ	Surface tension [N·m^{-1}]
ϕ	Correlation factor [-]
β	Ratio of channel height to channel width [-]
ΔP_{sat}	Saturation pressure difference[KPa]
ΔT_{sat}	Wall superheat temperature[K]
ΔT_{sub}	Subcooled temperature[K]

List of Symbols

Bo	Boiling number [-]
$c_{p,l}$	Liquid specific heat at constant pressure [J·kg^{-1}· K^{-1}]
d	Diameter [m]
d_h	Hydraulic Diameter [m]
G	Mass flux [kg·m^{-2}·s^{-1}]
h	Heat transfer coefficient [W·m^{-2}·K^{-1}]
h_{fc}	Forced convection heat transfer coefficient [W·m^{-2}·K^{-1}]
h_{lg}	Enthalpy of vaporization latent heat [J·kg^{-1}]
h_{nb}	Nucleate boiling heat transfer coefficient [W·m^{-2}·K^{-1}]
Ja	Jacob number [-]
l	Distance [m]
Nu	Nusselt number [-]
Nu_{fc}	Forced convection Nusselt number [-]
Nu_{nb}	Nucleate boiling Nusselt number [-]
S	Suppression factor [-]
P	Pressure [KPa]
Pr	Prandtl number [-]
Pt	Thickness of the porous layer [mm]
q	Heat flux [kW·m^{-2}]
q_t	Total heat flux [kW·m^{-2}]
q_{fc}	Forced convection heat flux [kW·m^{-2}]
q_{nb}	Nucleated boiling heat flux [kW·m^{-2}]
q_w	Wall heat flux [kW·m^{-2}·]
Ra	Roughness [μ m]
Re	Reynolds number [-]
Re_l	Liquid Reynolds number [-]
T	Temperature [K]
T_b	Bulk temperature [K]
T_s	Saturation temperature [K]
T_w	Wall temperature [K]
u_l	Liquid velocity [m·m^{-1}]
V	Volume [m^3]
We	Weber number [-]

Acknowledgements

First of all, I would like to express my sincere appreciation to my parents Adela Galicia Tulteca and Jose Santiago Vazquez, for all the unconditional support and love that helped me to pursue all my dreams.

I want to express my deepest gratitude to my supervisor Prof. Koji Enoki for receiving me in his laboratory as a short term exchange student, for offering me the option to come back to Japan as a Ph.D. student, for his excellent advice, all the guidance, and the shared experiences. Without his support emotionally and inspiration, this dissertation would not be possible.

To Prof. Okawa and his laboratory for offering me a place in his laboratory in collaboration with Prof. Enoki. To my lab mates Junki Ohashi, Kesuke Kumatori, and Yusuke Otomo for helping me with the experiments and the data analysis. To Yuto Katagi for helping me with the simulation study. To Ren Watanabe for the shared data of his experimental research.

I want to express a special dedication to Yurie Watanabe for all her love and support. I want to thank her for the financial and emotional support when I needed. She is part of the inspiration and part of this dream in Japan.

To my sister Maricela and my brother Jose who always listened to me and share me the recent news in Mexico regardless of the different time zone. To all my family in general.

To all my friends in Japan who always offered me a great time, for the times when we drank a coffee or a beer, for all their advice and tips. Especially to Edgar, Jairo, and Julio for all the support as *senpai*.

I also want to express my gratitude to Prof. Suwako Uehara and Prof. C.K Choo for offering me a chance to work with them in a part-time job at the university.

I am deeply grateful to Mr. Takeo Kanazawa for all his experiences he shared with me, for all the invitations to meet new people and for teaching me the importance of social relations.

Also, for encouraging me to come back to Japan.

I would like to thank Prof. Mariko Nakano from the National Polytechnic Institute (Mexico) for the information and guidance to receive a scholarship to study in Japan.

I want to thank the Inner trip foundation from which I received economic support in the last year of the doctoral program, also for all the monthly meetings, the lunch and coffee time, where we shared experiences and ideas.

Moreover, last but not least, I would like to express my gratitude to Mr. Toshihiko Saiwai, Mr. Kenji Takita, Mr. Kenji Orito, members of the Central Research Institute, Mitsubishi Materials Co., Ltd. for all the support on the fabrication of the high-porosity sintered fibers, and the data analysis to make possible this research.

1

Introduction

1.1 Background

It is widely known that subcooled flow boiling is characterized by high heat flux dissipation at low wall superheat temperature, which is necessary for high-performance cooling systems in diverse engineering processes such as nuclear plants, micro- and nano processors as well as rocket engines etc. which reach heat fluxes of around 2.5 $MW \cdot m^{-2}$. In particular, flow boiling allows a higher heat transfer rate than pool boiling due to the forced convection effect [1–4]. Flow boiling is discriminated into subcooled flow boiling and saturated flow boiling, where the subcooled flow boiling is characterized by a lower working fluid temperature than its saturation temperature. The combination of solid and fluids has a direct impact on the amount of heat transferred from the body to the fluid. The properties of the solid and the fluids have been studied for several years, and nowadays, one of the most common combinations for the design of cooling systems is copper-water. Copper offers a high thermal conductivity, relatively low specific heat, and relatively easy malleability. However, the combination of copper-water is susceptible to oxidation effects. The thermal properties also suffer degradation due to several physical phenomena during the boiling process on the copper surface, such as erosion, corrosion, and mainly oxidation [5–8].

In recent years researchers have developed new porous materials to enhance the heat flux in the cooling systems using water as the working fluid. An increase of the heat flux by a factor of two was reported when porous material was used instead of the bare surface. This enhancement is attributed to the activation of a higher number of nucleation sites, higher permeability, wettability, water supply, as well as higher formation and departure rate of the bubbles. However, the governing phenomena are not yet well understood, and the mechanism of the flow boiling using porous materials is still under discussion [9–11].

1.2 An overview of micro porous materials

The origin of the first use of metal porous materials (also known as foam metals) is uncertain; however, it is well known that ancient civilizations as the Egyptians started to use porous materials. They used porous clay pots to cool water. They filled the porous clay pots with water and exposed them to the cold night wind flow, promoting the cooling process through the pot pores. After some centuries, the walls of the houses were built from block bricks, which are highly porous. It was perceived that the temperature inside the house was different from the outside temperature. Also, they used charcoal as a porous medium to remove impurities in the water by filtration [12]. During the mid-20^{th} century the development of more sophisticated microscopes allowed a deeper study of the porous materials. They permitted the visualization of the micro and nano characteristics. Material structures like the density, porosity, adsorption, absorption, heat transfer coefficient etc. could be manipulated. As shown in Figure 1.1, microporous materials consist of a rigid frame with internal holes, keeping the physical and mechanical arrangement rigid [13–17, 19]. The porous surfaces increase the surface area and activate more nucleation sites. The porous matrix can be made by the same material as the surface or a different one, and is classified according to the machining process. Lin et al. [20] classified the fabrication of the porous materials as follows:

- Sintering: Consists of preparing of a powder of the material mixed with some lubricants or different chemical agents. The next step is to compact to the powder under high pressure and temperature. As a result of this sintering, surfaces of the grains are fused together.

- Spray coating: Small particles are sprayed onto a surface, creating a coating. A heat source is needed to melt the particles and the type of spray coating is classified according to the melting method: Combustion flame, electric discharge, beams, kinetic energy, etc.

- Electrochemical deposition: Created by the electrolysis between a solution and a metal surface. It is a simpler and cheaper method than sintering and spray coating. The parameters that affect the porous formation are the direct current density, the temperature, and the pH of the solution.

- Chemical vapor deposition: Coated surfaces are exposed to diverse chemical solutions

that promote the deposition of particles on the surface. Usually, chemical vapor deposition is combined with other methods.

- Additive machining: Recently developed and also know as 3D printing. The porosity and the dimension of the pores are easy to manipulate; however, the variety of materials than can be used are limited.

In particular, the microporous materials reduce the thermal resistance on the contact surface if they are sintered on the same material. High-porosity sintered fibers are a body with small internal holes and are classified according to the connectivity of internal holes. Porous materials are called *through-hole* if the internal holes are interconnected. If the internal holes are not interconnected, they are termed *closed-holes*. The microporous materials cover a wide range of applications as passive units in the environmental control, biology, medicine, chemical industry, mechanical and electrical industry, etc. Some typical applications to enhance certain operations are:

- Purification of gases in combustion processes, particularly on automobile emission gases.
- Chemical applications, particularly in the substitution of ceramic materials.
- Enhancement of the microreactors and the use of microelectronic systems.
- Use in cooling systems to enhance the heat transfer process.

Nowadays, new passive technologies to enhance the heat exchangers' performance, such as porous materials, have attracted researchers around the globe. In the last two decades, researchers have reported an improvement in the flow boiling heat flux using microporous materials between 20% and 200% compared to bare or untreated surfaces. The use of porous surface materials increases the heat flux compared to the bare surface, and offers a variety of thermal and cooling applications, including but not limited to computer cooling systems, air conditioners, refrigeration systems, and heat pumps. On the other hand, and despite the effort of researchers, the governing phenomena of subcooled flow boiling are still under investigation, and the discrepancies in the literature are also a subject of discussion.

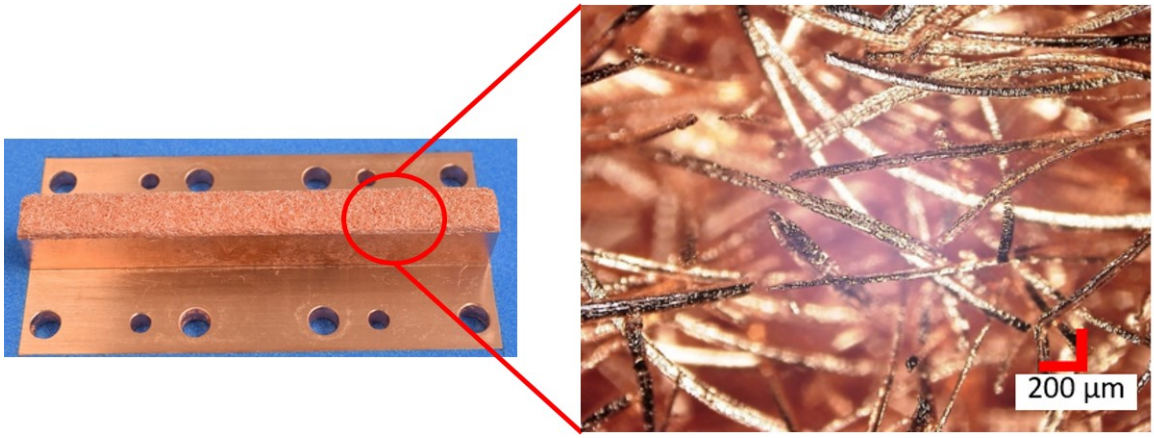

Figure 1.1: Microscopic view (100x) of the high-porosity sintered fibers.

1.3 Aim and scope of the study

This thesis presents the experimental results of the subcooled flow boiling heat flux using high-porosity sintered fibers made of copper attached to the surface. The present research aims to contribute to a better understanding on the physical and thermal phenomena of flow boiling heat flux using high-porosity sintered fibers attached to the heating surface, the effect of the porous thickness on the single-phase and two-phase region, and the relation with the wall superheat temperature. To minimize the effects of external agents on the boiling phenomena, deionized water was used as the working fluid. The effects of the mass flux G (200, 400, 600 [kg·m^{-2}·s^{-1}]) and the inlet subcooling temperature ΔT_{sub} (70, 50, 30 K) are also discussed. To analyze the effect of the porous body, four different thickness of the porous layer (0.2, 0.5, 1, and 2 mm) were tested, in addition to one bare surface (0 mm porous thickness). Bubble and horizontal flow patterns are recorded and analyzed using a high-speed camera. Furthermore, a deeper analysis of the bubble influence is also discussed.

Experimental research is needed to determine the relationship between the thickness of the porous layer, subcooled temperature, mass flux, heat flux, and wall superheat temperature to design modern cooling systems with passive technologies to enhance the amount of heat transferred from a solid to the working fluid. In addition, a computational fluid simulation was performed to confirm the enhancement of the heat transfer phenomena in the single-phase regime using the high-porosity sintered fibers.

2

Literature review

The heat transfer is the phenomenon where thermal energy is transferred from one body to another body due to a spatial temperature difference. Already the primitive man understood that the energy transfer is unidirectional, from the system with higher energy to the system with lower energy, this fact promoted the control of the most important energy source, the fire. Several years later the concept of temperature was established and defined as a property of all the bodies regardless of the mechanical conditions. The next important step in the development of humanity was the first commercially successful steam engine in 1712. Thus the development of cooling systems and heat exchangers were as necessary as the thermal engines. [21, 22]

2.1 Fundamentals of boiling

Boiling heat transfer is defined as a process between solid and liquids where a liquid phase change occurs due to an increment in the solid body temperature. As a consequence, the amount of heat flux from the solid to the liquid phase also increases. In general, the heat flux from a solid surface to a liquid increases with the temperature difference between the liquid and the solid. However, after a specific limit on the temperature difference is reached, the heat flux will decrease regardless of increases in the temperature difference. In 1934, Shiro Nukiyama conducted experimental research on the amount of heat transmitted from a heated metal to boiling water at atmospheric pressure. Nukiyama introduced the concept of the boiling curve, which is a plotted relation between the wall superheat temperature and the heat flux. He was the first to identify and propose the concept of 'Critical Heat Flux'(CHF) and also proposed the existence of a minimum heat flux point. The maximum point of heat flux is at the CHF; beyond the CHF point, the heat flux is reduced significantly, the wall superheat temperature increases abruptly, and it may cause damage to the heating

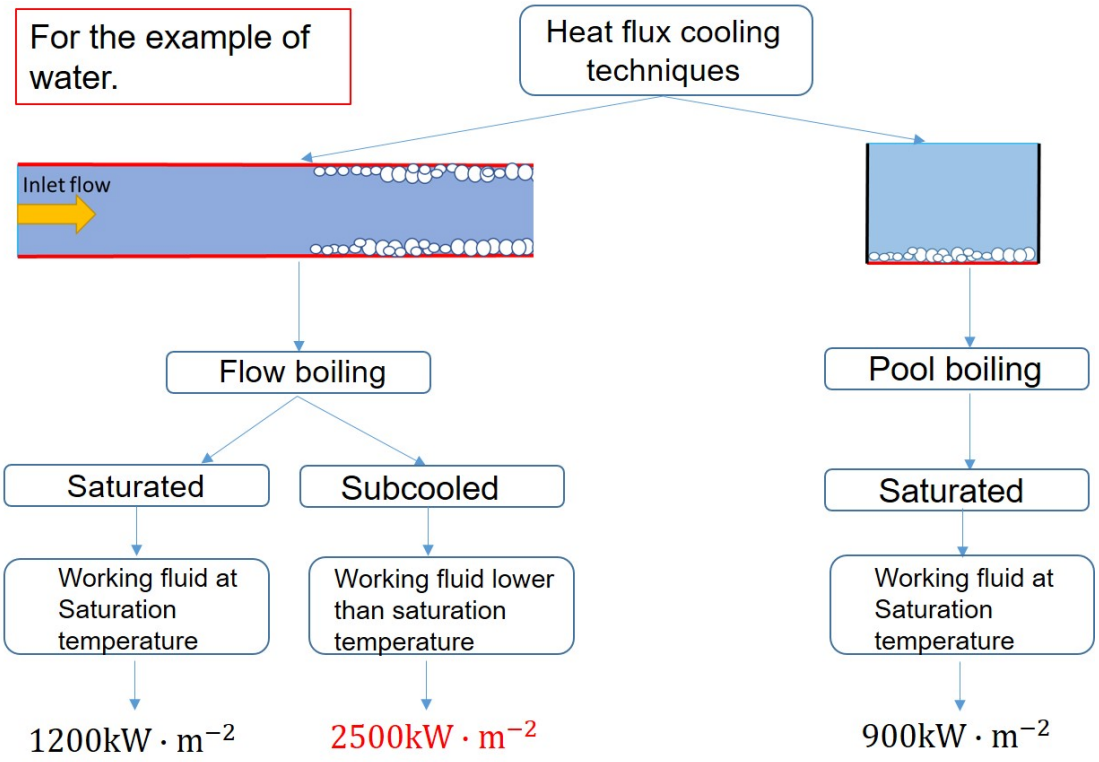

Figure 2.1: Cooling techniques; maximum heat flux reported of water as working fluid.

surface. [23]

The boiling is divided into two main categories: pool boiling, where a liquid is in a container, and the heat transfer between the heating surface and the liquid is due solely to free convection; on the other hand, the flow boiling is defined as confined fluids in pipes with an internal fluid moving through the pipes, where the heat transfer is due to the forced convection. In addition, pool boiling or flow boiling can be combined with subcooled or saturated flow. Subcooled flow occurs in a fluid with a bulk temperature lower than its saturation temperature; contrarily, the saturated flow has a bulk temperature higher than its saturation temperature. Subcooled flow boiling shows a higher heat transfer rate than pool boiling; due to this fact, subcooled flow boiling is commonly used in diverse engineering applications due to its high heat transfer promoted by the bubble dynamics and forced convection. Figure 2.1 shows the difference between the flow and pool boiling, for the particular case of water as working fluid. Here is noticeable the higher heat flux on the subcooled flow boiling. However, since flow boiling involves a phase change as well as boiling and condensation, the influence due to the latent heat h_{fg}, the surface tension σ, and the density ρ of each of the two phases need to be considered for the heat transfer process [24–28].

Some researchers have developed correlations to predict the subcooled flow boiling heat flux. These correlations consider the flow velocity, surface roughness, inner diameter, inlet subcooling temperature, etc [29, 30]. In particular, the surface roughness, micro porous channels, surface modifications, etc. are considered as a passive methods to increase the heat flux. Scratches, roughness, or cavities (also called nucleation sites) affect the heat transfer performance directly. The nucleation sites promote the bubble formation and departure rate, the water supply ability, and also increase the wetted area. This ability to increase the heat transfer performance has been studied by several researchers in the last decades; they proposed techniques such as rough surfaces, treated surfaces, extended surfaces, displaced enhancement devices, swirl flow devices, coiled tubes, surface tension devices, and porous surfaces, etc. The increase in the heat flux was reported to be between 20% and 200% in comparison with non treated (bare) surfaces [29, 31–33].

The thermophysical properties of the working fluid have a direct influence on the heat flux and the CHF; at a higher subcooling temperature, the CHF increases linearly, and also the pressure on the system increases [34]. Subcooled flow boiling using water as working fluid and copper for the heating surface is one of the most common combinations of heat exchangers and cooling systems due to the high heat transfer of this fluid-solid combination. Figure 2.2 shows the heat transfer coefficient of the most common working fluid of the cooling systems. The two-phase heat transfer coefficient is higher than the single-phase for all the working fluids. Water is often used as working fluid due to its high heat transfer coefficient range. The best performance on the cooling systems is the point called “hook back” by many researchers. This point consists in an increase of the heat flux, and a reduction of the wall superheat temperature at high heat fluxes. This phenomenon is usually observed on porous coating surfaces due to the increase of the bubble departure rate, the increased bubble diameter, and also the higher nucleation density [35].

An enhancement of the heat flux using sintered metal fibers attached to the surface and a reduction of the wall superheat was reported compared to the bare surface, also, a minor variation in the wall temperature was found for porous surfaces. This fact allows to design more compact, lightweight, and more efficient cooling systems [36,37]. However, the influence of the sintered fibers on the single-phase heat transfer is almost marginal due to the absence of bubbles, and nucleation sites are not activated in the single-phase region. In addition, the oxide deposits on the copper surface also need to be considered in the design of cooling

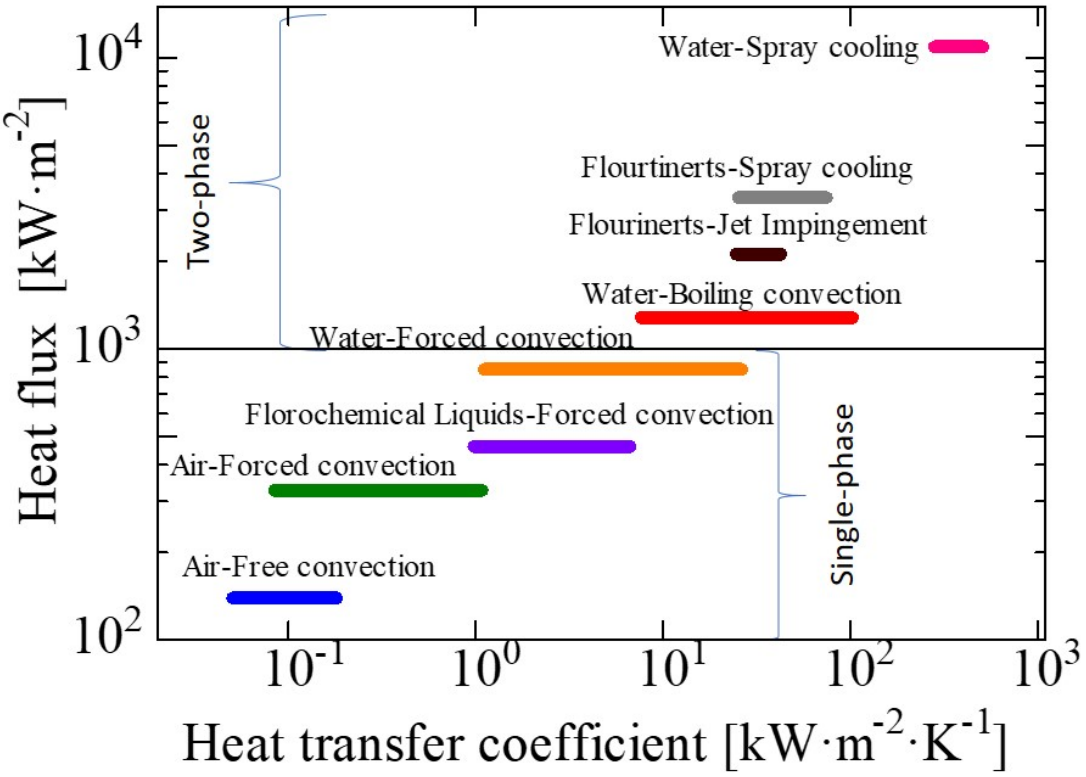

Figure 2.2: Heat transfer coefficient of the most common working fluids in cooling systems.

systems.

The boiling phenomena need to be analyzed under two-phase fluids, which means that the working fluid characteristics for the liquid and the vapor state need to be considered. As mentioned in Chapter 1, the boiling processes can be classified into different types, and it is necessary to understand the limitation points in the boiling curve. The literature review presented in this chapter shall explain the parameters that influence the boiling process.

2.2 Thermal analysis of the porous media

When a fluid, regardless of its state (liquid or gas), enters a porous body, this body is called saturated medium; on the other hand, if the three phases coexist, it is called non-saturated porous medium. Consider a saturated porous medium with a temperature T_1 at $x = 0$ and a second temperature T_2 at $x = L$, and $T_1 \geq T_2$. The heat flux can be calculated as

$$q = \frac{k_{eff} A}{L}(T_1 - T_2), \tag{2.1}$$

$$k_{eff} = \frac{1}{(1-\varepsilon)/k_s + \varepsilon/k_f}, \tag{2.2}$$

where k_{eff} is defined as the effective thermal conductivity coefficient and can be calculated with the equation (2.2). The porosity ε and the thermal conductivity coefficient of each phase determine the k_{eff}. Also, it must be considered that $k_s > k_f$, where k_s and k_f are the thermal conductivity of the solid and the fluid respectively.

Equation (2.1) can be applied to moving fluids if radiation effects can be neglected. Substituting equation (2.1) into equation (2.2), the expression is arranged into

$$q = \frac{A\Delta T}{(1-\varepsilon)L/k_s + \varepsilon L/k_f}. \tag{2.3}$$

2.3 Nucleation sites

The main advantage of nucleation boiling is the high heat flux that the process can reach and the relative low wall superheat temperature. This phenomenon is attributed to the formation, growth, detachment, coalescence, and collapse of bubbles. In general terms, the heated surface area where bubbles are generated is known as a nucleation site. It was found that the nucleation site density is enhanced by imperfections, scratches, cavities, pits, or grooves on the surface as sketched in Figure 2.3. In general, all of these imperfections are called cavities, and their main characteristic is the ability to trap vapor bubbles and promote the generation of bubbles. The form, size, and quantity of the nucleation sites determine the bubble contact angle and the bubble size. Nowadays, new techniques such as mechanic agitation and superficial vibration are used to promote bubble formation. However, these techniques are challenging to implement and also represent a waste of energy on the cooling systems because they need an extra energy source. Due to this reason, passive techniques such as surface modification or use of porous materials are the most common methods to enhance the number of nucleation sites [33, 36–38].

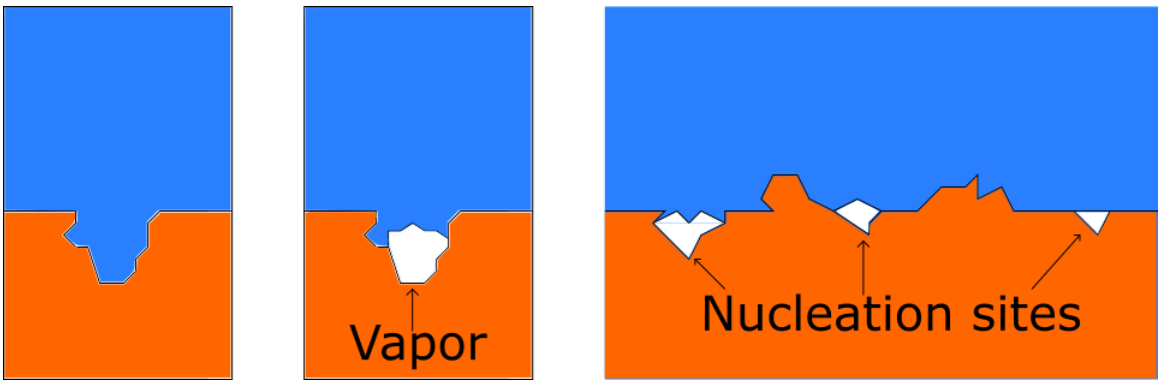

Figure 2.3: Sketch of the nucleation sites on a heating surface.

2.4 The boiling curve

In thermodynamics, it is well known that the amount of heat transferred from a body to another body is directly proportional to the temperature difference between them. This can be expressed by

$$Q \propto (\Delta T). \tag{2.4}$$

However, in the case of two-phase flow it is necessary to carry out an additional analysis of the boiling curve. It was in 1934 when Shiro Nukiyama published his revolutionary research where the maximum and minimum heat transmitted were defined [23]. Nukiyama implemented a saturated water pool boiling with a metal wire as heating surface; he found that the amount of heat q transferred from the metal to the water increases proportionally to the wall superheat temperature ΔT_{sat}. However, after ΔT_{sat} reaches a certain limit, the amount q of transferred heat decreases considerably, regardless of whether ΔT_{sat} continues to increase. Then, the amount q of transferred heat will reach the minimum heat flux at a certain ΔT_{sat}; Beyond this point, the effects of the radiation become more significant, and the heat flux will increase again. As shown in Figure 2.4, the boiling curve with the CHF and the MHF are a consequence of the bubble activity.

Nukiyama also found that the bubble formation was evidence of the boiling process; however, the bubbles were observed at a the wall superheat temperature $\Delta T_{sat} \approx 5°\text{C}$ where discrete bubbles could be identified. It is necessary to clarify that the boiling curve is similar in this case of the flow boiling and pool boiling.

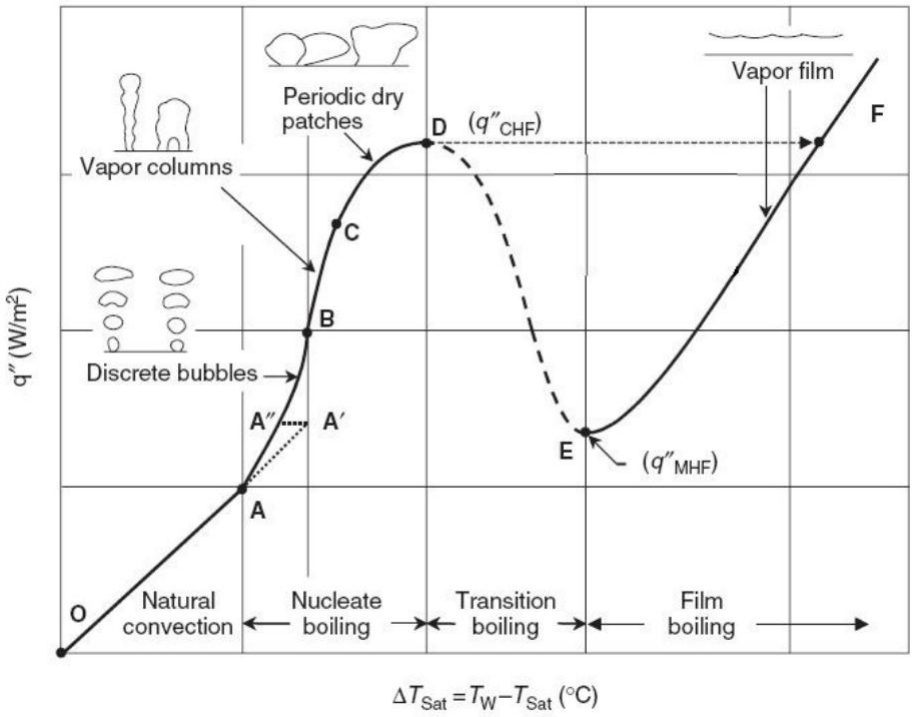

Figure 2.4: Nukiyama boiling curve [18].

2.4.1 Natural convection

Referring to the boiling curve in Figure 2.4, we can figure out that the part played by natural convection that is present when $\Delta T_{sat} \leq \Delta T_{sat,A}$ where $\Delta T_{sat,A}$ is the point where the bubbles are constantly formed. This point is also known as Onset Nucleated Boiling (ONB). Before ONB, there is no bubble generation, and the heat flux is only due to natural convection. In free convection, the heat transfer analysis can be done as for natural convection; thus, if the flow is laminar or turbulent, the heat transfer coefficient h will change as ΔT_{sat} changes [28]. Considering an internal flow before the ONB the heat flux is mainly caused by the forced convection and it is defined as the equation (2.5)

$$q_{fc} = h_{fc}(T_w - T_b), \tag{2.5}$$

where the forced convection heat transfer coefficient h_{fc} is determined by the Dittus-Boelter equation [39] for the convective Nusselt number

$$Nu_{fc} = \frac{h_{fc} d_h}{\lambda_l} = 0.023 Re_l^{0.8} Pr_l^{0.4}, \tag{2.6}$$

with the Reynolds number Re

$$Re_l = \frac{\rho_l u_l d_h}{\mu_l}, \tag{2.7}$$

where the ρ_l is the density of the liquid, u_l is the bulk velocity, and μ_l is the kinetic viscosity and all of them are evaluated at the bulk temperature. d_h represents the hydraulic diameter. The Prandtl number

$$Pr_l = \frac{\mu_l c_{p,l}}{\lambda_l}, \tag{2.8}$$

where the $c_{p,l}$ is the specific heat at constant pressure and λ_l represents the liquid thermal conductivity.

2.4.2 Nucleate boiling

This second region of the boiling curve (Figure 2.4) is called nucleated boiling. In this region between point B and C on the boiling curve, the bubbles start to coalesce to vapor columns. The bubble activity becomes more vigorous and the formation and departure rate also increases. As a result, periodic dry patches occur on the heated surface, and finally the CHF is reached due to the reduction of the fluid supply. The region of nucleate boiling occurs for $\Delta T_{sat,A} \leq \Delta T_{sat} \leq \Delta T_{sat,D}$, where $\Delta T_{sat,D}$ is the wall superheat temperature corresponding to the CHF. In the nucleate boiling region, the number of bubbles generated is determined by the number of active nucleation sites, and eventually, the bubble formation rate and coalescence will increase as ΔT_{sat} increases as shown in the Figure 2.5. Up to this point, the equation (2.4) is verified. In addition, the Nusselt number also depends on the combination between solid-surface and fluid. C_{sf} is a constant that depends on the material combination for solid and fluid independent of the surface geometry. For the particular combination water with polished copper, C_{sf} has a value of approximately of 0.0128. For the case of the non-polished copper, C_{sf} is around 0.0068 [40]. Thus the Nusselt number is

$$Nu = C_{sf} RePr. \tag{2.9}$$

The amount of heat flux is determined by the nucleate boiling heat transfer coefficient, and the wall superheat temperature is

$$q_{nb} = h_{nb}(T_w - T_s). \tag{2.10}$$

The nucleate boiling heat transfer is

$$h_{nb} = 0.00122 \frac{\lambda_l^{0.79} c_{p,l}^{0.45} \rho_l^{0.49}}{\sigma^{0.5} \mu_l^{0.29} h_{lg}^{0.24} \rho_g^{0.24}} \Delta T_s^{0.25} \Delta P_s^{0.25}. \tag{2.11}$$

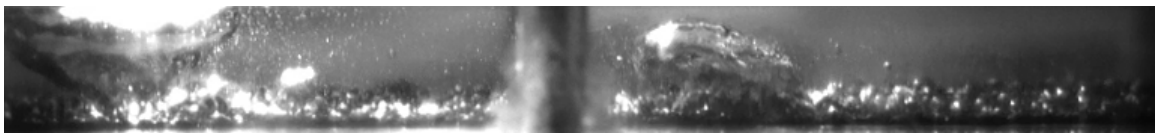

Figure 2.5: Bubble formation on the nucleate boiling regimen.

2.4.3 Critical heat flux

CHF refers to the maximum heat flux on the boiling curve (Figure 2.4). The CHF point is characterized by the rapid formation of bubbles, where a vapor film covers most of the heating area and therefore the working fluid supply ability is reduced. Thus a significant and a constant vapor blanket (also called dry patch or dry out) can be detected at this point, as shown in Figure 2.6. Due to the many influencing variables in two-phase flow like the bubble activity, working fluid motion, wettability, contact angle, capillary, etc., it is difficult to determine the CHF accurately. However, several researchers have reported correlations that can predict the CHF. Katto and Kurata [41] proposed an equation to predict the maximum heat transfer with

$$q_{chf} = 0.186 G h_{lg} \left[\frac{\rho_g}{\rho_l}\right]^{0.559} \left[\frac{\sigma \rho_l}{G^2 L}\right]^{0.264}, \tag{2.12}$$

where the G is the mass flux, L is the length of the heated surface, and h_{lg} corresponds to the enthalpy of vaporization.

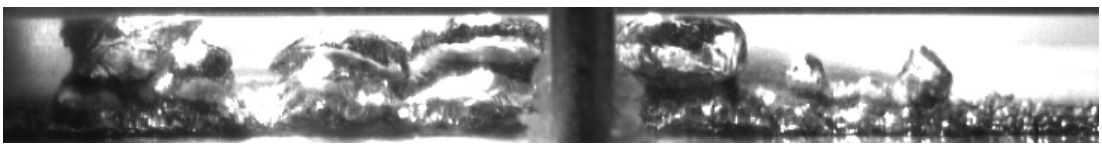

Figure 2.6: Bubble formation on the critical heat flux.

2.4.4 Transition boiling

This region of the boiling curve is characterized by the formation of a vapor blanket that covers the heating area, reducing the fluid supply while the vapor blanket performs thermal insulation as shown in Figure 2.7. Thus the heat transfer coefficient also is reduced, and the amount of heat flux will reduce as ΔT_{sat} increases. The range is $\Delta T_{sat,D} \leq \Delta T_{sat} \leq \Delta T_{sat,E}$, where $\Delta T_{sat,E}$ is the minimum heat flux, explained in section 2.4.5. The transition boiling regime is avoided in practical engineering applications due to its high instability and high wall superheat temperature operations.

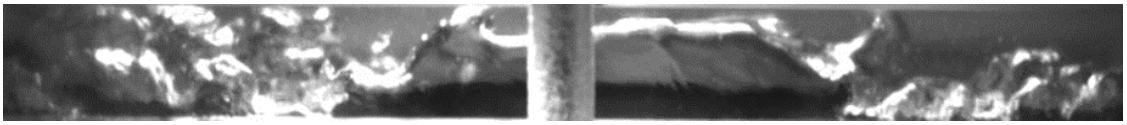

Figure 2.7: Bubble formation on the transition boiling

2.4.5 Minimum heat flux

Also known as the Leidenfrost point, this is the point on the boiling curve where the minimum heat is found. It is located just behind transition boiling, and it is characterized by the formation of a constant vapor blanket. In 1958 Zuber [42] established a correlation to predict the minimum heat flux on a long horizontal plate with

$$q_{min} = C p_v \rho_g h_g \left[\frac{g\sigma(\rho_l - \rho_g)}{(\rho_l + \rho_g)^2} \right]^{1/4}, \tag{2.13}$$

where the properties are evaluated at saturation temperature, and the constant $C \approx 0.09$ was determined experimental by Berenson [43] for pool boiling.

2.4.6 Film boiling

As mention in section 2.4.5 on the MHF, when the vapor blanket already covers the heating surface, the heat transfer by conduction and radiation becomes more significant, and thus the heat flux increases again with the increment of the wall superheat temperature. This effect leads to the inflection point on the boiling curve in Figure 2.4. This effect was observed by Leidenfrost in 1756 [44], and occurs in the range of $\Delta T_{sat} \geq \Delta T_E$.

2.5 Internal flow boiling

If the fluid which flows through the inlet of a heated pipe is in a state of internal flow boiling, there is no opening where the vapor could escape, and as a consequence, the liquid and the vapor are forced to flow together. In this case, is necessary to consider two-phase flow.

Let us consider an internal flow with an inlet subcooling temperature (for flow boiling T_b) lower than its saturation temperature $T_b < T_{sat}$. It is possible to analyze the heat transfer using the forced convection correlations for single-phase flow. The state of subcooled liquid could be defined as the equilibrium quality. Kandlikar [24] proposed the equation to calculate the quality x. In general terms, subcooled flow boiling is characterized by the bubble rate generation, in other words, an equilibrium called 'quality' is defined as

$$x = \frac{(h_l - h_{l,sat})}{h_{lg}} = \frac{-c_p \Delta T_{sub}}{h_{lg}}. \tag{2.14}$$

Before the bubble formation, subcooled flow does not contain any bubbles or vapor. Thus, considering the wall temperature and the liquid temperature the heat transfer rate can be expressed as

$$q = h_l(T_w - T_b) = h_l(\Delta T_{sat} + \Delta T_{sub}), \tag{2.15}$$

considering the wall temperature T_w and the bulk temperature T_b of the liquid.

As the fluid flows further inside the pipe, the bubble activity increases, and also the fluid temperature increases. After the ONB, the point called fully developed boiling (FDB) is reached. Here the heat trasnfer is a combination of the nucleate and the forced convection modes. When the subcooling temperature reaches the saturation temperature, the net vapor generation (NVG) sets in. NVG is characterized by a high-temperature gradient and the formation of vapor bubbles near to the heating area as shown in Figure 2.8.

As mention in section 2.4, the boiling curve plotted for flow boiling is similar to the pool boiling; however the ONB is shifted to a higher wall superheat temperature due to the flow effects. Several researchers have reported a higher CHF for the subcooled flow boiling. [28, 36–38, 45–47].

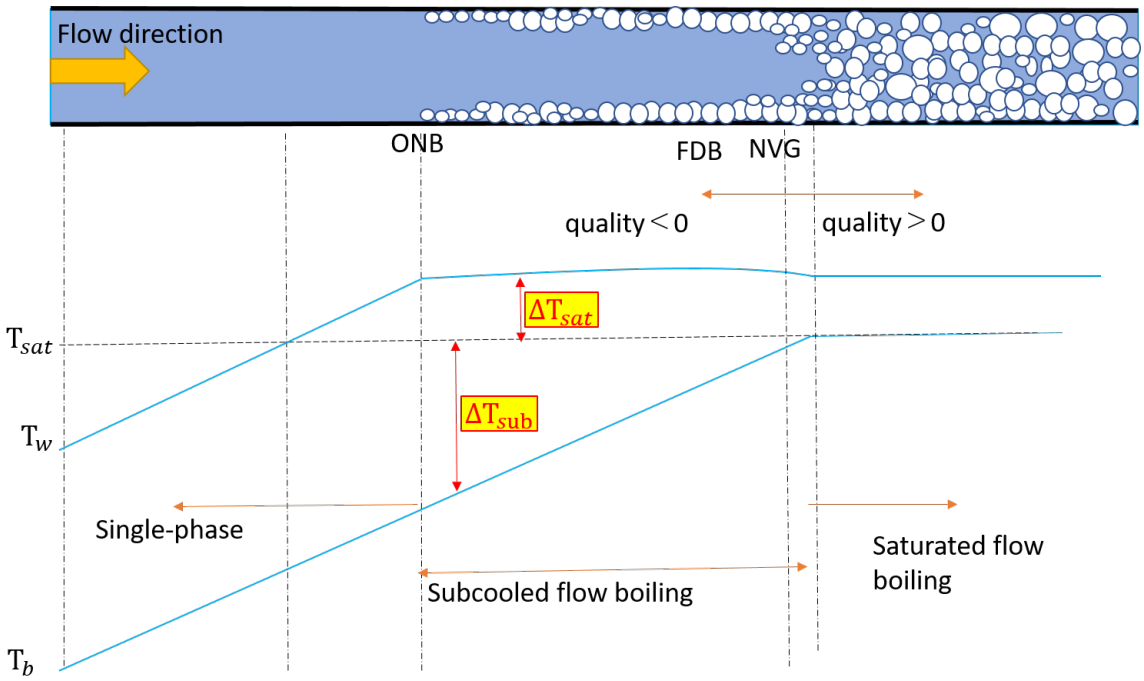

Figure 2.8: Subcooled flow boiling bubble pattern formation.

2.6 Subcooled flow boiling correlations

As mention in section 2.1, the influences that affect subcooled flow boiling have been studied by several researchers who proposed correlations to predict the heat transfer coefficient using different solid-fluid combinations. In the last 70 years and for the particular case of water as a working fluid, researchers have proposed more than 20 correlations. Fang et al. [29] proposed a classification of the correlations into five different categories (enhancement-factor models, superposition models, asymptotic models, $q - \Delta T_{sat}^{n}$ models, and flow pattern-based models). For a better understanding is necessary to define the wall superheat temperature as

$$\Delta T_{sat} = T_w - T_{sat}, \tag{2.16}$$

where T_w is the heated surface temperature and T_{sat} corrresponds to the saturation temperature. The inlet subcooled temperature need to be consider for the correlations which is

$$\Delta T_{sub} = T_{sat} - T_b, \tag{2.17}$$

where T_b denotes the bulk temperature.

2.6.1 Enhancement-factor models

These models consider the heat transfer coefficient in nucleate boiling as an enhancement ϕ of the heat transfer coefficient on the single-phase. The heat transfer coefficient in nucleated boiling is

$$h_{nb} = \phi h_{fc}, \tag{2.18}$$

where the heat transfer coefficient h_{fc} in the forced convection is in the function of the Reynolds number and the Prandtl number, equations (2.7) and (2.8) respectively. It can be reduced to

$$h_{fc} = C Re_l^m Pr_l^n \frac{\lambda_l}{d}. \tag{2.19}$$

The constant C is expressed in the equation (2.13). The constants m and n are experimentally determined according to the fluid physical properties, so substituting equation (2.19) into equation (2.18) leads to

$$Nu_{nb} = h_{nb} \frac{d}{\lambda_l} = Y Re_l^m Pr_l^n. \tag{2.20}$$

Most researchers who proposed these correlation models differ on the enhancement factor for detailed information, see table 2.1. Correlation factors are in function of the Boiling number (2.21), Jacob number (2.22), and Weber number (2.23). In addition, β, ratio of the channel height to the channel width, is considered:

$$Bo = \frac{q}{G h_{lg}} \tag{2.21}$$

$$Ja = \frac{c_{p,l} \Delta T_{sub}}{h_{lg}} \tag{2.22}$$

$$We = \frac{G^2 d}{(\rho_l - \rho_g)\sigma} \tag{2.23}$$

Table 2.1: Enhancement-factor models [29].

Autor	Enhancement factor
Shah [48]	$\phi = \begin{cases} \phi_0 & \text{for low subcooling} \\ \phi_0 + \Delta T_{sub}/\Delta T_{sat} & \text{for high subcooling} \end{cases}$ $\phi_0 = \begin{cases} 230 Bo^{0.5} & \text{for} Bo > 0.3x10^{-4} \\ 1 + 46 Bo^{0.5} & \text{for} Bo < 0.3x10^{-4} \end{cases}$
Hata and Noda [50]	$h_{nb} = 0.02 Re_l^{0.085} Pr_l^{0.4} \left(\frac{l}{d}\right)^{-0.08} \left(\frac{\mu_{l,b}}{\mu_{l,w}}\right)^{0.14} \left(\frac{\lambda_l}{d}\right)$
Hata and Masuzaki [51]	$q = 51.25 \Delta T_{sat}^3$
Baburajan et al [52]	$\phi = 267 Bo^{0.86} Ja^{-0.6} Pr_l^{0.23}$
Papell [49]	$\phi = 90 Ja^{-0.84} \left(\frac{q}{h_{lg}\rho_g u}\right)^{0.7} \left(\frac{\rho_g}{\rho_l}\right)^{0.756}$
Lee-Mudawar [53]	$\phi = 90 Bo^{0.9} Ja^{-0.98} We^{0.15} \beta^{-0.42}$

2.6.2 Superposition models

The superposition models assume that the total amount of heat transferred is the sum of the forced convection heat flux and the nucleated boiling heat flux equation (2.24). It was proposed to calculate the total heat transfer as a sum of the heat transfer coefficient of forced convection and the nucleate boiling, defined as

$$q_t = q_{fc} + q_{nb}. \tag{2.24}$$

Rohsenow model

In 1953 Rohsenow [54] developed the superposition model base on the equation (2.24), and he proposed the values for heat flux by forced convection q_{fc} as

$$q_{fc} = h_{fc}(T_w - T_b), \tag{2.25}$$

and the heat flux on the nucleate boiling as

$$q_{nb} = \mu_l h_{lg} \left[\frac{g(\rho_l - \rho_g)}{\sigma}\right]^{1/2} \left[\frac{c_{p,l}\Delta T_{sat}}{C_{sf} h_{lg} Pr_l^n}\right]^3, \tag{2.26}$$

where C_{sf} is a constant for the solid-fluid combination. Further, Rohsenow proposed a

value for the water-copper of $C_{sf} \approx 0.0128$, $n = 1$ and h_{fc} is calculated as

$$h_{fc} = 0.023 Re_l^{0.8} Pr^{0.4} \frac{\lambda_l}{d}. \tag{2.27}$$

Chen model

In 1966, Chen [56] proposed a model to predict the heat flux considering the subcooled and the saturated water flow boiling using the superposition model

$$h_t = h_{fc} + h_{nb}, \tag{2.28}$$

where

$$h_{fc} = 0.023 \left[\frac{G(1-x)d}{\mu_l} \right]^{0.8} Pr^{0.4} \frac{\lambda_l}{d} F, \tag{2.29}$$

$$h_{nb} = 0.00122 \frac{\lambda_l^{0.79} c_{p,l}^{0.45} \rho_l^{0.49}}{\sigma^{0.5} \mu_l^{0.29} h_{lg}^{0.24} \rho_g^{0.24}} \Delta T_s^{0.25} \Delta P_s^{0.25} S. \tag{2.30}$$

Chen considered the F factor based on the Martinelli parameter X_{tt} and can be calculated as

$$F = \begin{cases} 1, & \text{if} \quad \frac{1}{X_{tt}} \leq 0.1 \\ 2.35(1/X_{tt} + 0.213)^{0.736} & \text{if} \quad \frac{1}{X_{tt}} > 0.1 \end{cases} \tag{2.31}$$

The Martinelli parameter is defined by the liquid fraction of a flowing fluid and is calculated with

$$\frac{1}{X_{tt}} = \left[\frac{x}{1-x} \right]^{0.9} \left[\frac{\mu_v}{\mu_l} \right]^{0.1} \left[\frac{\rho_l}{\rho_v} \right]^{0.5}. \tag{2.32}$$

Finally, the suppression factor S is via case discrimination as

$$S = \begin{cases} \frac{1}{1+0.12 Re_{tp}^{1.14}} & \text{for} \quad Re_{tp} \leq 30, \\ \frac{1}{1+0.42 Re_{tp}^{0.78}} & \text{for} \quad 30 < Re_{tp} \leq 70, \\ 0.1 & \text{for} \quad Re_{tp} > 70, \end{cases} \tag{2.33}$$

where

$$Re_{tp} = 10^{-4}\frac{G(1-x)d}{\mu_l}F^{1.25}. \tag{2.34}$$

Butterworth model

Butterworth et al. [55] extended Chen's correlation [56] and applied it to subcooled flow boiling. This model considers two different constants, one for forced convection and another one for nucleated boiling, and it can be expressed as

$$q_t = Fh_{fc}(T_w - T_b) + Sh_{nb}(T_w - T_{sat}). \tag{2.35}$$

They propose a value for the constant F as the unit ($F = 1$) for subcooled flow boiling, and the constant S is determined by Chen's graph (refer to [56]). The heat transfer coefficient h_{fc} in forced convection is calculated with equation (2.27) and the heat transfer coefficient h_{nb} in nucleate boiling is defined by equation (2.11).

Steiner model

Steiner et al. [28] conducted experimental research with water as a working fluid for single-faced heated subcooled flow boiling. They adopted Chen's correlation and proposed S and F values for the equation (2.35) as

$$S = \frac{1}{1 + 2.53x10^{-6}(Re_l F^{1.25})^{1.17}}, \tag{2.36}$$

$$F = \begin{cases} 2.35(1/X_{tt} + 0.213)^{0.736} & x > 0.1 \\ 1 & x \leq 0.1 \end{cases} \tag{2.37}$$

where X_{tt} is the Martinelli parameter for a turbulent liquid-gas combination. Steiner also assumed $F = 1$ for the subcooled flow boiling due to the mass fraction $x \leq 0.1$ of the vapor.

The model by Yan et al.

Yan et al. [57] consider subcooled flow boiling on vertical tubes with water as working fluid, at high pressure, high mass, and high heat fluxes. They also proposed a modified Chen

correlation; in general, $F = 1$ was proposed for the case of water, h_{nb} was calculated with the equation (2.11), and S is defined by equation (2.41). They calculated the Nusselt number Nu_{cp} at constant properties defined in the equation (2.39) so that

$$h_{fc} = Nu_{cp}\left[1 + \left(\frac{d}{l}\right)^{2/3}\right]\left[\frac{Pr_l}{Pr_w}\right]^{0.01}\left[\frac{\lambda_l}{d}\right], \tag{2.38}$$

$$Nu_{cp} = \frac{(f/8)(Re_l - 1000)Pr_l}{1 + 12.7(f/8)^{1/2}(Pr_l^{2/3} - 1)}. \tag{2.39}$$

The constant f corresponds to a friction factor which is a function of the Reynolds number,

$$f = \left[0.19 \ln Re_l - 1.64^{-2}\right], \tag{2.40}$$

$$S = \left[\frac{1}{1 + 2.53x10^{-6}Re_l^{1.17}}\right]\left[\frac{T_{sat}}{\Delta T_{sub}}\right]^{0.9} \tag{2.41}$$

Gungor-Winterton

Gungor and Winterton [58] also adopted Chen's correlation and proposed new values for the subcooled flow boiling. They tested water, trichloromonofluoromethane (R11), dichlorodifluoromethane and (R12) as working fluids. The heat transfer coefficient for the forced convection h_{fc} was calculated by the equation (2.27). A new formulation, the heat transfer coefficient for the nucleate boiling h_{nb} was calculated with

$$h_{nb} = 55P_R^{0.12}\left[-0.4343 \ln P_R\right]^{0.55} M^{-0.5} q^{0.67}, \tag{2.42}$$

where the M constant corresponds to the molecular mass and the P_R corresponds to the reduced pressure. Thus the final constant for S and F are defined by t

$$S = \left[\frac{1}{1 + 1.15x10^{-6}F^2Re_l^{1.17}}\right], \tag{2.43}$$

$$F = 1 + 2.4x10^4 Bo^{1.16}. \tag{2.44}$$

Table 2.2: $q - \Delta T_{sat}^{n}$ Prediction models.

Autor	Prediction model	
Jens and Lotes [65]	$q = \left[\frac{\Delta T_{sat}}{25} \exp(\frac{P}{62})\right]^4$	where P is in bar and q in MW/m^2
Tom et al. [66]	$q = \left[\frac{\Delta T_{sat}}{22.65} \exp(\frac{P}{87})\right]^2$	where P is in bar and q in MW/m^2
McAdams et al. [64]	$q = C\Delta T_{sat}^{3.86}$	$2.26 \leq C \leq 5.8$

2.6.3 Asymptotic models

The asymptotic models assume a direct power law relation between the total amount of heat flux, the heat transfer of the forced convection, and the heat transfer of the nucleate boiling. The formula for the total heat transferred is then

$$q_t^n = \left[Fh_{fc}(T_w - T_b)\right]^n + \left[Sh_{nb}(T_w - T_{sat})\right]^n. \tag{2.45}$$

The exponent n is determined experimentally by data analysis. In fact, for $n = 1$, the asymptotic model is equivalent to the superposition model. Researchers do not often use the asymptotic method due to its complexity and the various constants that it involves. However, some literature can be found in [59–63].

2.6.4 $q - \Delta T_{sat}^{n}$ models

This family of models predicts the total amount of heat flux q based on the wall superheat temperature ΔT_{sat} as

$$q = C\Delta T_{sat}^{n}, \tag{2.46}$$

where the constants C and the exponent n are defined by the fluid thermophysical properties and the experimental conditions. It is an empirical prediction which depends only on ΔT_{sat}, which means that the $q - \Delta T_{sat}^{n}$ model is applicable for fully developed subcooled flow boiling to that $\Delta T_{sat} \geq 0$. This predictive model is not applicable for the single-phase heat transfer regime. Some models with different exponents are listed in table 2.2.

2.6.5 Flow pattern based models

Flow pattern models are based on bubble formation, flow patterns and vapor quality of the working fluid. Some researchers consider a three-zone model or vapor fraction, in addition to the boiling number. This model is developed experimentally. In general, this model has a suitable predictive power; however, the accuracy of this method dependents directly on the bubble behavior and makes it difficult to use with different refrigerants. Also, a minor variation of the flow pattern measurement may cause a higher deviation in the predicted heat transfer coefficient. Some correlations can be found in [67, 68].

2.7 Porous microchannels heat transfer enhancement methods

As mentioned in the section 1.2, the development of new machining techniques allowed the production of new micro materials that provide numerous micro holes, increase the heating area, promote more nucleation sites and thus enhance the heat transfer coefficient. In addition, these kind of materials have been reported to reduce the wall superheat temperature, increase the CHF and shift the ONB to higher wall superheat temperatures. In the last two decades, several researchers have tested the micro materials as a passive method to enhance the cooling performance. Tzeng et al. [69] performed experimental research using sintered porous copper beads, copper and aluminum bare heat sinks. The porous sink presented the best heat transfer performance compared to the bare surfaces, the heat flux enhancement was attributed to the increment in the area available for heat transfer as well as the increment on the ability to supply water through the porous body.

Gao et al. [70] developed a copper open-cell metal foam mini channel as shown in Figure 2.9. They found an increment of the boiling heat transfer coefficient of up to 1.5 times and a delay of the dry out point. They also found a reduction in the pressure drop of around 2.1-2.7 times when an open-cell was used. Deng et al. [71] developed a sintered copper porous sink with reentrant Ω-shaped microchannels. Two samples flow channels were tested (a reentrant porous microchannel and a reentrant cooper microchannel). Flow boiling using deionized water at low mass fluxes and inlet temperatures of 30, 60, and 90 °C were used to compare the heat transfer performance of the microporous channels. They found a higher number

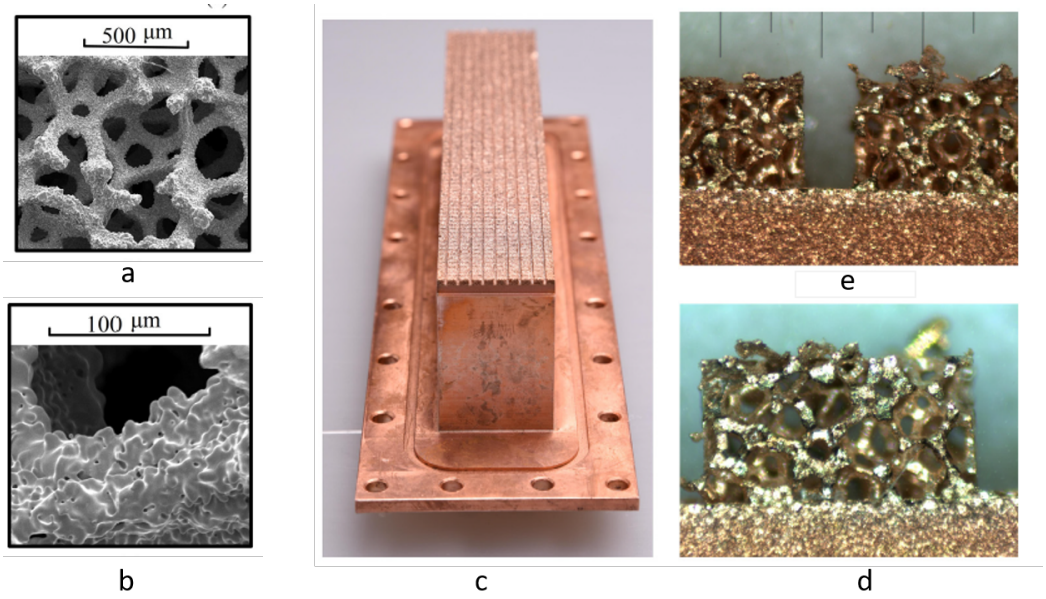

Figure 2.9: Open-cell metal foam mini channel evaporator; (a) and (b) microscopic view of the porous medium, (c) porous test section, (d) porous medium, and (e) channel between porous medium [70].

of nucleation sites using sintered porous medium an increase of the heat transfer by 2-5 times, and the instability on the flow boiling pattern was reduced. A sintered micro copper porous coating between 120-240 μm was developed by Sun et al. [76]. They used deionized water at medium mass fluxes, reporting an increment on the heat transfer coefficient and a reduction of the ONB. They also studied the boiling heat and physical parameters of the porous media. They machined a spherical and irregular powder, with three different micro diameters (50-75, 75-110, and 110-150 μm). The irregular diameter shows the highest heat flux. Xu et al. [77] also performed single directional V-shaped channels made by sintered copper. They found an enhancement of the BHT and also a delay of the CHF. A direct effect of the micropore diameter, the porous thickness, number of pores, distribution, foam material, and pore density also was found. Some publications using copper sintered fibers as heating surface using water as the working fluid are summarized in table 2.3.

2.8 Copper oxidation effects on the heat flux performance

In section 2.3, the influence of roughness, scratches, the form of the surface, etc., were explained, these factors affects the bubble formation directly and thus the heat transfer performance. However, tiny impurities, contaminants, or oxidation layers may be found at the

Table 2.3: Copper micro porous surface enhanced surfaces [72]

Autor	Enhanced surface	Characteristics
Qu et al. [73]	V-shaped open cells; Pore density 100, 130 PPI, porosrity: 0.95 foam thickness	Enhancement of the HTC and CHF
Jaikumar. [74]	Sintered fin-tops, sintered channels and sintered throughout of microchannels	Enhancement of the HTC and CHF
He et al. [75]	Bi-porous minichannel made by copper wires with a diameter of 0.03 mm each one	Enhancement of the HTC, increased pressure drop and reduction on the pressure drop fluctuation
Sun et al. [76]	Sintered microporous coating particles (diameter of 120-240 μm)	Enhancement on the HTC and reduction on the ONB

Figure 2.10: Wettability on the polished surface and the aged surface [47].

nucleation sites and affect the cooling performance.

Copper surfaces are stable in pure and deionized water. However, if oxygen is added during the boiling process or specifically to the working fluid, an oxidation layer of CuO or CuO_2 is formed on the heating surface [78]. The thickness of this oxidation layer depends on the electrochemical potential, the oxygen concentration, the heating time and the reaction time between water and copper. The oxidation process occurs in four steps defined as follows [79]:

1. Formation of small particles of oxide on the surface
2. Release of the formed particles from the surface
3. Migration through different parts of the surface (usually moved by the refrigerant flow)
4. Re-deposition and formation of a uniform oxide layer

Thus, the nucleation sites covered by the oxidation layer, Moliere et al. [80], identify a reduction in the cooling efficiency of electric turbo-generators. They found that the heat transfer is affected directly by the copper oxide particles that cause clogging in the hollows strands. They attributed the release of the oxide particles and migration to the oxygen

concentration to the water; in general, at lower oxygen concentration, the oxidation layer easily breaks loose from the surface. Vlachou et al. [47] performed experimental research using two different surfaces; one polished surface and one oxidized surface after 24 hours of heating(Figure 2.10). They report a lower bubble contact angle on the polished surface in comparison with the aged surface, and they also reported a reduction of 10% of the heat flux on the aged oxidized surface. A flow boiling experiment was conducted by Jayaramu et al. [46]. They used a copper microchannel using three different heating surfaces; a freshly machined surface, an aged surface (the first surface after oxidation), and finally, a cleaned surface (the second surface after cleaning with 0.1 M hydrochloric acid). They reported that an increase in the roughness induces more active nucleation sites and thus an increase in the boiling heat transfer. However, the aged surface presented a reduction in the heat flux and an increase of the wall superheat in comparison with the other two surfaces. This effect is attributed to the increased wettability caused by the copper oxidation. In addition, the onset nucleation boiling depends on the size of cavity holes, the shape of the cavity holes, and the surface wettability. In general, aged surfaces present lower wettability than freshly machined surfaces due to the high surface energy of the copper oxide layers. Kim et al. [81] reported a degradation of the heat transfer coefficient on a roughness copper surface in comparison with superhydrophilic aluminum surfaces; the degradation is attributed to the flooding of the scratches, holes and cavities due the oxidation. Wang et al. [82] performed flow saturated boiling experiments using four different surfaces. Figure 2.11 shows the four different surfaces with a different period time of oxidation with different mass fluxes. They reported a reduction of the nucleation sites that were covered by the oxidation layer; this layer promoted a reduction of the NSD on the oxidized copper surface. As a result, under high heat flux, the vapor blanket area on the surface is reduced. Finally, they reported an enhancement in the CHF using the oxidized surfaces; fewer bubbles were found on the surface. Nevertheless, they found a higher wall superheat temperature at the CHF. Santiago Galicia et al. [83] performed research to analyze the oxidation effect on the copper surface. The same experiment was repeated 13 times under the same experimental conditions; deionized water was used as working fluid. They found that a small oxidation layer formed on the heated surface which increased with the number of experiments, covering nucleation sites and scratches on the surface. However, the influence of oxidation on the heat flux is minimal in the single-phase region due to the absence of bubbles, and the nucleation site density

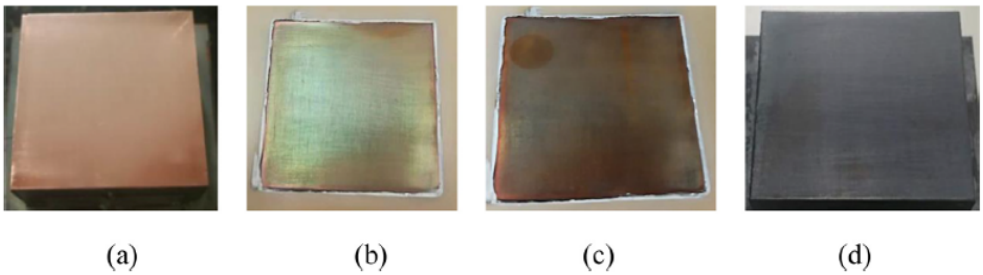

Figure 2.11: Copper bare surfaces. (a)Fresh machined surface, (b) 1 hour oxidation surface, (c) 3 hours oxidation surface, (d) 6 hours oxidation surface [82].

.

(NSD) has no notable influence on the heat flux performance. The oxidation layer has a significant impact on the two-phase heat transfer coefficient. This is attributed to the reduction in the number of nucleation sites that are covered by the copper oxidation layer. In the boiling heat flux, the wall superheat temperature increases proportionally to the number of experiments; in other words, after longer oxidation times, the wall superheat temperature increases. They also confirm a variation in the heat flux in the first five experiments, but thereafter the heat flux became stable. This is due to the fact that in the first heating hours, the oxidation layer is not uniform and some nucleation sites are covered. Their conclusion was that the oxidation layer limits the heat flux. At longer oxidation times, the effect on the wall superheat temperature is less at the same heat flux. A uniform oxidation layer is created at longer heating times.

It is also important to mention that due to the micro-holes formed by the high-porosity sintered fibers is susceptible to clogging, obstruction or fill up of the micro-holes. This fact is a demerit of the porous surfaces, in fact, the use of this materials is usually in combination with filters to trap the impurities of the working fluid [80].

Despite the high number of studies related to porous media as a passive method to enhance the heat transfer, it is necessary to perform experiments considering the large number of variables to understand and clarify the discrepancy in the heat transfer performance using microporous materials in the particular case of the heat exchangers that use a combination of copper-water.

3

Experimental method

The purpose of this chapter is the detailed information about the experimental equipment for the analysis of the subcooled flow boiling heat transfer performance using enhanced surfaces. For this purpose, an experimental apparatus was designed and assembled to visualize the flow pattern and the effects on the single-phase and two-phase heat transfer. The instrumentation, such as the heating surfaces, pressure gauges, thermocouples, pumps, PID controllers, heat exchanger, high-speed camera, etc., are explained. The experimental loop was similar to the one used in [37]. The experimental research was conducted in the Enoki laboratory of the University of Electro-Communications, Japan. The pressure conditions of the working fluid were consider to be at sea level.

3.1 Experimental test loop

A schematic of the experimental loop is shown in Figure 3.1. Most parts of the test loop components were interconnected using a PFA (Perfluroalkoxy alkane) tube with a diameter of 12.7 mm. This material was selected due to its high temperature working range (260° C), long-life use, saturated steam up to 450 KPa gage pressure, high thermal stability, and easier malleability than metal conduct pipes. The components and the PFA tubes were interconnected with Swagelok tube fittings [84], to prevent leaking and provide a hermetic connection. A hermetically closed degassing tank with a heating resistance and a maximum capacity of 40 liters was used as a reservoir. In addition, a glass condenser tube was fixed on the top part of the tank; thus, the degasification cycle was completed.

Just behind the degassing tank, a heat exchanger with a maximum capacity of 40 l/s with 20 cooling tubes was installed to reduce the temperature of the degassed water from the tank. The cooling fluid for the heat exchanger was ordinary tap water. A 2 pole magnetic drive pump "IWAKI MD-55R", propelled the flow with a maximum capacity of 70 l/min and a

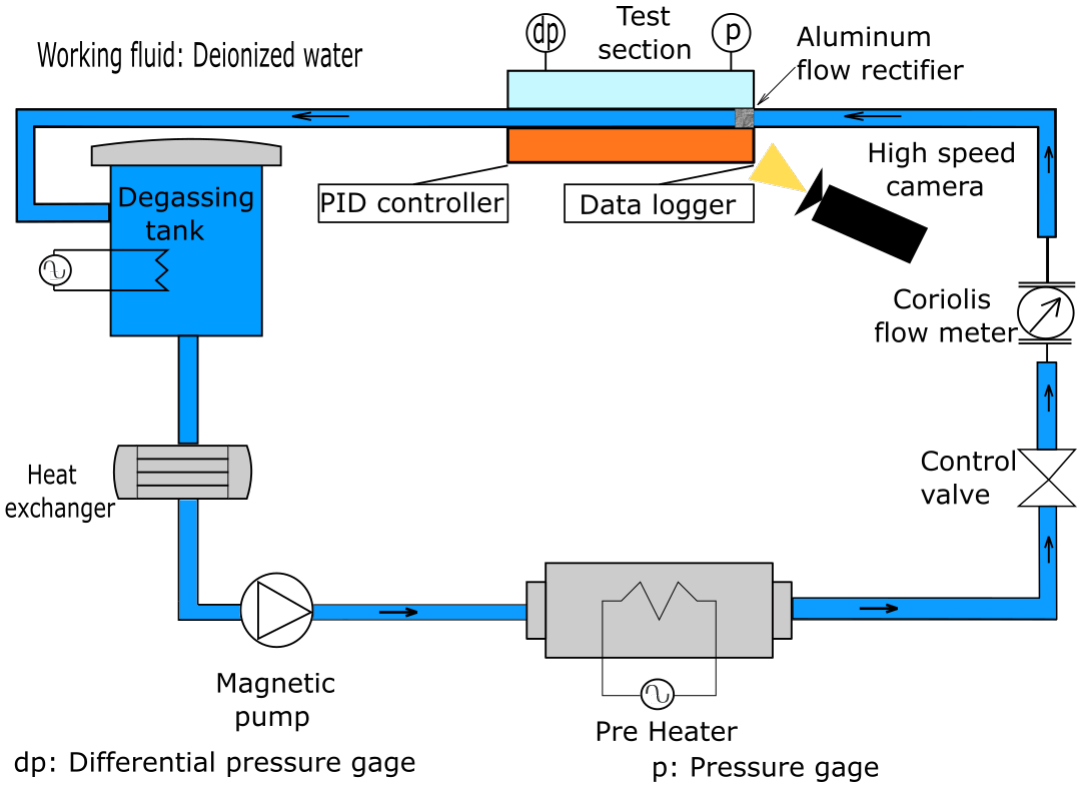

Figure 3.1: Schematic representation of the experimental loop.

maximum working fluid temperature of 80° C. The pump working range is between 2800-3300 rpm with a maximum head height distance of 5.6 meters. After the water has passed through the heat exchanger, the working fluid is heated using a stainless preheater (HWA5101) made by Yakko Electric company with a maximum capacity of 10 kW. The minimum working range to keep the fluid temperature stable is 120 liters per hour.

For better control, a digital flow meter (6710M-6 series) was installed. The preheater is equipped with an automatic temperature controlled ("YAGAMI") to avoid variations in the temperature of the working fluid. This temperature controller keeps the temperature constant in the output part of the preheater. Its power supply uses three-phase alternating current with 200 V. A control valve regulates the desired mass flux before entering the test section; the flow is measured by a Coriolis flowmeter ALTImassII (CB015) with an operating range from 0 - 96000 kg/l.

The working fluid passes through the test section (details in section 3.3). In the test section, a data logger "Yokogawa SMART DAC + ™ data acquisition system GM" is used to measure and control the parameters of the experiments. The data logger receives data from the thermocouples, differential pressure, pressure gauge, temperature on the tank, temperature in the inlet and outlet part of the preheater, inlet and outlet part parameters of the test

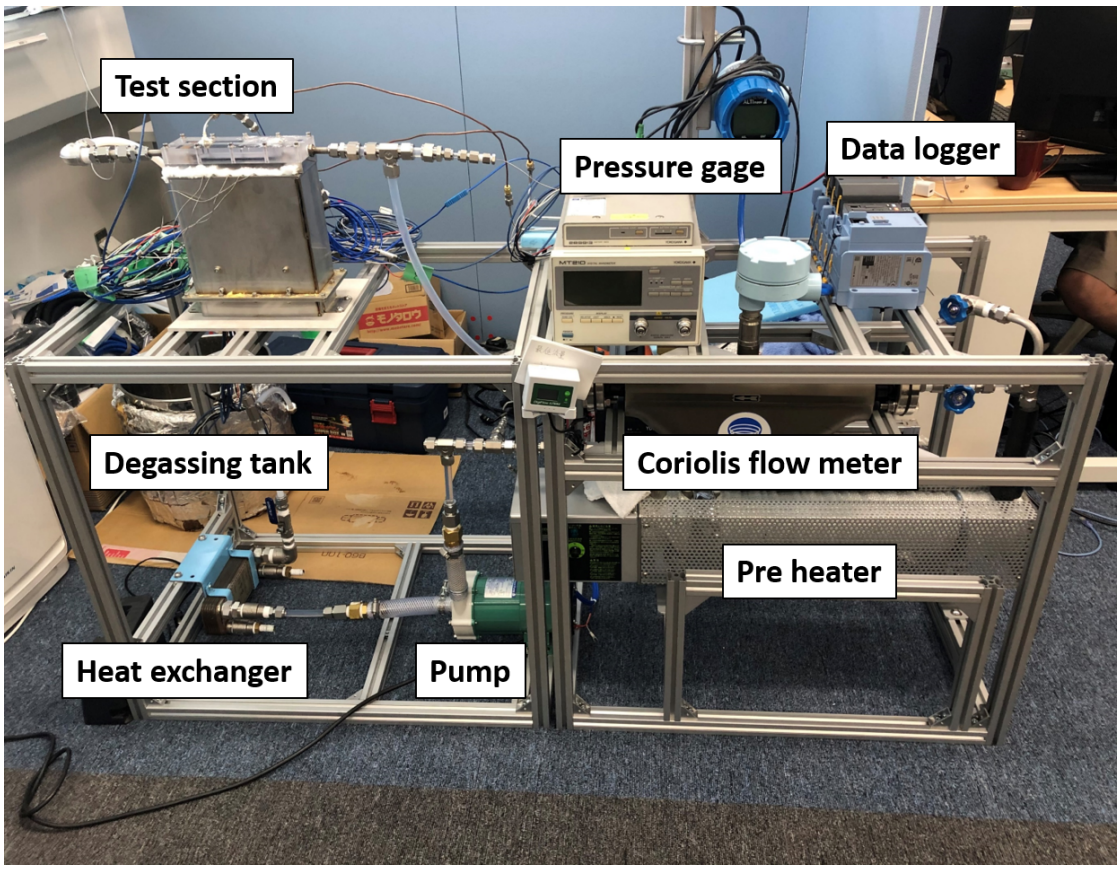

Figure 3.2: Photo of the experimental loop.

section and mass flow. A photo of the hole experimental test loop is shown in Figure 3.2. A proportional–integral–derivative (PID) controller is installed on the test section to provide the heat and control of the temperature in the heating section; to be specific, it provides the voltage to the cartridge to heat the copper block. The deionized water flows through the whole test loop back into the tank and the cycle continues until the limit conditions are reached. The test section is covered by a polycarbonate block that allows the flow visualization. The melting point of the polycarbonate is calculated around 190 -220 ° C. In front of the test section, a high-speed camera was installed (Fastcam mini AX50 type 170-M-8GB) to record the bubble pattern formation; the shutter speed was set to 1/50000 sec at 5000 frames per second (FPS). As mention in section 2.8, due to the impurities that can flow into the experimental test loop produced by the oxidation or by natural contamination, every day the degassing thank is cleaned and the deionized water is changed.

Table 3.1: Pressure meter characteristics.

Pressure meter	Pressure range	Accuracy
Yokogawa MT210	1Kpa - 3000Kpa	±0.01%
Nagano Keiki KP-15-17G	10 Kpa - 200Kpa	±0.25%

3.2 Instrumentation and measurements

The detailed information of the measurement elements in the experimental loop, such as thermocouples, mass flow meter, electric input, pressure meter, flow pattern record, and signals, are explained in this section.

3.2.1 Data acquisition

The data are recorded after 5 minutes of stable conditions and analyzed in real-time by a "YOKOGAWA Data Acquisition Module for SMARTDAC+ GM GX90XA Analog input module: DC voltage, DC current, thermocouple, RTD, contact" [85], using the Ethernet feature to ensure the real-time monitoring. Signals from the different setup modules are processed in the data logger and displayed on a personal computer. The working fluid properties are also evaluated in real-time using the software REFPROP ver. 9.1 [86]. The real-time acquisition allows recording of the physical and thermal properties of the working fluid and the test loop components.

3.2.2 Pressure measurement

The pressure meter is installed at the top part of the test section. Another pressure meter and a differential pressure meter are installed at the inlet and outlet of the channel flow. The differential pressure meter used in this research was a "YOKOGAWA digital manometer MT210". In the output section, the D/A signal for the pressure value received from the pressure calculation section at intervals of 2 ms period. The pressure meter was a dust- and water-proof stainless steel "NAGANO Keiki KP-15-17G" with a response time of 1ms or lower. More details are given in table 3.1

Table 3.2: Flow meter characteristics.

Flow meter	Temperature range	Pressure range	Accuracy
6710M-6 series	0 to 60°C	0.6Mpa	±10%
ALTImass II CB015	-40 to 130 °C	Depends on flange rating	±0.2%

3.2.3 Temperature measurements

Two kinds of thermocouples were used in the experimental loop:

- Thermocouple CHINO K-type 2 sheath thermocouple (SC SUS 316) inserted in the copper block A, placed for the measurement of the temperature fluid, except for the temperature of the tank. The sheath diameter is 1 mm, and the total length of the thermocouple is 3 meters, with a maximum temperature working range of 650°C. These elements have a measurement error of 0.05K. It was previously calibrated for minimum error.

- Thermocouple CHINO K-type 1 with a diameter of 1.0 mm was inserted in the cooper block B, and another one was also used to monitor the tank temperature. Both have a measurement error of 0.2 K

3.2.4 Mass flow measurements

Due to the preheater's minimum working range of 120 l/min, the mass flux needs to be measurement just after the water flows through the pump; for this reason, a simple digital flow meter "6710M-6 series" was used to keep the flow range for the preheater. An Oval Coriolis (ALTImass II CB015) flow meter was installed in front of the inlet part of the test section, and the mass flow is regulated with a pair of control valves. The Coriolis flow meter was used due to the high measurement accuracy and low-pressure loss. Additional information is presented in table 3.2

3.2.5 PID controller measurements

The PID controller was designed and fabricated by the Ntech company. It consists on a block heater with a group of 12 cartridges heaters "G3A133" developed by Sakaguchi Electric with a heating capacity of 5.0 KW. The 12 cartridges heaters have a diameter of 3/8 inch

Table 3.3: PID controller components.

Elements	Number of elements	Remarks
Cartridge block heaters	12	SAKAGUCHI Electric Heat G3A133 240V, 600W, 3 groups of 4 elements, Δ connection.
Thyristor	1	FUJI ELECTRIC RPDW2020T 5Kw class, set temperature control, and manual capacity control.
Temperature controller	1	OMRON E5CC-CX2ASM-000 For heating temperature setting and prevention of abnormal overheating
Heating block temperature sensor	1	MATSUO ELECTRIC H101 Fusing temperature 710 ℃ ± 10 ℃ Safety device (heater circuit cut off due to fusing)

and they are connected in three groups of four elements, each group on a Δ connection. The automatic temperature control is done by an Automatic Manual Three-phase thyristor control Automatic: OMRON E5SS Manual: 0-100%. The copper block B is equipped with a "MATSUO ELECTRIC Thermal fuse H101 blown" temperature control to prevent abnormal overheat, with a maximum capacity of $760 \pm 10°C$. Additional information is given in table 3.3.

3.3 Test section

The test section is mainly divided into two cooper blocks as shown in Figure 3.3: The copper block B consists of a group of 12 cartridge heaters inserted on the bottom part of the block. In addition, a thermocouple measures the temperature; both components are connected directly to the PID controller. The copper block A is the heating surface, consisting of two pieces of copper. In their middle, a group of ten k-type thermocouples is installed in five groups of two elements for each group. The thermocouples are connected to the data logger. A polycarbonate block is installed at the top of the copper block A; the thermophysical properties of the polycarbonate allow a high temperature working range and the flow pattern visualization.

To avoid temperature loss and for safety reasons, two stainless bases were placed to carry the copper block B. Additionally, a stainless case was also placed to cover the copper block A and B, giving enough space to record the water flow pattern. The whole section was covered by an insulator and a stainless case.

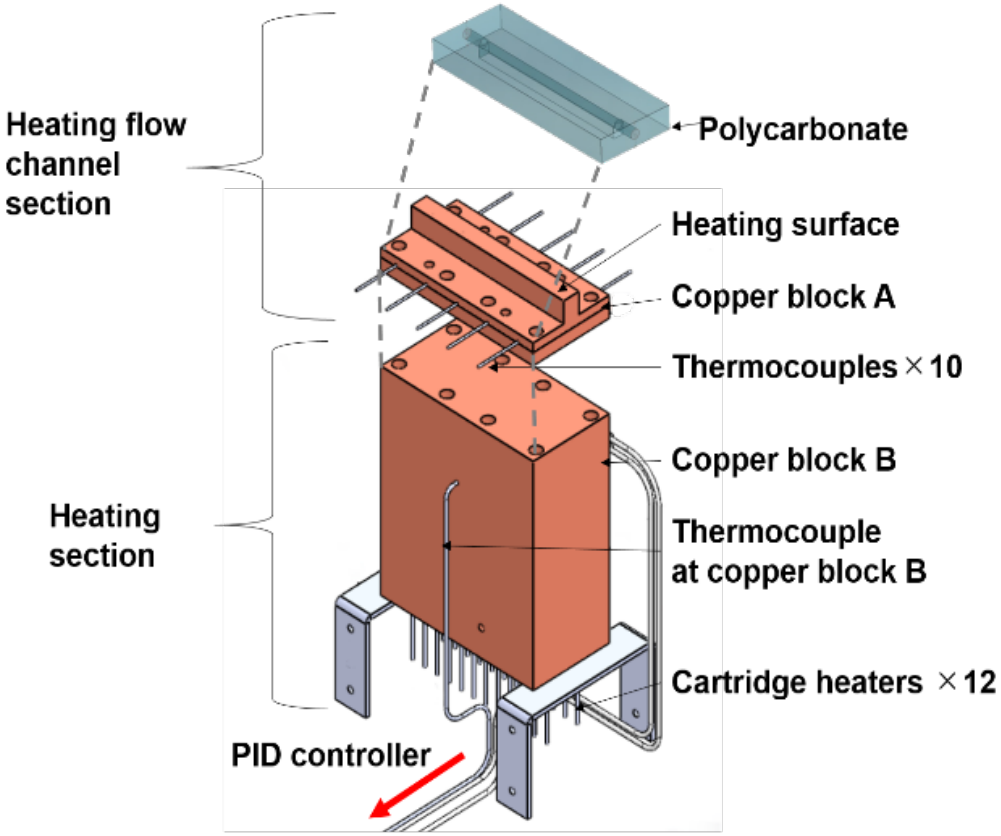

Figure 3.3: Schematic of the test section

3.4 Flow channel and thermocouple distribution

The flow channel between the heating surface and the polycarbonate is 10mm x10 mm square as shown in the figure 3.4a (front view) and 3.4b(lateral view), the flow direction is from right to left. The polycarbonate has two holes for the pressure and the differential pressure meter, respectively. In order to correct the mass velocity profile and boundary layer, a porous aluminum 10x10x10 mm was installed. The dimensions of copper block A are 100 mm length x 17 mm height and 50 mm width. In addition, two k-type thermocouples are installed, one just before and one behind the heating surface. The heating surface is a rectangular area of 100 x10 mm; inside the heating surface, five groups of 2 thermocouples are installed. The distance between each group of thermocouples is 20 mm, starting from 10 mm from the inlet part of the flow direction as shown in figure 3.4c, and the distance between the two thermocouples is 9 mm (Figure 3.4b).

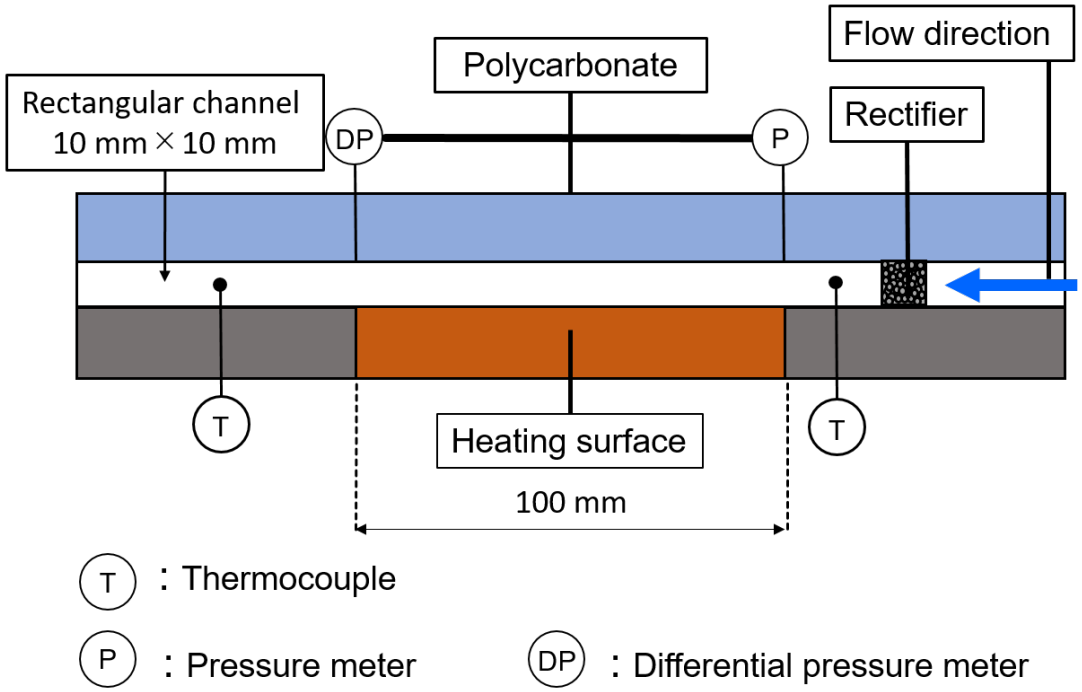

(a) Front view of the flow channel

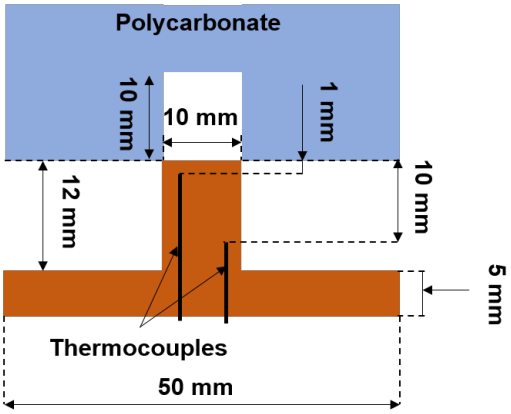

(b) Distance between each part of thermocouples

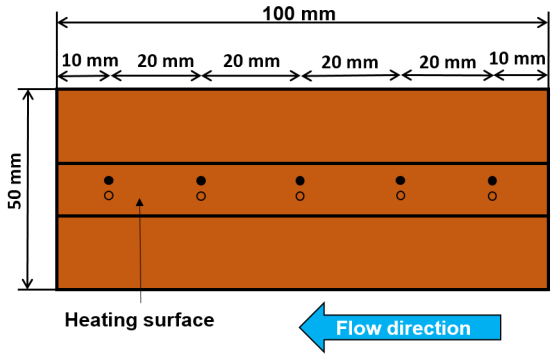

(c) Thermocouples distribution on the heating surface

Figure 3.4: Heating surface, thermocouples distribution and flow channel characteristics.

3.5 Heating surfaces

The purpose of this research is to compare the heat transfer performance using porous materials in comparison with the bare surface. Five different copper surfaces were fabricated. One with a bare surface and one porous surfaces (four different porous thickness surfaces). The porous surface has a high-porosity sintered copper fibers attached to the heating surface. All the surfaces were fabricated by Mitsubishi Materials Co., LTD [87], and the details are explained as follows.

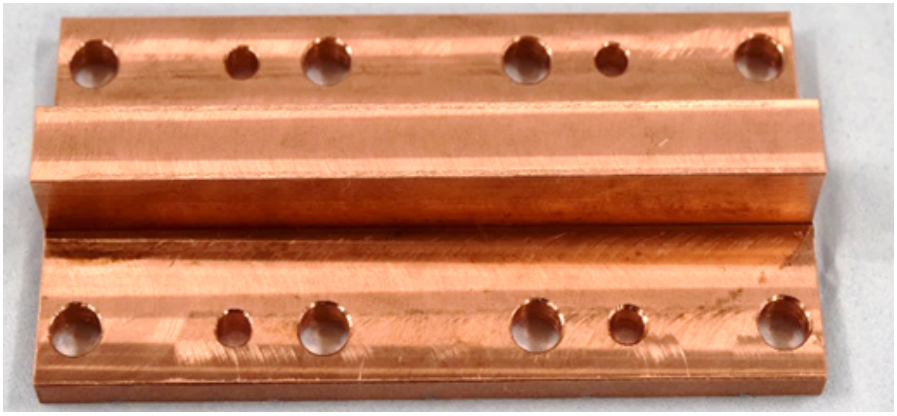

Figure 3.5: Bare surface.

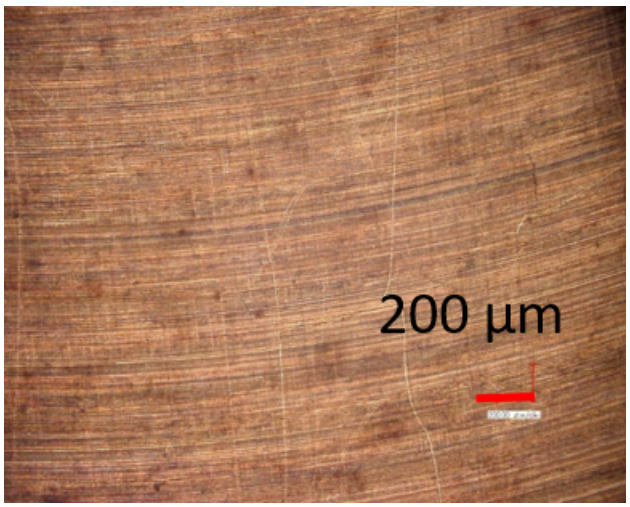

Figure 3.6: Bare surface microscopic view (100x amplification).

3.5.1 Bare surface

Figure 3.5 shows a photograph of the bare surface (0mm thickness of the porous layer). This surface has no porous material attached to the surface. The heating surface and flow channel can be observed on Figure 3.4a; the holes on the copper are designed to insert the compression screws after placing the thermocouples inside the copper block. The bare surface roughness was measured using a Dektak stylus profiler. The roughness was $Ra = 0.4\mu$m. A microscopic view of the bare surface is shown in Figure 3.6. The thermal conductivity is constant over the whole solid surface due to absence of attached materials.

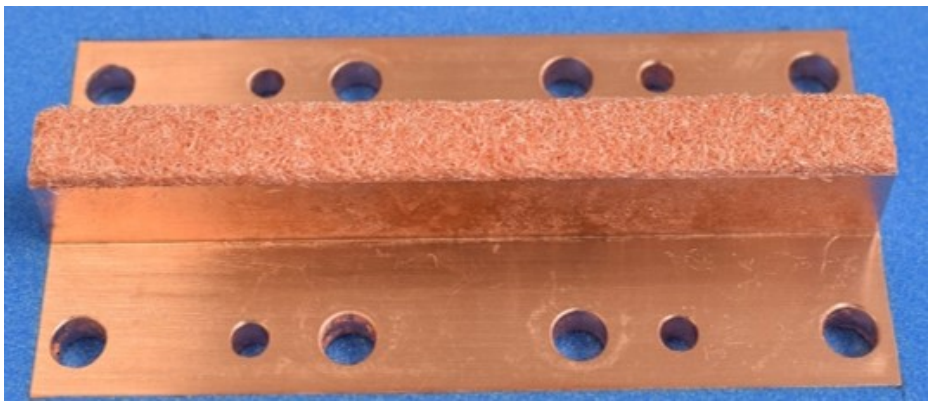

Figure 3.7: Porous surface.

3.5.2 Porous surface

The porous surface consists of a high-porosity sintered fibers attached to the surface as shown in Figure 3.7. The porosity of the sintered fibers body was calculated in 86%, this porosity is one of the highest porosities that can be reached on the sintered process. The diameter of each fiber is around 40μm as shown in Figure 3.8. In other words, the porous surface is a bare surface with the sintered fibers attached. The contact resistance between the porous material and the surface can be neglected because the identical materials are sintered together; as mentioned in the above sections (2.1, 2.3, and 2.7) the intertwined fibers increased the wetting area and promoted the occurrence of nucleation sites. The porosity and the material are the same for all thickness of the porous layer. The roughness of the porous material was calculated as $Ra = 24.1\mu$m.

The copper fibers are distributed randomly due to the sintered process, the form and direction of each fiber is difficult to predict or calculate as shown in the microscopic view of the Figure 3.9. Here four different microscopic amplification views (100, 200, 500, and 1000 x) are shown under a scale of 200 μm represented by the red arrow on each microscopic view. Because the fact that the copper fibers are sintered, the distribution and the density of fibers is unknown, thus the calculation of the porosity need to be calculated after the fabrication process. In addition, the micro-holes formed by the sintered fibers have not a constant value and also the number of channels inside the porous body in unpredictable.

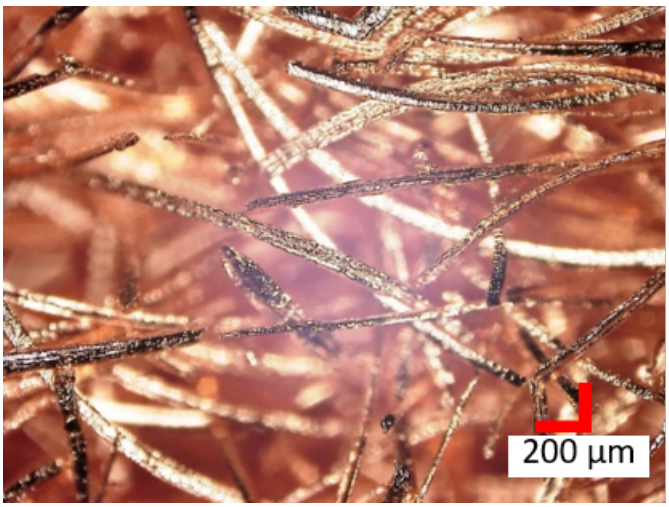

Figure 3.8: Porous surface microscopic view (100x amplification).

Table 3.4: thickness of the porous layer parameters.

Surface	Thickness of the porous layer Pt [mm]	Porosity [%]	Roughness [μm]
Bare surface	0	-	0.4
Porous surface	0.2, 0.5, 1, 2	86	24.1

Porous thickness

In order to compare the influence of high-porosity sintered fibers, four different thickness of the porous layer were fabricated and sintered on the surface, in addition to the bare surface (0 mm) shown in Figure 3.10a, the porous thickness is shown in the Figure 3.10b. A resume of the machined heating surface is given in Table 3.4.

3.6 Experimental procedure and conditions

3.6.1 Experimental parameters

To analyze the effects of the mass flux, the thickness of the porous layer and the inlet subcooling temperature in the heat transfer coefficient were considered as parameters. The mass flux was considered from relatively low to high Reynolds numbers, from laminar over transitional to turbulent flow. The subcooling inlet temperature also was considered with respect to low, medium, and high subcooling degrees. These parameters were tested for each heating surface. In other words, three mass flux parameters, three inlet subcooling temperature parameters in combination with five different heating surfaces make a total of 45 different experimental

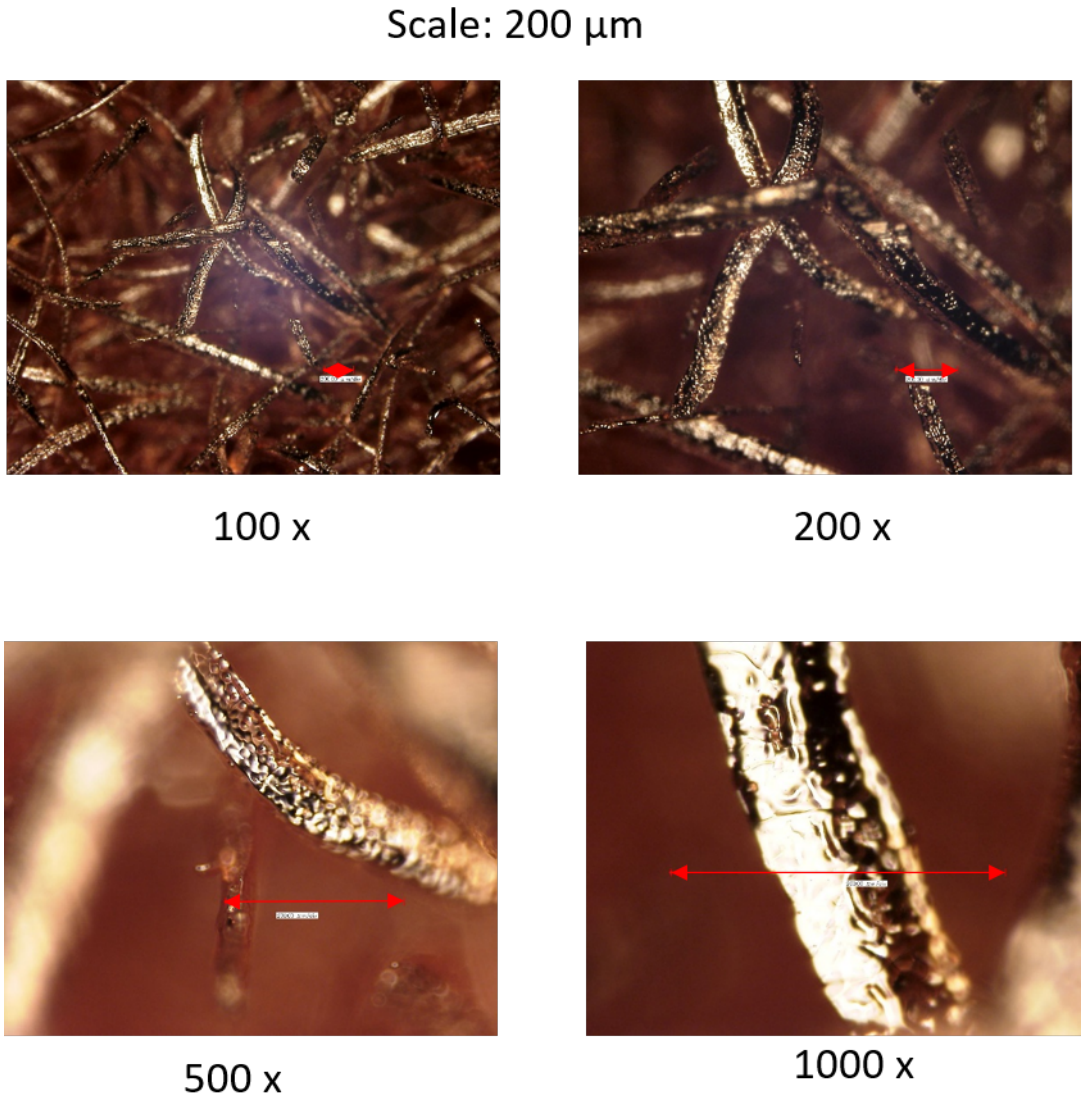

Figure 3.9: Microscopic view of the copper fibers.

conditions. Details of the experimental conditions are given in Table 3.5. All the experiments were carried out under atmospheric pressure corresponding to sea level.

3.6.2 Experimental procedure

The experimental procedure is the following:

1. Turn on the electric heater installed on the tank and supply the glass condenser with tap water. Conduct a degasification of the deionized water for around 2 hours to unsure the absence of microbubbles that could affect the heat transfer coefficient.

2. Supply the heat exchanger with tap water and regulate the flow according to the inlet

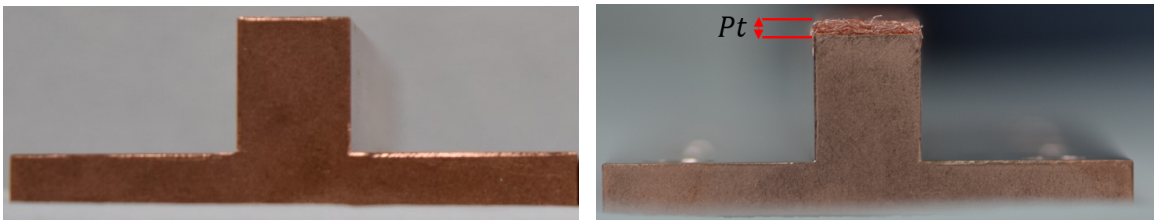

(a) Bare surface (porous thickness 0 mm) (b) Thickness of the porous layer (Pt)

Figure 3.10: Porous and bare thickness.

Table 3.5: Experimental parameters.

Mass flux	G [kg·m^{-2}·s^{-1}]	200, 400, 600
Inlet subcooling temperature	$\Delta T_{sub}[K]$	30, 50, 70
Thickness of the porous layer	Pt	0, 0.2, 0.5, 1.0, 2.0
Porosity	ϵ [-]	0.86
Hydraulic diameter	d [mm]	10

mass flux.

3. Confirm that the valves are opened, ensure that the polycarbonate is correctly placed in the test section, and activate the magnetic pump to dispatch the fluid.

4. Regulate and confirm the water flow with the valves and the mass flow meters respectively. Calibrate the valves to the desired mass flux.

5. Activate the preheater and set the temperature to the desired subcooling degree. Wait around 5 minutes to reach a steady temperature

6. Remove the entrapped air from the pipes and the differential pressure meter by opening the purge valves, also confirm the real-time data.

7. Turn on the PID controller, set the copper block at an arbitrary temperature of 60 ° C and wait until the steady state conditions are reached.

8. After reaching the steady state conditions, record the data for a period of around 3 minutes. In addition, record the flow pattern with the help of the high-speed camera.

9. Rise the temperature by 40 ° C and repeat step number 8 until the Critical Heat flux (CHF) is reached or the cooper block temperature reaches the safety conditions (580 ° C). The CHF is an unsteady physical phenomenon and is difficult to predict. For

this reason, after the copper block reaches the 450 ° C, record the data continuously (without considering the stable conditions).

Due to the abrupt increment on the wall superheat after the CHF, the data is unstable and need to be recorded every second, this phenomena was also observed by Nukiyama [23] who reported an unstable conditions on the heating surface mainly produced by the working temperature that is near to the melting point of the solid and also due to the hysteresis. The conditions are extremely difficult and he identified the jump into the boiling curve. Some year later, this point (after the CHF) was called *burnout point* or *boiling crisis*. The results of the present thesis shows the experimental heat flux under stable conditions before the Critical Heat Flux (the data was recorded for three minutes), after this point the plotted data is unstable conditions as explained in the step 9 of the experimental procedure. One single experiment takes between 3.5 and 4.5 hours, and around 2 hours of cooling, this allows to perform a total of 3 experiments per day. Every day the deionized water was changed to avoid impurities inside the flow channel.

3.7 Data reduction

The calculation of the heat flux in each part of the thermocouple distribution as defined in section 3.4 is calculated using Fourier's law

$$q = k\frac{\Delta T}{\Delta x}, \tag{3.1}$$

where the ΔT is the measured temperature difference and Δx is the distance difference between each pair of thermocouples. The thermal conductivity of the copper is also a function of the temperature difference, namely

$$k = -0.0713\left[\frac{T_2 - T_1}{2}\right] + 402.68. \tag{3.2}$$

As shown in Figure 3.11, a distance of 20 mm separates the five groups of thermocouples. Each group of two thermocouples covers a heating area of 200 mm^2; thus the total amount of heat flux can be expressed with equation 3.4, and each part of the five groups is calculated as

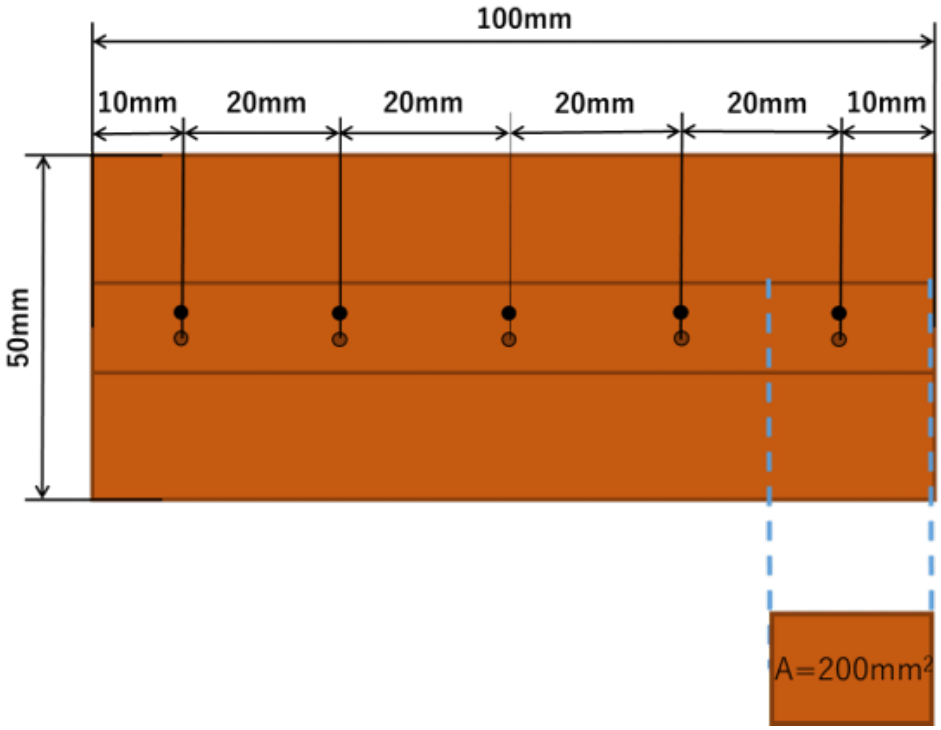

Figure 3.11: Area distribution of each group of thermocouples.

$$Q_1 = A\frac{k_1 \Delta T_1}{\Delta x_1}. \tag{3.3}$$

The total heat flux is the sum of the partial heat fluxes

$$q = \sum_{i=1}^{5} \frac{q_i}{5} = \frac{q_1 + q_2 + q_3 + q_4 + q_5}{5}. \tag{3.4}$$

In addition to the calculation using the Fourier's law, the heat flux was also compared to the inlet and outlet temperature via

$$qA = \dot{m} C_p \Delta T, \tag{3.5}$$

where ΔT is the inlet and outlet temperature difference, $\dot{m}$ is the mass rate and C_p is the specific heat. Performing the proper substitutions, the equation 3.5 can be rewritten as

$$qA = G\left(\frac{\pi d_h^2}{4}\right)(h_{out} - h_{in}). \tag{3.6}$$

Due to the thickness of the porous layer increase inside the flow channel as shown in Figure 3.12 different hydraulic diameter need to be consider for the calculation of mass flow

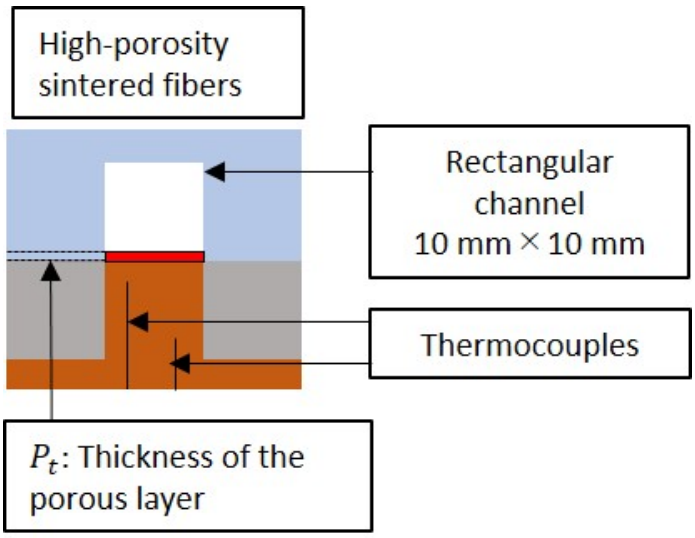

Figure 3.12: Flow channel of the test section.

Table 3.6: Uncertainly values to consider on the calculation of the heat flux.

Parameter	Uncertainty
Pressure meter	0.26 kPa
Mass flux	0.2%
Copper block depth distance	0.02 mm
Thermocouples at copper block A	0.05K
Thermocouples at copper block B	0.2K

as shown in the equation (3.6), however, the high porosity of the sintered copper fibers (86%) allows to minimize the effects of different hydraulic diameters and this can be neglected, considering the 10 mm x 10 mm flow channel as constant for all the surfaces.

3.7.1 Uncertainly analysis

The measurement uncertainty was calculated following the method by Taylor et al [88]. The uncertainty of the heat flux and the errors for each measuring instrument is shown in equation 4.10 and Table 3.6 respectively. We have

$$\Delta q = \sqrt{\left(\frac{\delta q}{\delta k}\Delta k\right)^2 + \left(\frac{\delta q}{\delta x}\Delta x\right)^2 + \left(\frac{\delta q}{\delta T_1}\Delta T_1\right)^2 + \left(\frac{\delta q}{\delta T_2}\Delta T_2\right)^2}, \tag{3.7}$$

where Δq is the uncertainty of the heat flux, Δk is the uncertainty of the copper thermal conductivity, Δx is the uncertainty of the distance between each pair of thermocouples, ΔT_1 and ΔT_2 are the uncertainties of the thermocouples.

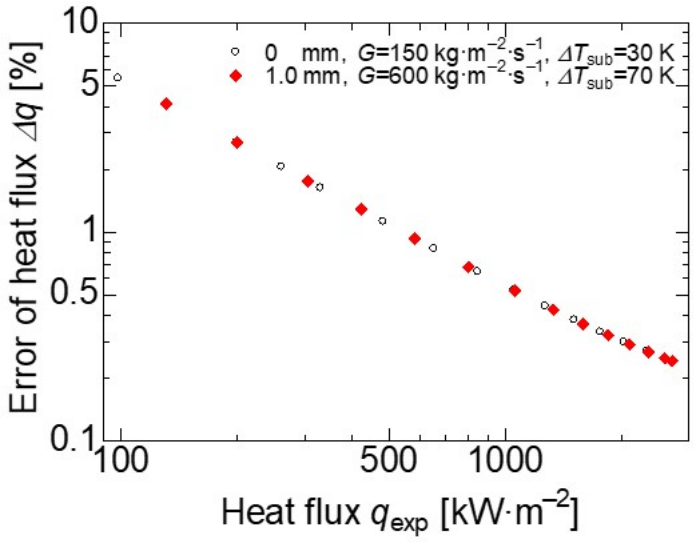

Figure 3.13: Error of the heat flux

A graph to compare the error of the heat flux results for the porous surface and the bare surface is plotted in Figure 3.13. The 1 mm thickness of the porous surface was taken as a reference for the porous heating surface and is compared with the bare surface. The graph shows a good relation between both surfaces, here the heat flux error is around 3% at low heat flux (around 200 kW·m^{-2}), nevertheless, at higher heat flux, the error tends to be reduced by around 0.5% at heat fluxes higher than 1000 kW·m^{-2}.

In order to verify the repeat ability of the experiments the same experiment was repeated twice. To compare the bare surface and the porous surface, the 1 mm thickness of the porous layer and the bare surface (0mm) were tested. It is also important to consider the importance of the subcooling temperature as mention by Fang et al. [29]. Figure 3.14 shows the boiling curve of both surfaces (0mm and 1 mm thickness of the porous layer), in addition to the Steiner correlation that predicts the subcooled flow boiling heat flux in one side heated surfaces for the nucleated boiling [28]. The prediction model that predicts the heat flux in relation with the wall superheat using the bare surface is explained in subsection 2.6.2. It was found a better relation of the predicted heat flux and the experimental heat flux at high subcooling temperature. Figure 3.14a shows the boiling curve at low subcooling temperature ($\Delta T_{sub} = 30$), here the heat flux using the bare surface and the predicted heat flux showed a percentage error of 4% at low heat flux. Nevertheless, at high heat flux the percentage error increased to 36% at the maximum heat flux. This high percentage error is attributed to the heat flux near to the CHF, inf fact, the subcooled correlations tends to shows a

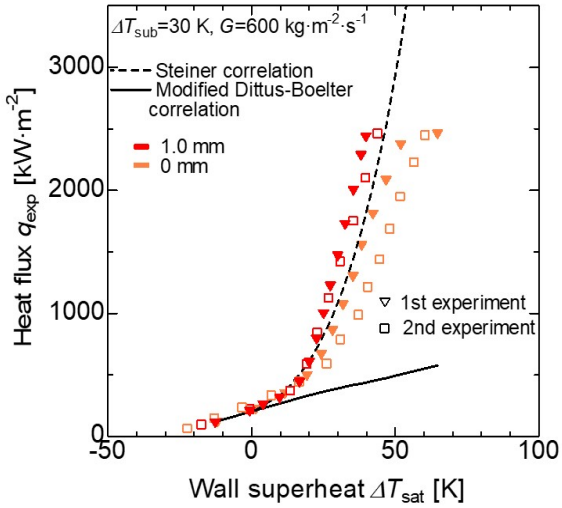

(a) $\Delta T_{sub} = 30$ K, repeat ability for the 1 mm thickness of the porous layer and the bare surface.

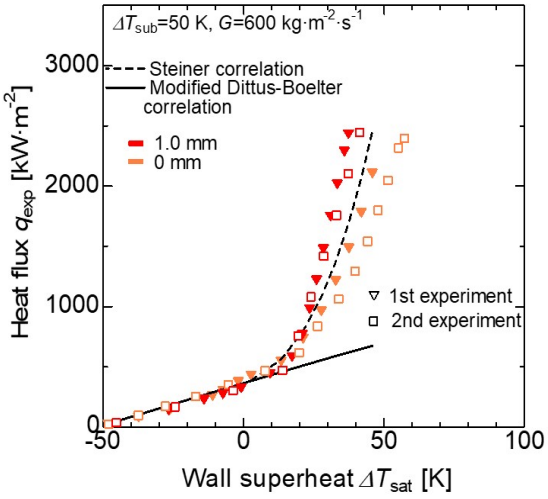

(b) $\Delta T_{sub} = 50$ K, repeat ability for the 1 mm thickness of the porous layer and the bare surface.

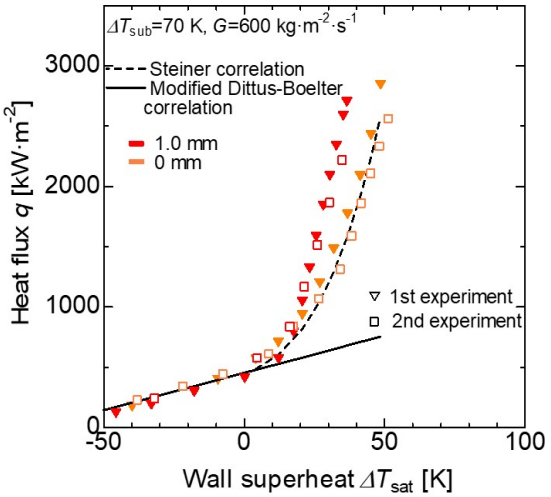

(c) $\Delta T_{sub} = 70$ K, repeat ability for the 1 mm thickness of the porous layer and the bare surface.

Figure 3.14: Confirmation of the repeat ability in the heat flux experiments using the high-porosity sintered fiber and the bare surface.

higher error in high heat fluxes. Figure 3.14b shows a minimum percentage error of 8% at low heat fluxes, in the other hand, a maximum percentage error of 38% was found. These errors correspond to the medium subcooling temperature $\Delta T_{sub} = 50$. As expected, at high subcooling temperature the error tends to reduce due to fact that the inlet temperature of the working fluid is not close to the boiling temperature. Figure 3.14c shows a minimum percentage error of 0.2% and a maximum of 9.5%.

Due to the absence of the subcooled flow boiling correlations that can predict the heat flux using high-porosity sintered fiber, the error percentage was calculated with the bare surface. Nevertheless, the plot of the 1 mm thickness of the porous layer shows a high repeat ability,

having a percetage error bweteen the first and the second experiment of around 6%.

4

Experimental results

This chapter presents the results in the case of the single-phase and two-phase heat flux as well as the heat transfer coefficients of the bare and porous surfaces. The single-phase regime was considered when the wall superheat temperature was lower than 0 K($\Delta T_{sat} < 0$K), in this regime, the analysis of the bubble flow could be neglected. In addition, the effects of the oxidation were analyzed at high mass flux and low inlet temperatures were discussed.

4.1 Effects of the oxidation layer on the heat flux

In order to verify the influence of the copper oxidation layer on the heat flux and on the wall superheat, a total of 13 experiments (around 52 heating hours using the same experimental loop) was performed under the same experimental conditions using the same polished bare surface as shown in Table 4.1. After the series of 13 experiments, a black copper oxide layer had clearly formed on the heating surface. Figure 4.1a shows the polished bare surface before starting the experiments, and Figure 4.1b shows the copper oxide layer after the 13 experiments. The surface was polished with Tamiya polishing compound, in the grades "coarse", "fine" and finally "finish". The color of the copper block changed color considerably, as did the surface rugosity. For the safety of the experimental loop and the heating surface, the experiments were stopped at a maximum heat flux of around 2200 kW·m^{-2} The analysis of the oxidation effects will be divided into the single-phase and the two phases regime to

Table 4.1: Parameters for the experiments to verify the effects of the oxidation layer on the heat flux.

Mass flux	G [kg·m^{-2}· s^{-1}]	600
Inlet subbcoled temperature	ΔT_{sub} [K]	70
Bare surface rugosity	Ra [μm]	0.4
Maximum heat flux	kW·m^{-2}	2200

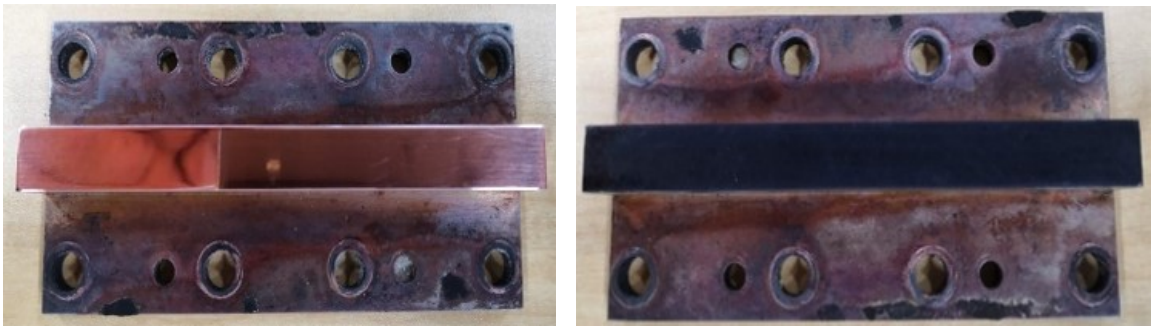

(a) Polished bare surface (before oxidation) (b) Oxidized bare surface (after 13 experiments)

Figure 4.1: Bare heating surface before and after oxidation.

consider the effect of the NSD and the bubble flow pattern. It is important to mention that the first experiment was performed with the polished heating surface without any washing process to remove the polishing compound, thus less active nucleation sites and a reduction on the heat flux is expected.

4.1.1 Oxidation effects in the single-phase regime

The results of the 13 oxidation experiments on the single-phase regime are shown in Figure 4.2. One can note a slight and almost marginal variation from experiment to experiment in the heat flux and the wall superheat temperature. However, the heat flux in the first experiment was lower than in the following repetitions. This can be attributed to the polish compound residues that remained on the cavity sites and provide an additional thermal resistance between the heating surface and the working fluid (See figure 4.3).

In addition, the reason why the heat flux did not show a high variation on the heat transfer coefficient is, that the thermal boundary layer is small enough that its influence can be neglected on the heat transfer coefficients. The absence of bubble formation also allows to keep up about the same value of the heat flux during all the experiments except for the first one. Due to the absence of bubble formation, the flow pattern did not change visibly, and it can be concluded that there is no considerable effect of the oxidation layer on the single-phase due to the absence of bubble formation.

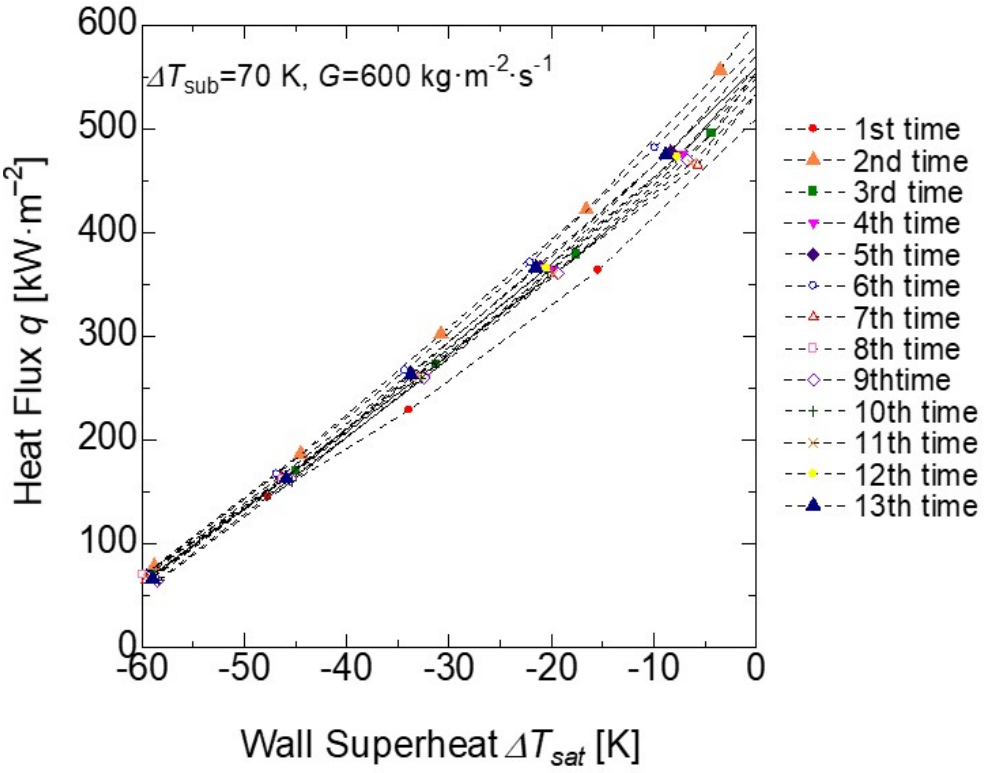

Figure 4.2: Heat flux on the single-phase for the thirteen experiments.

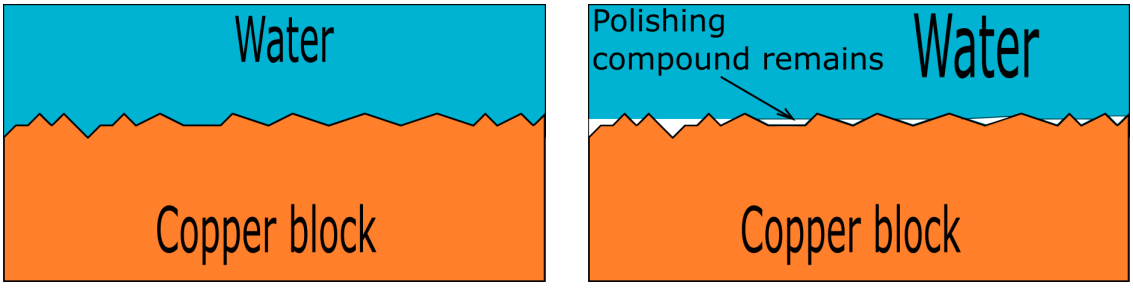

(a) Freshly machined surface

(b) Polishing compound remains on the surface

Figure 4.3: Nucleation sites covered by the polishing compound.

4.1.2 Oxidation effects in the two-phase regime

Regarding the oxidation layer effect on the boiling regime, Figure 4.4 shows the relation for heat flux and wall superheat. The first and the second experiment were stopped at a copper block B temperature of 540 °C, the rest of the experiments were stopped at a copper block B temperature of 580 °C. This experimental procedure was changed due to the thermal resistance formed by the oxidation layer between the copper block B and the copper block A. A considerable increment on the wall superheat temperature was found as well as a reduction of the heat flux after the thirteen experiments. From the first experiment to experiment number thirteen, the heat flux showed a reduction of around 8% (From 2259 kW· m^{-2} to 2081 kW·

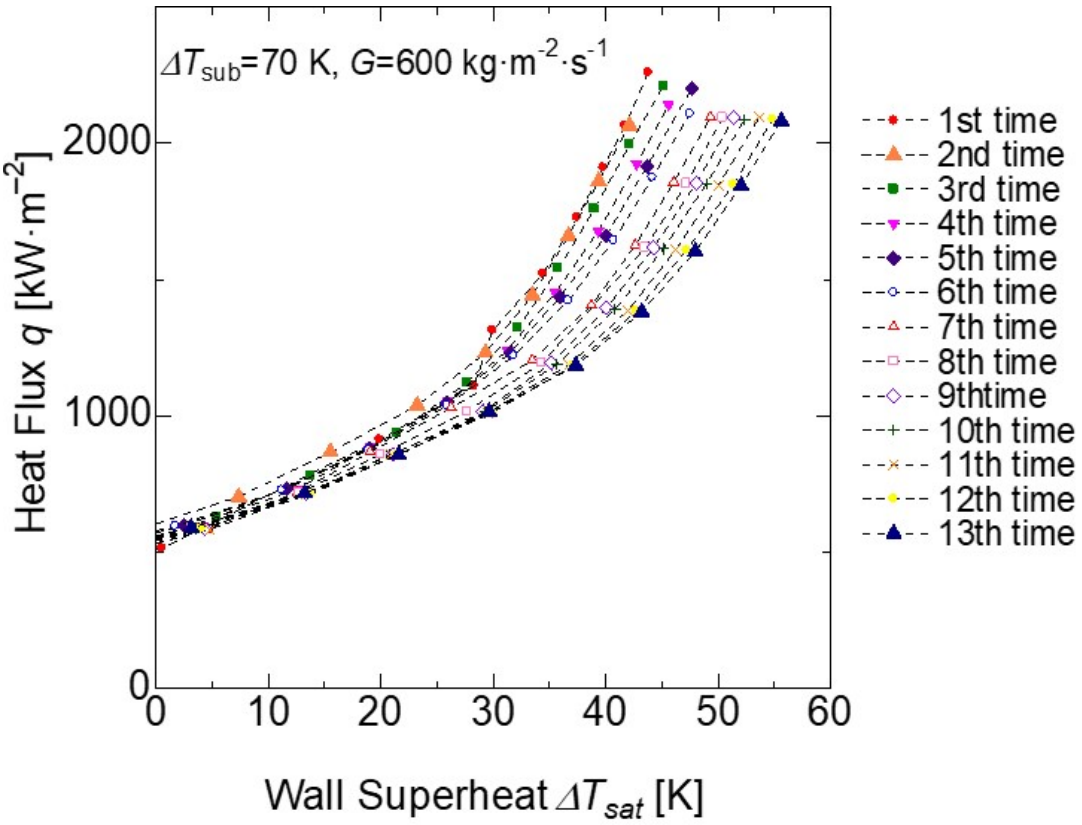

Figure 4.4: Heat flux for the flow boiling for the thirteen experiments.

m^{-2}) and there was an increase of about 26% of the wall superheat temperature (11.74 K). This increase can be attributed to the copper oxidation layer that covers the nucleation sites and reduces the contact with the water; thus, the thermal resistance also increased.

An abrupt increase of the heat flux at a wall superheat temperature of around 28 K ΔT_{sat} in the first experiment also was observed. This increase is due to the fact that the polishing compound was removed by the boiling water, and the nucleation sites freed from the remains of the compound as shown in Figure 4.3b.

In general, from the first to the sixth experiment, the heat flux presented a small variation of the maximum heat flux; from the seventh to the last experiment, nevertheless, the wall superheat increased in all the cases. The variation in the heat flux is due to the formation of copper oxide particles on the heating surface; at this point, the oxidation layer is not uniform, and the formation and deposition of copper oxidation is random, also affected by the water flow, as shown in the Figure 4.5a. After longer heating times, to be specific, after the seventh experiment, a uniform copper oxidation layer is formed, and the heat flux variation is reduced for the subsequent experiments as shown in Figure 4.5b.

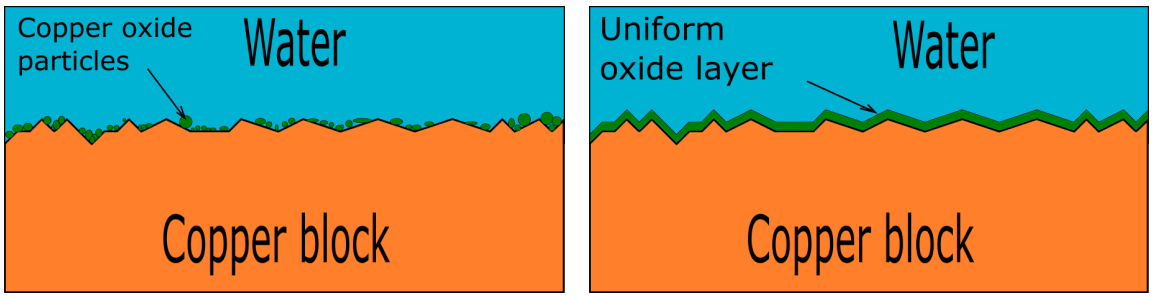

(a) Copper oxide particles deposition (b) Uniform oxide layer

Figure 4.5: Copper oxide layer formation.

After the analysis of the oxidation temperature, it was found that the oxidation layer has a minimal effect on the heat flux for single-phase flow; however, in the boiling regime, the heat flux was reduced by the influence of the oxidation layer. During the first hours of heating, small copper oxide particles start covering some nucleation sites in a random pattern, then gradually, a uniform oxidation layer is formed, and the variation on the heat flux is lower. On the other hand, the oxidation layer produced on the copper surface covers a high number of nucleation sites, thus the contact of the water with the heating surface is reduced; as a result, an increment on the wall superheat was found after the onset of nucleate boiling. Finally, the oxidation layer limits the heat flux. At higher oxidation times, the increment on the wall superheat temperature reduces gradually.

The influence of the oxidation layer and the inlet subcooling temperature also were considered; similar experimental conditions were performed as by Wang et al. [82], who consider saturation temperature conditions for the degassed water and mass flux of 640 kg$\cdot$ m^{-2} $\cdot$s^{-1}, also for the combination copper-water for the heating surface and refrigerant. Our result and a comparison with Wang et al. [82] are shown in Figure 4.6. The oxidation layer delays the ONB and also shifts the boiling curve to higher wall superheat temperatures regardless of the water subcooling temperature of the inlet. At low wall superheat, the effect of the oxidation layer is minimal. It is also well known that a high subcooling inlet temperature leads to a higher CHF and higher ONB. Finally, the copper oxidation layer allows reaching a higher CHF under the same experimental conditions. After the analysis of the results, it was decided to perform the experiments following the same order for all the thickness of the porous layer surfaces as well as the bare surface as shown in Table 4.2.

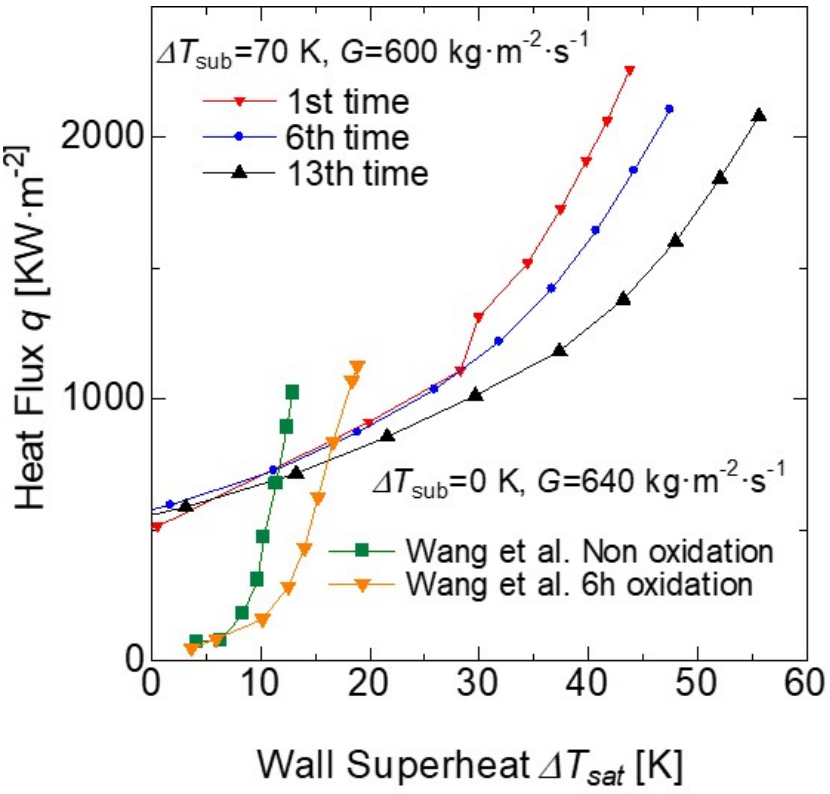

Figure 4.6: Influence of the subcooling degree and oxidation layer on the heat flux.

4.2 Modified Butterworth superposition model

The subcooled flow correlations mentioned in section 2.6 have being developed by several researchers. The one by Butterworth et al. [55] is the most commonly used and modified. However, this correlation considers a flow boiling in circular tubes and pipes with medium diameter. The calculation by Butterworth considers the diameter of the tubes under a constant heat flux; this provides a larger heating area than the square one as shown in Figure 4.7. When square-shape channels are used in the channel flow, it is necessary to consider the hydraulic diameter in the calculation of the heat flux. A reduction in the heating area directly affects the amount of heat transferred from the heated surface to the liquid coolant. Steiner

Table 4.2: Experiment order for each thickness of the porous layer.

		Mass flux [kg· m^{-2} ·s^{-1}]		
Thickness of the porous layer [mm]	Subcooling temperature [K]	200	400	600
0, 0.2, 0.5, 1, and 2	30	9th	8th	7th
	50	6th	5th	4th
	70	3rd	2nd	1st

et al. [28], employed the superposition model from equation (2.35). They also calculated a constant value for the constants F and S as shown in equation (2.36) and (2.37) respectively for a square and a one side heated flow channel.

Hua et al. [59] and Vlachou et al. [47] performed experiments using a one side heated surface and rectangular flow channel. They proposed a different Dittus Boelter correlation (equation 2.6) to calculate the forced convection heat transfer coefficient. In order to verify the accuracy of the predicted heat flux and the experimental heat flux, experiments using bare surfaces were performed, and the results are shown in Figure 4.8. A considerable deviation could be noticed between the experimental heat flux and the predicted heat flux. The experimental heat flux corresponding to the bare surface was around 50% lower than the predicted one using Dittus Boelter correlation. This effect is due to the fact that the correlation tries to consider a circular heated channel, while our uses a single heated face in a square flow channel.

To tackle this problem, Hua et al. [59] proposed a modified Dittus Boelter correlation to predict the heat flux on cast iron square channels using water as a working fluid, equation (4.1). They used a Reynolds number between 2500 and 25000 with a maximum heat flux of 1000 kW$\cdot$ m^{-2}, a working flow velocity of 0.2 to 2.0 m$\cdot$ s^{-1}, and a pressure between 100 and 300 KPa.

$$q = 2.906 Re^{0.36} Pr^{0.48} \left(\frac{\mu_b}{\mu_w}\right)^{-0.22} \frac{(T_w - T_b)\lambda_l}{d_h}. \tag{4.1}$$

With linear regression, the heat transfer coefficient on the forced convection h_{fc} was found to be

$$h_{fc} = 0.168 Re^{0.62} Pr^{0.545} \frac{\lambda_l}{d_h}. \tag{4.2}$$

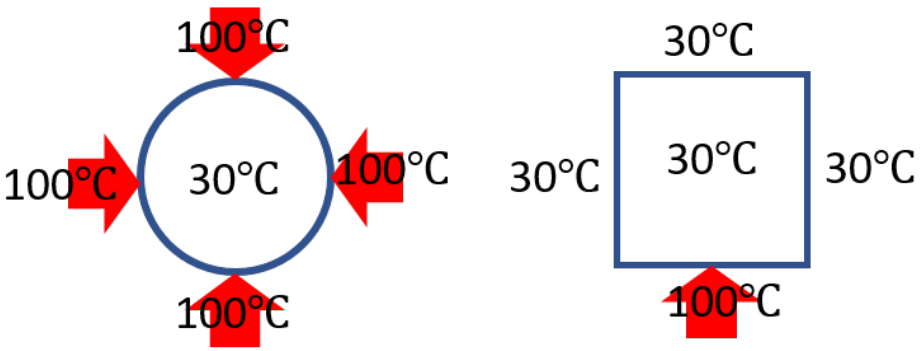

Figure 4.7: Circular tubes and one side heated flow channels.

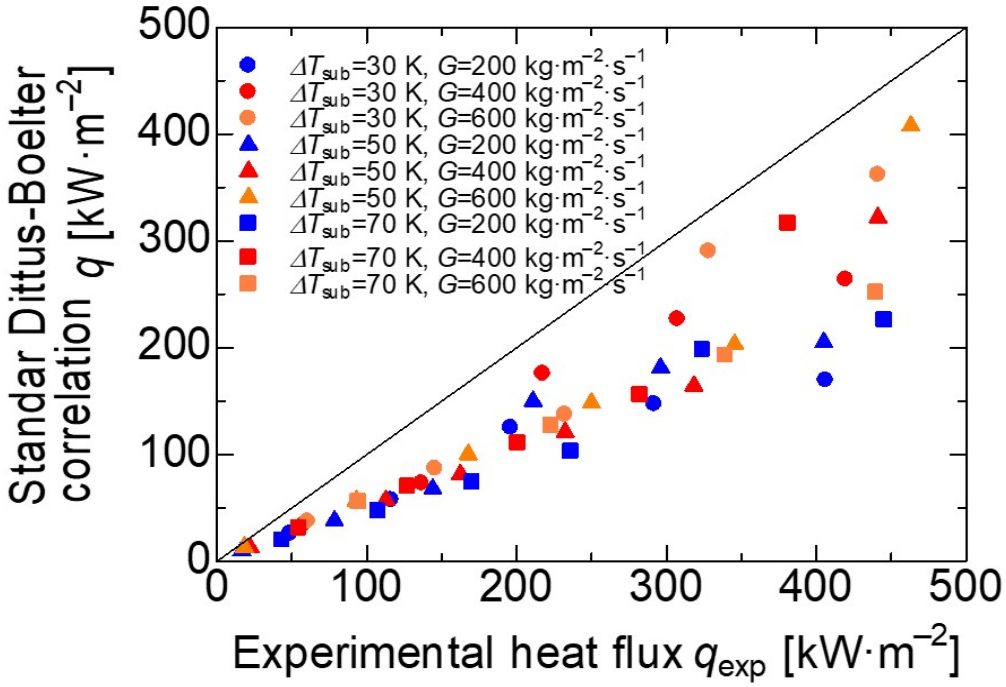

Figure 4.8: Experimental heat flux and predicted heat flux by the standard Dittus Boelter prediction.

The heat flux calculated by the modified Dittus Boelter correlation and the experimental heat flux corresponding to the bare surface is plotted in figure 4.9 where the black line represents the theoretical heat flux prediction.

4.3 Comparison of the calculated heat flux and the experimental heat flux

Figure 4.10 shows the comparison between the experimental heat flux calculated with the Fourier law equation (3.4) and the heat flux calculated with equation (3.5) using the inlet and outlet temperature and enthalpy as parameters. Figure 4.11 shows the sketch for the heat flux calculation using the temperature difference trough the copper body (Fourier law) and the heat flux calculation using the working fluid temperature difference in the inlet and the outlet part of the test section. The results showed an average accuracy between 80 % and 95%, the best accuracy was found for the 1 mm thickness of the porous layer and the lower accuracy was found for the 0.5mm thickness of the porous layer. This high accuracy confirms the good quality of the experimental measurement method. The variation between the experimental heat flux and the predicted heat flux is attributed to the higher number

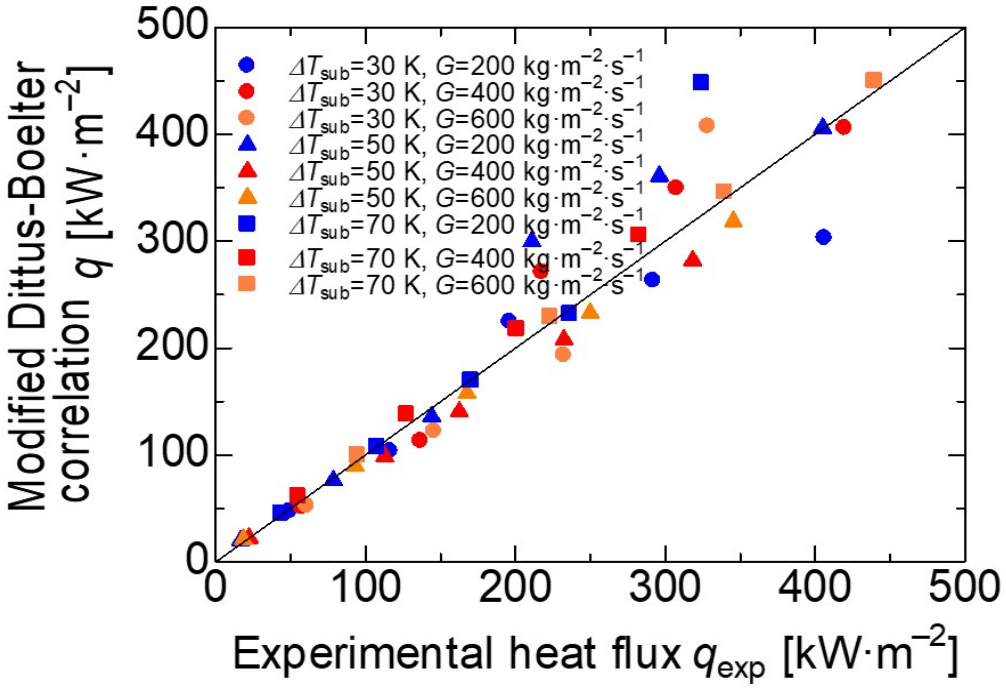

Figure 4.9: Experimental heat flux and predicted heat flux by the Modified Dittus Boelter prediction

of nucleation sites that promote a higher vapor bubble activity in the flow channel. This phenomenon is confirmed at high heat flux where the bubble formation and departure rate is higher. The heat flux ratio was around 80% at heat fluxes higher than 1500 kW· m^{-2}.

4.4 Single-phase heat flux

The enhancement of the heat flux using high-porosity sintered fibers attached to the surface is discussed in this subsection. As parameters, thickness of the porous layer, mass flux, and inlet subcooling temperature are considered. For easy comprehensibility, the results are divided by mass flux and inlet subcooling temperature for each porous layer thickness. The single-phase flow is considered for $\Delta T_{sat} \leq 0$. In the absence of bubbles, the influence of the flow pattern was considered insignificant. Flow patterns with the high-speed camera are not presented in this section due to the absence of bubble formation.

4.4.1 Heat flux for single-phase flow $\Delta T_{sub} = 30$ K $G = 200, 400, 600$ kg·m^{-2}·s^{-1}

The thickness of the porous layer of high-porosity sintered fibers affects the heat flux in the single-phase flow independent of the mass flux conditions. Figure 4.12 shows the results for

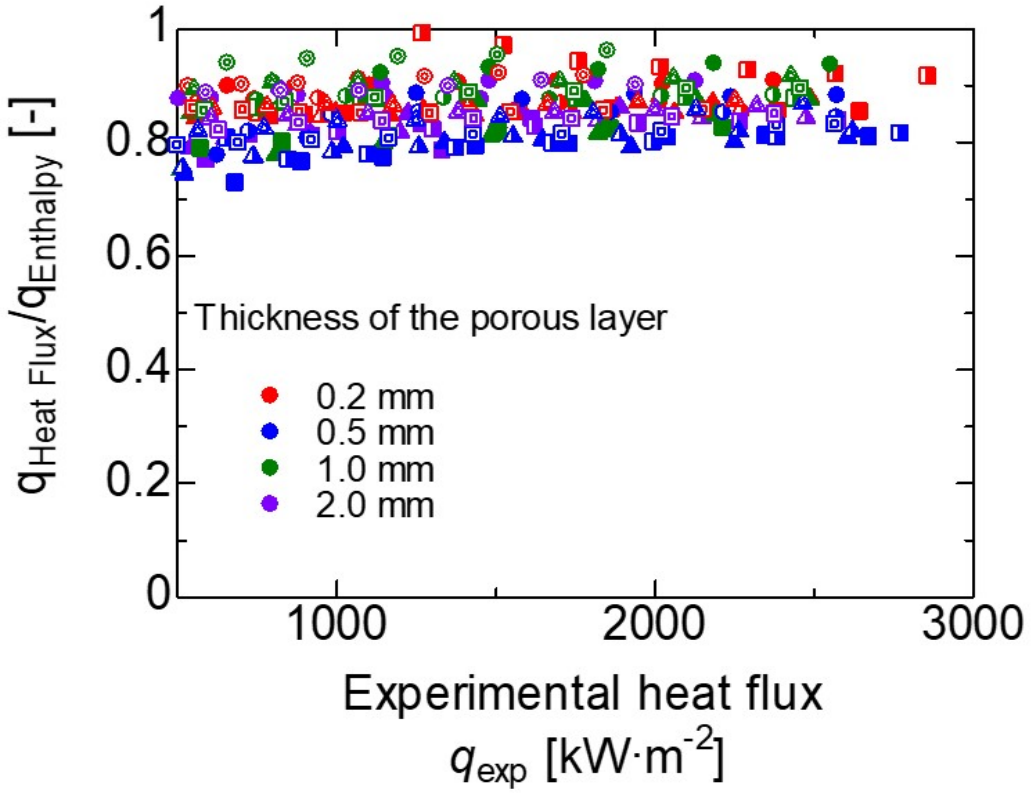

Figure 4.10: Ratio of the experimental heat flux and the calculated heat flux.

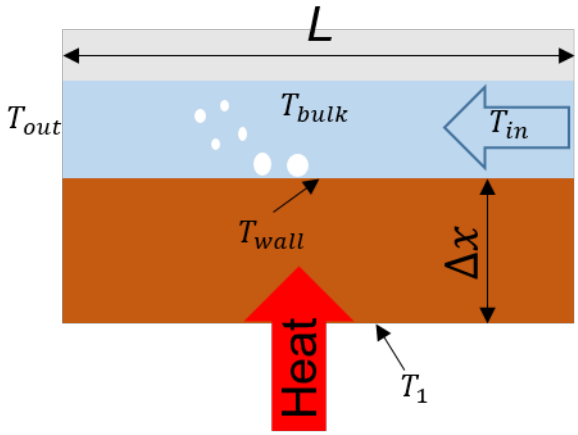

Figure 4.11: Sketch of the test section and the parameters for the heat flux calculation.

the different mass fluxes and all the thicknesses of the porous layer. A different heat flux for each thickness of the porous layer is noticeable. In particular, the 0.2 mm thickness of the porous layer surface shows the highest heat flux, independent to the mass flux conditions. 0.5 mm thickness of the porous layer shows the second best heat transfer performance. Similar values for the heat flux are measured for the bare surface at low and medium mass flux as shown in Figure 4.12b and 4.12c. On the other hand, at high mass fluxes, the heat flux is

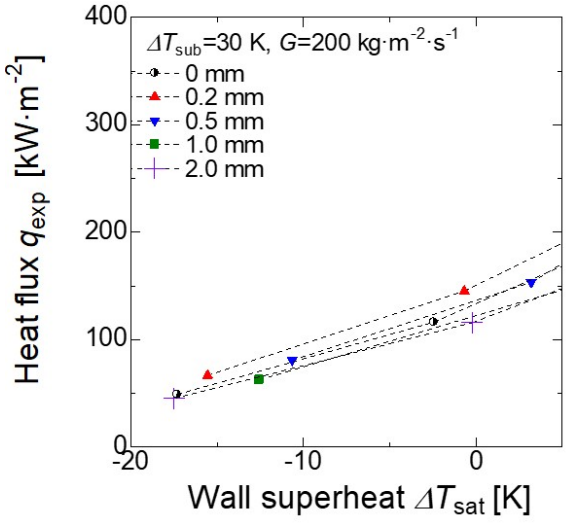

(a) $\Delta T_{sub} = 30$ K, low mass flux

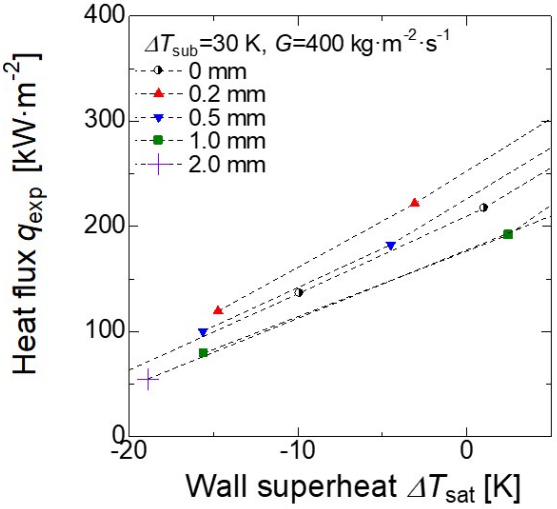

(b) $\Delta T_{sub} = 30$ K, medium mass flux

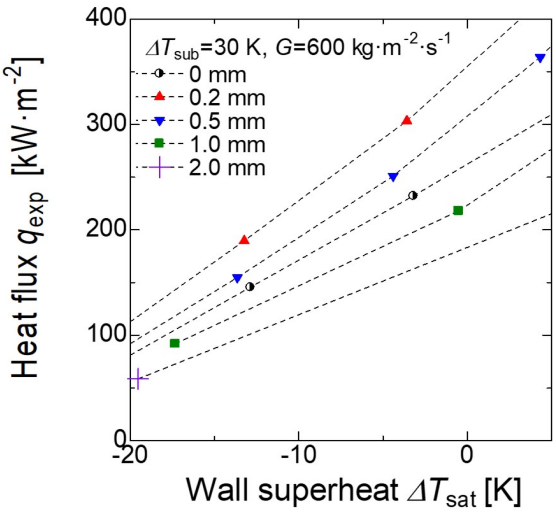

(c) $\Delta T_{sub} = 30$ K, high mass flux

Figure 4.12: Influence of the mass flux on the single-phase heat flux at $\Delta T_{sub} = 30$ K.

totally different for all the surfaces. For the 1 mm and 2 mm thickness of the porous layer showed a lower heat flux than the bare surface (0 mm), which represents a worse performance of the porous material. This effect is attributed to the capillary suction effect and the hydrodynamic limit.

In general terms, the maximum heat flux under low mass flux is between 100 and 150 kW· m^{-2}. The heat flux increases gradually at medium mass fluxes, the maximum heat flux was found between 160 and 230 kW· m^{-2}. Finally, at high mass fluxes conditions, the range of the maximum heat flux was between 190 and 330 kW· m^{-2}. The effect of the thickness of the porous layer on the heat flux at the same wall superheat temperature is more noticeable

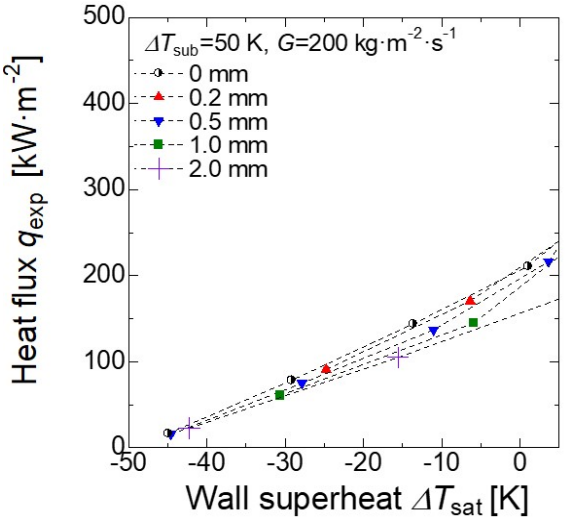

(a) $\Delta T_{sub} = 50$ K, low mass flux

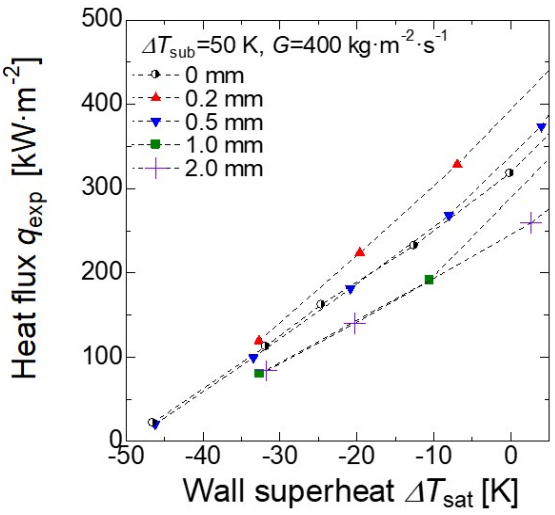

(b) $\Delta T_{sub} = 50$ K, medium mass flux

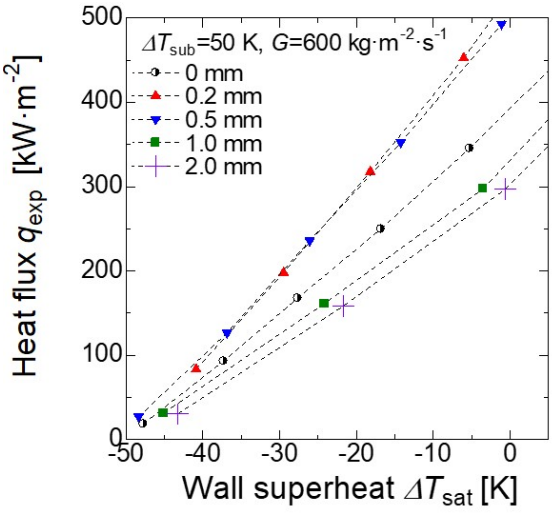

(c) $\Delta T_{sub} = 50$ K, high mass flux

Figure 4.13: Influence of the mass flux on the single-phase heat flux at $\Delta T_{sub} = 50$K.

at high mass fluxes. Around $\Delta T_{sat} = 0$, comparing the 0.2 mm thickness of the porous layer surface and the bare surface, the enhancement of the heat flux is around 40 %, 25%, and 13%, for high, medium, and low mass fluxes, respectively.

4.4.2 Heat flux for single-phase flow $\Delta T_{sub} = 50$ K $G = 200, 400, 600$ kg·m^{-2}·s^{-1}

The degree of inlet subcooling represents another essential factor to consider in the heat transfer process. As mentioned in section 4.4.1, the sintered fibers with low thickness of the porous layer presented an enhancement under all the mass fluxes. However, at low inlet subcooling temperatures (Figure 4.13), the heat flux enhancement was minimal. As shown in the Figure 4.13a, the heat flux of the bare surface (0 mm) and the 0.2 mm porous layer thickness

were similar and could be neglected, the rest of the porous thickness presented a reduction on the heat flux. Figure 4.13b shows the heat flux at medium mass flux, here the 0.2 mm thickness of the porous layer surface presented an enhancement in comparison with the bare surface. 0.5 mm thickness of the porous layer surface, and the bare surface showed a similar heat flux pattern. Nevertheless, the high thickness of the porous layer (1, and 2 mm) reduced the heat flux compared with the bare surface at the same wall superheat temperature. In contrast, at high mass fluxes, the low thickness of the porous layer (0.2, and 0.5 mm) showed a considerable enhancement on the heat flux.

At medium inlet subcooling temperature and low mass flux, the range of heat flux was between 160 and 205 kW$\cdot$ m^{-2} where the maximum heat flux was observed on the bare surface and the minimum on the 2 mm thickness of the porous layer surface 4.13a. At medium mass fluxes, the maximum heat flux fluctuated between the 325 and the 405 kW$\cdot$ m^{-2}. At these conditions, the lowest thickness of the porous layer presented an enhancement of the heat flux by around 25% in comparison with the bare surface 4.13b. The performance at high mass fluxes showed higher heat fluxes. At 0.2 mm and 0.5 mm thickness of the porous layer the heat flux was around 525 kW$\cdot$ m^{-2}. In addition, the minimum heat flux was found for 2 mm thickness of the porous layer. The heat flux enhancement of the two lowest thickness of the porous layer was around 35%, as can be seen in Figure 4.13c.

4.4.3 Heat flux for single-phase flow $\Delta T_{sub} = 70$ **K** $G = 200, 400, 600$ **kg$\cdot$m$^{-2}\cdot$s^{-1}**

The influence of the high subcooling temperature at low mass fluxes was similar at medium and low subcooling temperature under low mass fluxes as explained in section 4.4.1 and 4.4.2, respectively. High-porosity sintered fibers showed a higher heat flux for 0.2 mm and 0.5 mm thickness of the porous layer in comparison with the bare surface (around 300 kW$\cdot$ m^{-2}) . However, the high porous layer thickness showed a decrease in the heat flux (around 200 kW$\cdot$ m^{-2}) that represents a 33% lower heat flux than the bare surface. The same behavior as for the low and medium subcooling temperatures at medium mass flux was found at high subcooling temperature (Figure 4.12b, 4.13b and 4.14b). Nevertheless, at high subcooling temperatures, the 0.2 mm and 0.5 mm thickness of the porous layer surfaces showed a heat flux of around 490 kW$\cdot$ m^{-2}, the 1mm thickness of the porous layer and the bare surface heat

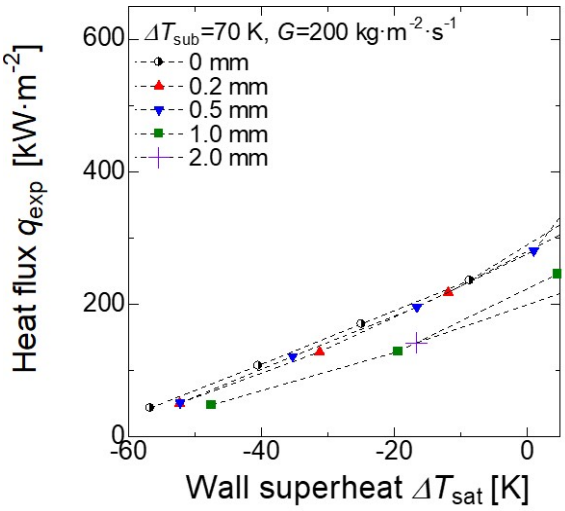

(a) $\Delta T_{sub} = 70$ K, low mass flux

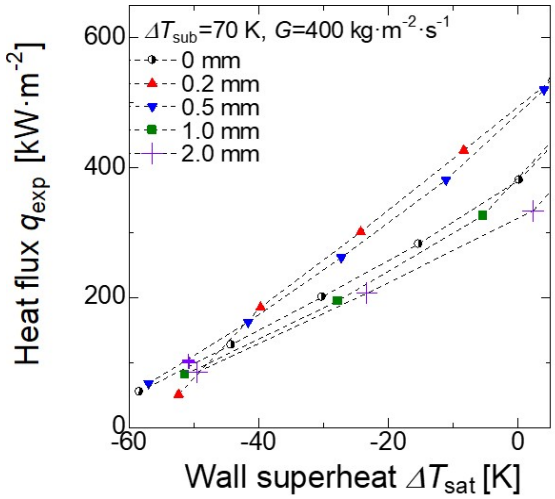

(b) $\Delta T_{sub} = 70$ K, medium mass flux

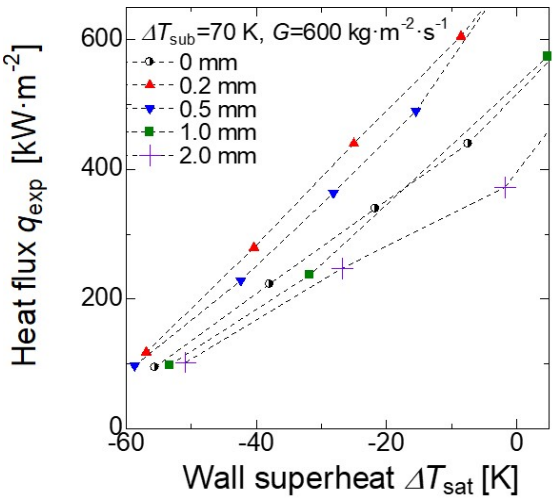

(c) $\Delta T_{sub} = 70$ K, high mass flux

Figure 4.14: Influence of the mass flux on the single-phase heat flux at $\Delta T_{sub} = 70$ K.

flux was found at around 380kW· m^{-2}. Meanwhile, for the 2 mm thickness of the porous layer was around 320 kW· m^{-2}. This represents an enhancement of around 28 % using the low thickness of the porous layer in comparison with the 0 mm surface.

Finally, at high mass flux and high subcooling temperature, the 0.2 mm and 0.5 mm thickness of the porous layer showed a high enhancement in comparison with the bare surface. The low thickness of the porous layer heat flux was around 700 kW· m^{-2} and the bare surface a heat flux around 500 kW· m^{-2}, representing an enhancement of around 40%. A slightly higher heat flux in 1 mm thickness of the porous layer than the bare surface was found, nevertheless, the enhancement is minimal and can be neglected. The wall superheat was considerably lower at high subcooling temperatures; in this case, the minimum wall superheat was around 60 K. Meanwhile, the minimum wall superheat temperature for the medium subcooling temper-

ature (section 4.4.2) was around 45 K, and the low subcooling temperature (section 4.4.1) presented a minimum wall superheat of around 18 K. The wall superheat temperature is not constant according to the inlet subcooling temperature as the data recording started at a copper block B temperature of 60° C.

Table 4.3: Enhancement of the heat flux using high-porosity sintered fibers in comparisson with the bare surface; ◯ enhancement, [-] around the same heat flux, ⊗ no enhancement (decrease).

		Mass flux [kg· m^{-2} ·s^{-1}]		
Thickness of the porous layer [mm]	Subcooling temperature [K]	200	400	600
0.2	30	◯	◯	◯
	50	[-]	◯	◯
	70	[-]	◯	◯
0.5	30	[-]	◯	◯
	50	⊗	◯	◯
	70	[-]	◯	◯
1	30	⊗	⊗	⊗
	50	⊗	⊗	⊗
	70	⊗	[-]	◯
2	30	⊗	⊗	⊗
	50	⊗	⊗	⊗
	70	⊗	⊗	⊗

A general review of the performance of the porous materials for the single-phase is given in Table 4.3. The comparison of the maximum heat flux was compared for the same wall superheat temperature $\Delta T_{sat} = 0K$.

4.4.4 Single-phase heat flux comparison

The heat flux enhancement on the single-phase is shown in Figure 4.15. The best heat flux enhancement was presented on the 0.2 mm thickness of the porous layer surface (red sign on the graph). The following surface 0.5 mm thickness of the porous layer (blue points) also shows a better heat flux in comparison to the bare surface. On the other hand, the heat flux decreased for the high thickness of the porous layer; both the 1 mm and 2 mm thickness of

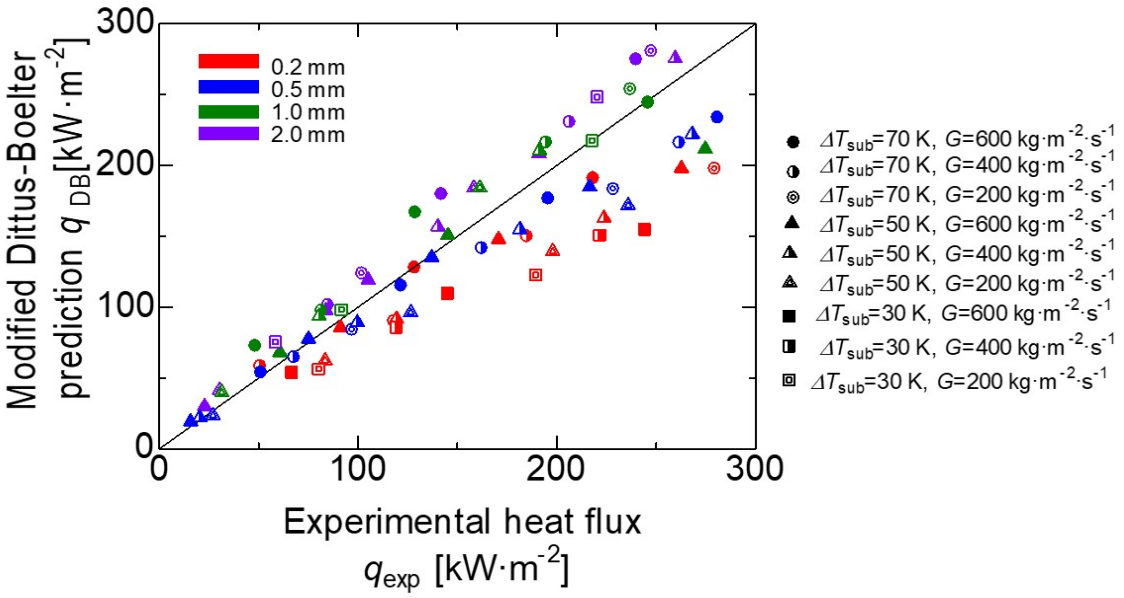

Figure 4.15: Single-phase heat flux for all values of the thickness of the porous layer.

the porous layer surface presented an apparent reduction in the heat flux and an increment on the wall superheat temperature. The enhancement in the heat flux can be attributed to the turbulence generated on the low thickness of the porous layer. However, the high thickness of the porous layer promotes high turbulence that partially blocks the water supply.

4.5 Heat flux for two-phase flow and flow patterns

The subcooled flow boiling, bubble pattern formation, and departure were recorded with a high-speed camera, and heat flux comparison between the all the thickness of the porous layer and the bare surface is explained in this section. The relation between the flow pattern on the porous surface and its direct relation with the heat flux are discussed. For safety reasons, the experiments were stopped at a maximum heat flux of around 2500 kW· m^{-2} or if the wall superheat temperature exceeded the $\Delta Tsat = 70$ K to avoid temperatures close to the polycarbonate melting point as shown in Figure 4.16.

4.5.1 Flow boiling heat flux $\Delta T_{sub} = 30$ K $G = 200, 400, 600$ kg·m^{-2}·s^{-1}

Figure 4.17 shows the results of the subcooled two-phase flow heat flux for four types of porous layer thickness. 0.2, 0.5, and 1 mm thickness of the porous layer showed a heat flux enhancement at the same wall superheat temperature. They also exhibited an earlier onset

Figure 4.16: Melting of the polycarbonate cover.

nucleate boiling point than the bare surface. The abrupt increase of the wall superheat also was suppressed for values of the thickness of the porous materials of 0.2, 0.5, and 1 mm. However, for the case of the 2 mm thickness of the porous layer surface and independently of the mass flux, this heating surface showed the lowest heat transfer performance, and the CHF could not be reached despite the high wall superheat temperature. It was found that the higher mass flux promotes a higher heat flux at the same wall superheat temperature; at the same time, the effect of the thickness of the porous layer is more visible at higher mass fluxes. When the wall superheat temperature value is between 0 K and 20 K, the effect of the mass flux on the heat transfer is more pronounced, see Figures, 4.17a, 4.17b, and 4.17c. The CHF was observed only at medium mass flux on the bare surface as shown in Figure 4.17b at a wall superheat temperature of around 60 K and a heat flux of around 2500 kW$\cdot$ m^{-2}. The abrupt increase for the bare and the 2 mm thickness of the porous layer surface is attributed to the formation of a vapor blanket on the heating surface. In the case of the bare surface, a big bubble is formed that blocks the water supply partially from the heating surface. On the other hand, the formation of the vapor blanket inside the 2 mm thickness of the porous layer is attributed to the higher vapor trap ability. The CHF was not reached because the bubble diameter inside the porous material is lower than the bare surface; thus, the collapse of the smaller bubbles is easier and faster.

The bubble flow pattern formation was analyzed with the high-speed camera. For a medium mass flux, the pattern for the 400 kg$\cdot$m$^{-2}\cdot$s^{-1} was taken as reference. Figure 4.18 shows the flow bubble pattern at the maximum heat flux of each of the porous thicknesses. As mentioned above, the critical heat flux was reached for the bare surface, and the flow pattern is shown in Figure 4.18a. Here one can see a case of transition film boiling; in other words, a big bubble is formed on the heating surface, so nearly no water can reach this

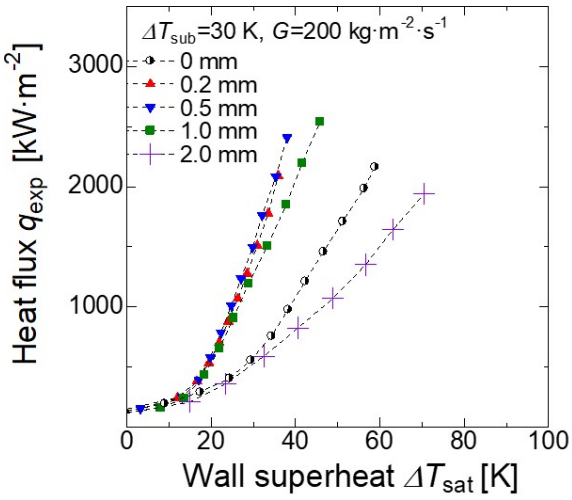

(a) $\Delta T_{sub} = 30$ K, low mass flux

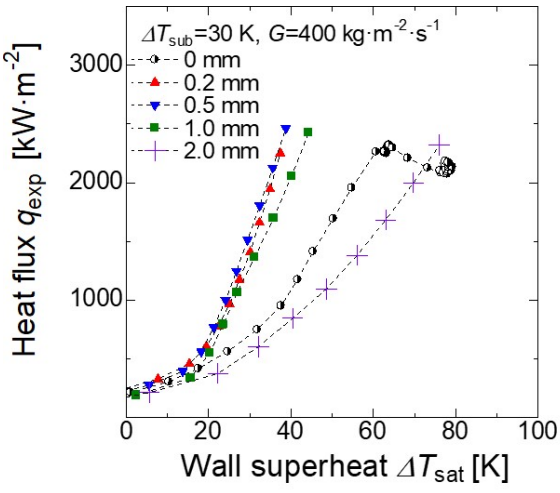

(b) $\Delta T_{sub} = 30$ K, medium mass flux

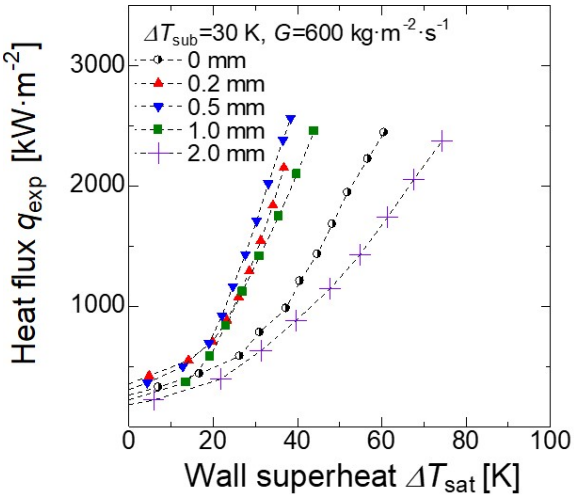

(c) $\Delta T_{sub} = 30$ K, high mass flux

Figure 4.17: Boiling curve for all values of the thickness of the porous layer $\Delta T_{sub} = 30$ K.

area. Therefore, the heat transfer coefficient decreases considerably, and the wall superheat increases abruptly. The water that enters the channel evaporates rapidly after contact with the vapor film. A reduction in the mass flux was also detected; this effect is attributed to the rapid collapse of bubbles and the high pressure inside the channel flow. The CHF was found to be around 2400 kW$\cdot$ m^{-2} with a wall superheat temperature of $\Delta T_{sat} \approx 60$ K. Figure 4.18b shows the flow bubble pattern for the 0.2 mm thickness of the porous layer. The high-speed video analysis showed a similar flow bubble pattern for the bare surface. However, the use of a porous heating area allowed to constantly supply liquid to the surface, so that smaller bubbles and continued departure guaranteed a constant flow inside the porous body and thus a lower wall superheat temperature. This porous thickness also shows a not fully filled vapor channel despite the large size of the bubble which formed on the surface. Water also flows

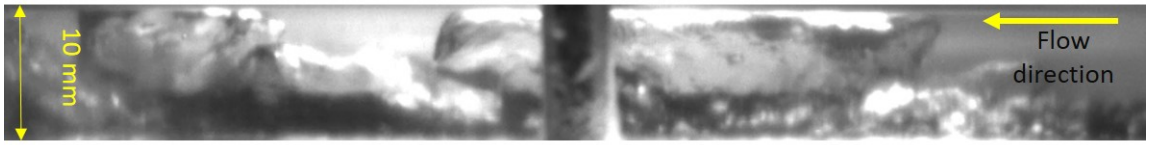

(a) 0 mm thickness of the porous layer; Maximum heat flux 2400 kW· m^{-2}, $\Delta T_{sat} \approx 60$ K

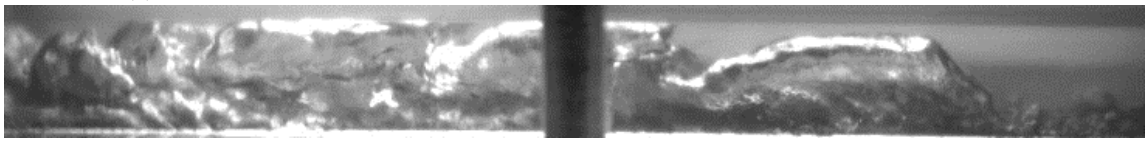

(b) 0.2 mm thickness of the porous layer; Maximum heat flux 2350 kW· m^{-2}, $\Delta T_{sat} \approx 37$ K

(c) 0.5 mm thickness of the porous layer; Maximum heat flux 2500 kW· m^{-2}, $\Delta T_{sat} \approx 40$ K

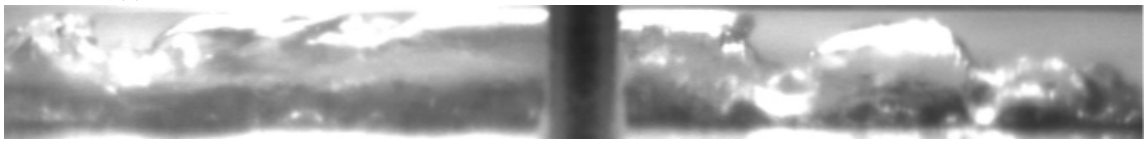

(d) 1 mm thickness of the porous layer; Maximum heat flux 2500 kW· m^{-2}, $\Delta T_{sat} \approx 44$ K

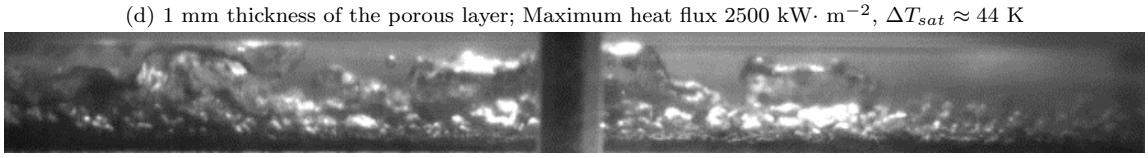

(e) 2 mm thickness of the porous layer; Maximum heat flux 2400 kW· m^{-2}, $\Delta T_{sat} \approx 70$ K

Figure 4.18: Maximum heat flux for each thickness of the porous layer under medium mass flux.

through the upper part of the channel. The inlet part of the flow channel presents a low rate of bubble generation. The maximum heat flux recorded for this porous layer thickness was around 2350 kW· m^{-2}, $\Delta T_{sat} \approx 37$ K. A lower wall superheat temperature at the same heat flux in comparison with the bare surface was found, representing a reduction on the wall superheat of around 39%.

The flow pattern of the 0.5 mm thickness of the porous layer is shown in Figure 4.18c showing a similar behavior for the lowest porous thickness. However, in this case the flow channel is totally covered by a vapor film. Nevertheless, the use of the porous materials can suppress the vapor pressure inside the flow channel so that a constant water supply was obtained and the critical heat flux was not reached. The maximum heat flux was detected around 2500 kW· m^{-2} and a wall superheat temperature $\Delta T_{sat} \approx 40$ K. The 0.5 mm thickness of the porous layer showed a reduction of 33% on the wall superheat temperature in comparison with the bare surface.

A reduction of the wall superheat of around 27% was found for the 1 mm thickness of the

porous layer compared to the 0 mm thickness of the porous layer. The flow pattern shows a vapor film covering most of the heating surface and the flow channel. Smaller bubbles and a constant formation a departure was found on on the porous surface. This effect allows the constant water flow through the inside part of the porous body; as a result, the heating surface is cooled by the working fluid (See 4.18d). This surface presented a similar heat flux to the 0.5 mm surface (2500 kW$\cdot$ m^{-2}).

In comparison with the bare surface, the 2 mm thickness of the porous layer surface presented an increase of the wall superheat at the same heat flux. Nevertheless, the CHF was not reached. The increment on the wall temperature is due to the higher vapor trap ability inside the porous body. In this surface, small vapor bubbles are generated inside the porous body, the bubbles coalescence in bigger bubbles making more difficult the departure trough the porous medium and just small bubbles can scape from the porous body, these bubbles coalescence and depart in the outside of the porous body . The flow bubble pattern is shown in Figure 4.18e, in the picture is shown a group of smallest bubbles that coalescence after leaving the porous medium. Due to the small diameter, lower pressure and lower energy, they are condensed. A constant mass flux at lower pressure in comparison with the bare surface was observed.

4.5.2 Flow boiling heat flux $\Delta T_{sub} = 50$ **K** $G = 200, 400, 600$ **kg$\cdot$m$^{-2}\cdot$s^{-1}**

The boiling curve at medium inlet subcooling temperature is shown in Figure 4.19. With the exception of the 2 mm porous thickness, the rest of the surfaces presented an apparent reduction of the wall superheat temperature at the same heat flux. The increment on the wall superheat is due to the fact that vapor tends to accumulated and form a big vapor bubble, blocking partially the water supply in the heating surface. The reduction in the wall superheat was attributed to the increase of nucleation sites, the number of vapor escape channels, and the wettability. The ONB also was shifted to a higher wall superheat temperature (same effect as described in section 4.5.1), the heat flux also increased. This effect is attributed to two main effects; the macro convection due to the working fluid motion and the evaporation of the liquid layer evaporation between the heating surface and the generated bubbles. However, independent of the mass flux, all the boiling curves converged in one point near to the CHF called “transition to the fully developed boiling”. Before this point, in the film boiling

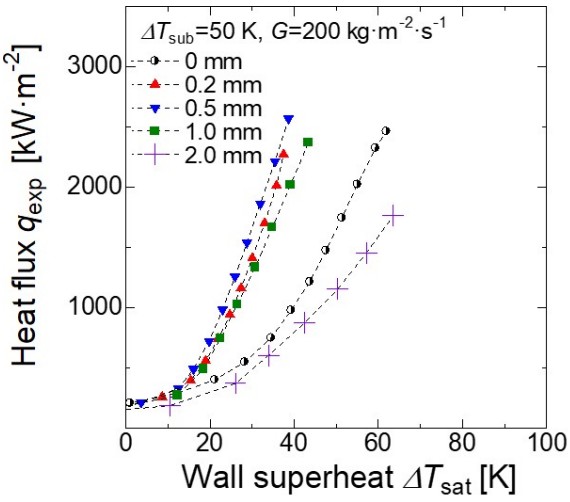

(a) ΔT_{sub} = 50 K, low mass flux

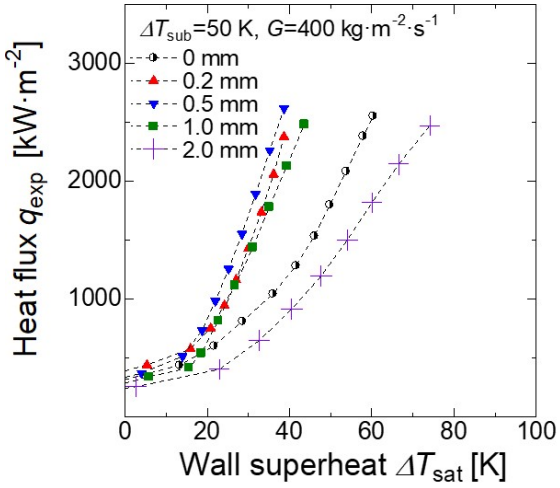

(b) ΔT_{sub} = 50 K, medium mass flux

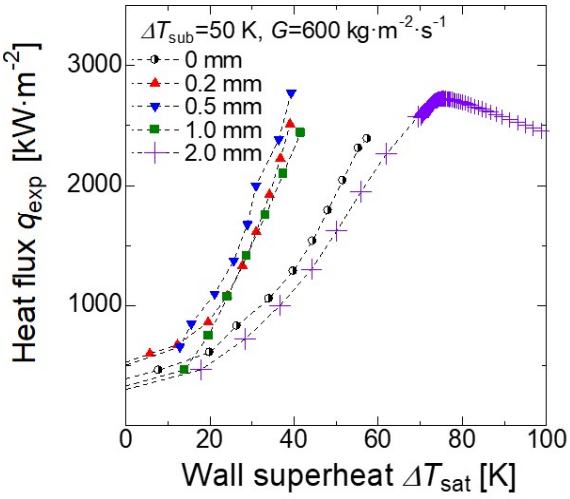

(c) ΔT_{sub} = 50 K, high mass flux

Figure 4.19: Boiling curve for all values of the thickness of the porous layer ΔT_{sub} = 50 K.

regime, the effects of the macro convection became less; however, the layer evaporation effect prevailed.

Unlike low subcooling inlet temperature, the CHF was not reached for the bare surface; however, the 2 mm thickness of the porous layer surface reached the CHF at high mass flux as shown in Figure 4.19c. The experiments using the 0, 0.2, 0.5, 1 mm thickness of the porous layer were terminated when they reached the heat flux limit; on the other hand, the 2 mm thickness of the porous layer was stopped after reaching the wall superheat temperature limit. In general terms, at medium inlet subcooling temperature, the highest heat flux was detected for the 0.5 mm thickness of the porous layer, followed by the 0.2 mm and finally the 1mm. The 2 mm thickness of the porous layer presented a decrease in the heat transfer performance regardless of the mass flux.

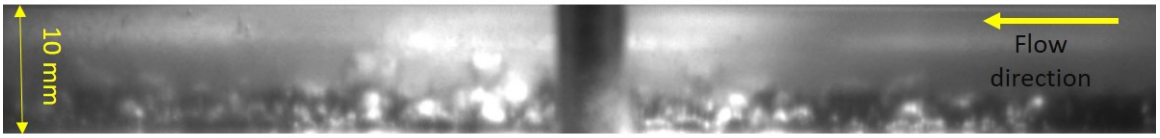

(a) 0 mm thickness of the porous layer; Maximum heat flux 2500 kW· m^{-2}, $\Delta T_{sat} \approx 60$ K

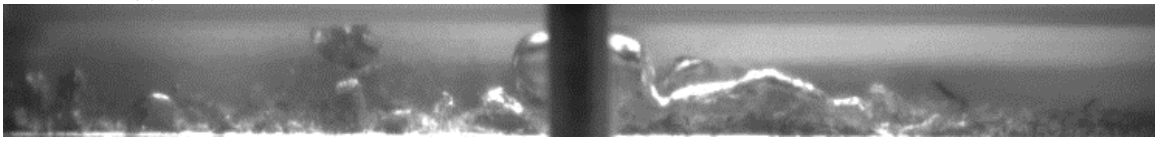

(b) 0.2 mm thickness of the porous layer; Maximum heat flux 2450 kW· m^{-2}, $\Delta T_{sat} \approx 39$ K

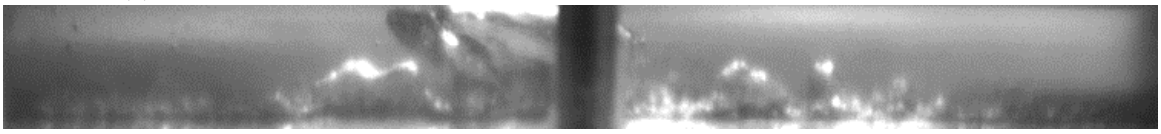

(c) 0.5 mm thickness of the porous layer; Maximum heat flux 2500 kW· m^{-2}, $\Delta T_{sat} \approx 40$ K

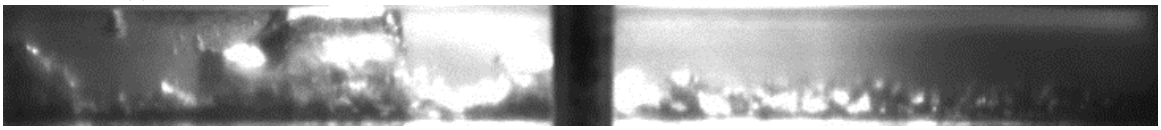

(d) 1 mm thickness of the porous layer; Maximum heat flux 2500 kW· m^{-2}, $\Delta T_{sat} \approx 45$ K

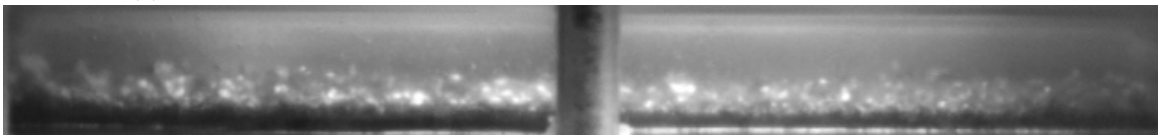

(e) 2 mm thickness of the porous layer; Maximum heat flux 2500 kW· m^{-2}, $\Delta T_{sat} \approx 70$ K

Figure 4.20: Maximum heat flux for each thickness of the porous layer under medium mass flux.

In order to compare the flow bubble patterns at the same mass flux (similar conditions as the section 4.5.1), the working fluid pattern at 400 kg·m^{-2}·s^{-1} at medium inlet subcooling temperature is shown in Figure 4.20. In comparison with the flow bubble pattern at low subcooling inlet temperatures (see Figure 4.18), a clear reduction in the size, formation, and departure rate could be seen. This effect was attributed to the inlet temperature that affects the bulk temperature farthest from the saturation temperature.

For high inlet subcooling temperatures, the bubble formation was reduced to small bubbles outside the porous body with a high departure rate. On the bare surface, the vapor blanket and the CHF was reached, unlike the case with low water subcooling temperatures. Nevertheless, a thin film vapor covers the surface; this increases the wall superheat temperature. No hightened boiling activity was found for the heating surface. The maximum heat flux of the bare surface was around 2500 kW· m^{-2} with a wall superheat temperature of 60 K.

Bubble formation was more marked for the 2 mm thickness of the porous layer. Figure 4.20b shows a clear increase in the number of bubbles that departed from the porous body; the

bubbles that separeted from the porous body coalescence in a medium-size bubble and are carried away the channel by flow. A considerable reduction of $\Delta T_{sat} \approx 20$ K in comparison with the bare surface was found. The maximum heat flux using the 0.2 mm thickness of the porous layer was around 2500 kW$\cdot$ m^{-2}. This represents a reduction of 35% on the wall superheat in comparison with the bare surface.

Figure 4.20c shows the flow pattern for the 0.5 mm thickness of the porous layer. For the bare surface, bubbles rarely coalesce. However, the 0.5 mm thickness of the porous layer promoted the bubble coalescence and thus, increased the heat flux at lower wall superheat. The bubbles are mainly generated at the center of the heating surface, they coalesce and condense; due to this effect, the wall superheat temperature it kept lower that for the bare surface. Observe that the wall superheat temperature was reduced by around 33%.

Higher thickness of the porous layer promoted a higher number of bubbles, higher departure and coalescence rate as shown in Figure 4.20d. Bubbles are generated inside the porous body, and the ability to trap vapor leads to coalescence of the departed bubbles. A considerably bigger bubble than in the case of low thickness of the porous layer surface was recorded. However, the water supply is not affected due to water temperature at the inlet. The surface with thickness of the porous layer reached a maximum heat flux of around 2500 kW$\cdot$ m^{-2} at a wall superheat temperature of 45 K, in other words, a reduction of around 25% compared with the bare surface.

In contrast to the previous thickness of the porous layer surfaces, the 2mm thickness of the porous layer surface presented an increase of the wall superheat temperature at the same heat flux compared to the bare surface. The number of bubbles generated outside the porous body is marginal; the vapor is trapped inside the porous body due to the high thickness of the porous layer. A big bubble is formed inside the porous body and just small bubbles can scape trough the porous body. The small bubbles that can escape from the inside to the outside part of the body are rapidly collapsed and removed by the water flow. As a result, no big sized bubbles (almost cover the complete flow channel height) were detected on the channel flow as shown in Figure 4.20e. Due to the difficulty of the water to enter inside the porous body, the vapor trapped on the porous body increase the wall temperature considerably. The experiment was stopped for safety reasons; here, the maximum heat flux was around 2500 kW$\cdot$ m^{-2}, and a wall superheat temperature of around 70 K which represents an increment of 16% in comparison with the 0 mm thickness of the porous layer.

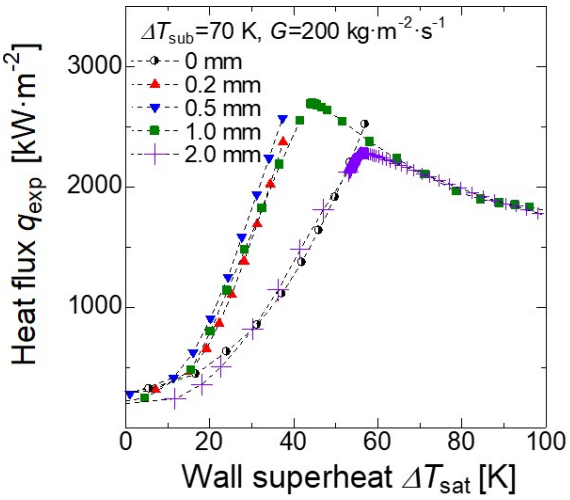

(a) $\Delta T_{sub} = 70$ K, low mass flux

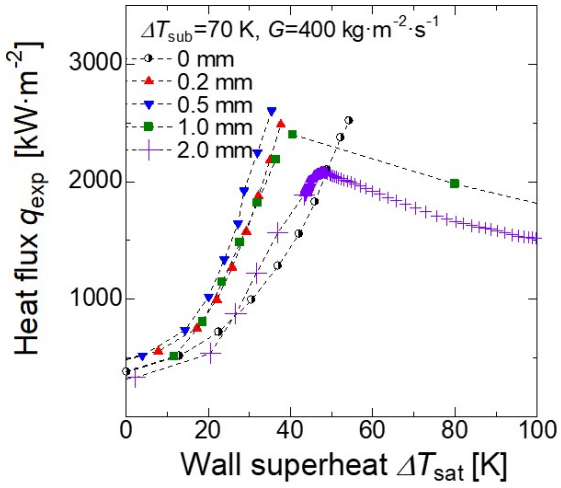

(b) $\Delta T_{sub} = 70$ K, medium mass flux

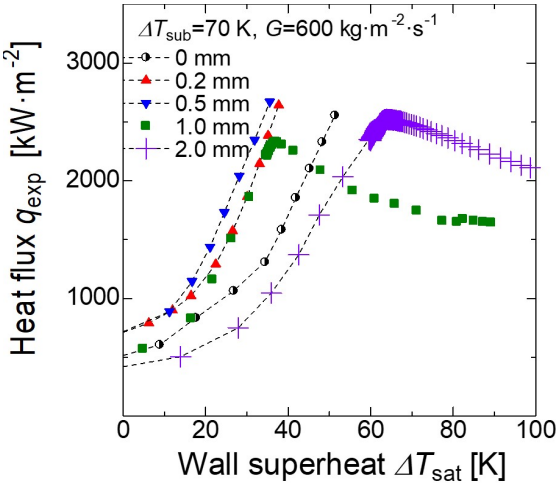

(c) $\Delta T_{sub} = 70$ K, high mass flux

Figure 4.21: Boiling curve for all values of the thickness of the porous layer $\Delta T_{sub} = 70$ K.

4.5.3 Flow boiling heat flux $\Delta T_{sub} = 70$ K $G = 200, 400, 600$ kg·m^{-2}·s^{-1}

As expected, at high inlet subcooling temperatures, the heat flux increased for the same wall superheat temperature and the same mass flux for each thickness of the porous layers. However, six cases of critical heat flux were found. These six cases were detected on the high thickness of the porous layer, three cases for the 2 mm thickness of the porous layer for all the mass fluxes, and three cases for the 1 mm thickness of the porous layer as shown in Figure 4.21. The abrupt increase of the wall superheat is due to the high subcooling temperature at the inlet, the ability to trap vapor lead to the effect that the generated bubbles escaped with difficulty from the porous body, and the water rapidly collapsed the tiny bubbles that could escape at low temperature.

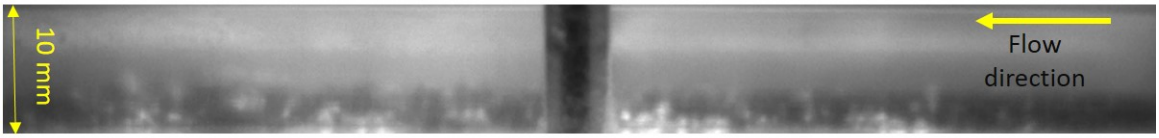

(a) 0 mm thickness of the porous layer; Maximum heat flux 2500 kW· m^{-2}, $\Delta T_{sat} \approx 55$ K

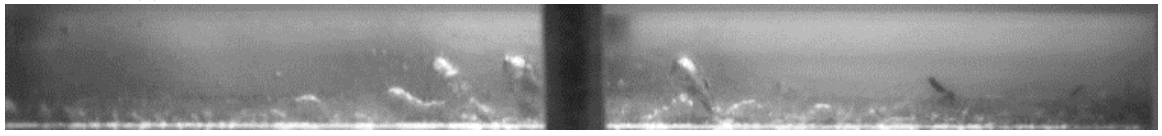

(b) 0.2 mm thickness of the porous layer; Maximum heat flux 2450 kW· m^{-2}, $\Delta T_{sat} \approx 39$ K

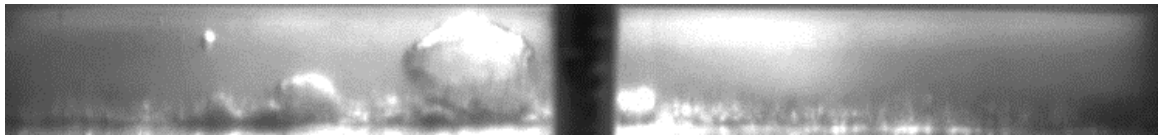

(c) 0.5 mm thickness of the porous layer; Maximum heat flux 2550 kW· m^{-2}, $\Delta T_{sat} \approx 40$ K

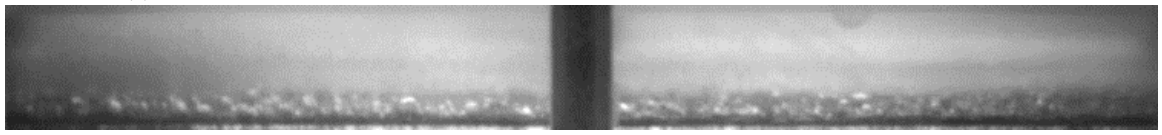

(d) 1 mm thickness of the porous layer; Critical heat flux 2400 kW· m^{-2}, $\Delta T_{sat} \approx 40$ K

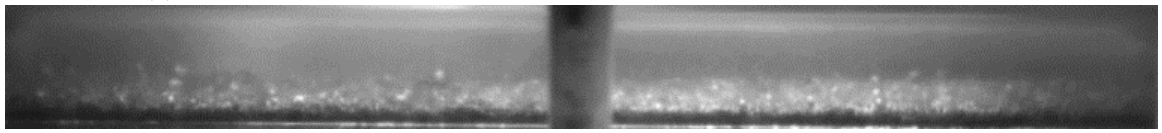

(e) 2 mm thickness of the porous layer; Critical heat flux 2000 kW· m^{-2}, $\Delta T_{sat} = 45$ K

Figure 4.22: Maximum heat flux for each thickness of the porous layer under high mass flux.

In the particular case of the 1 mm thickness of the porous layer surface, an enhancement on the heat flux at the same wallsuperheat in comparison with the bare surface; however, after reaching a certain wall superheat temperature, the CHF was reached at a lower heat flux than for the bare surface. In Figure 4.21, a violent increment on the wall superheat for the 1 mm and 2 mm thickness of the porous layer surfaces was identified. This unexpected jump in the graphs is due to the fact that the vapor blanket for thick porous layer acts as insulation between the water and the copper block, thus the CHF is reached and film boiling developed. Due to the abrupt increment on the wall super heat and for safety conditions, after the critical heat flux point the data was recorded constantly, thus the plot on the graph corresponds to unstable conditions.

On the other hand, the low thickness of the porous layer surfaces presented an enhancement on the heat flux in comparison with the bare surface; the abrupt increment on the wall superheat also was controlled, none of the low thickness of the porous layer reached the CHF. The wall superheat temperature ΔT_{sat} was lower than 40 K for all the three mass fluxes. Similar to the results in the sections 4.5.1 and 4.5.2, the low thickness of the porous

layer exhibited an enhancement of the heat flux; this phenomenon is attributed to the higher number of nucleation sites and the relative low vapor trap ability. At low subcooling inlet temperatures, the CHF was easily reached on the bare surface, in the high subcooling degree temperatures where the high thickness of the porous layer reached the CHF.

The high subcooling inlet temperature flow pattern is shown in Figure 4.22. Here, a considerable reduction in the number of bubbles was detected in comparison to the medium and low subcooling temperature. The bare surface shows a high number of small bubbles; however, they rarely coalescence, and they collapse rapidly after departing from the surface. These phenomena produce a thin vapor layer that covers the heating surface and blocks the water supply, as shown in Figure 4.22a. The maximum heat flux reached on the bare surface was around 2500 kW$\cdot$ m^{-2}, and a wall superheat temperature $\Delta T_{sat} \approx 55$ K.

Figure 4.22b shows the flow pattern o the 0.2 mm thickness of the porous layer; it shows a bubble formation and coalescence rate relatively higher than the bare surface. This effect produces a constant bubble departure and constant water supply through the heating surface. As a result, lower superheat temperature at the same heat flux was detected. The CHF was not reached, and the maximum heat flux was similar to the bare surface. However, the wall superheat temperature was reduced by around 16 K that represents an enhancement of around 30%.

Bigger size bubbles was formed by the coalescence of small bubbles on the 0.5 mm thickness of the porous layer (see Figure 4.22c). The nucleation site density is higher than for the 0.2 mm thickness of the porous layer surface, and the facility of the coalescence is also higher. On the center of the heating surface, a big sized bubble is generated and rapidly condensed due to the high subcooling temperature, in addition to small bubbles present in all the top parts of the surface. Once again, this thickness of the porous layer showed the best heat flux enhancement, and the lowest wall superheat temperature. The maximum heat flux was around 2550 kW$\cdot$ m^{-2} and a wall superheat temperature $\Delta T_{sat} \approx 40$ K.

The lower number of bubbles that coalesce was recorded on the 1 mm thickness of the porous layer as shown in Figure 4.22d. Despite the fact that the bubbles did not cause coalescence, the formation and departure rate is high, allowing the heat removal from the surface. The low water inlet subcooling temperature rapidly condenses the bubbles, and thus the bubbles are replaced by new bubbles, and the ability to supply water is not constant; though the wall superheat was reduced, the CHF was reached before 2500 kW$\cdot$ m^{-2}. The abrupt

Table 4.4: Enhancement of the heat flux using high-porosity sintered fibers in comparison with the bare surface in the subcooled flow boiling regime; ◯ enhancement, [-] around the same heat flux, ⊗ no enhancement (reduction).

		Mass flux [kg· m^{-2} ·s^{-1}]		
Porous thickness [mm]	Subcooling temperature [K]	200	400	600
0.2	30	◯	◯	◯
	50	◯	◯	◯
	70	◯	◯	◯
0.5	30	◯	◯	◯
	50	◯	◯	◯
	70	◯	◯	◯
1	30	◯	◯	◯
	50	◯	◯	◯
	70	◯[CHF]	◯[CHF]	◯[CHF]
2	30	⊗	⊗	⊗
	50	⊗	⊗	⊗[CHF]
	70	[-][CHF]	◯[CHF]	◯[CHF]

increment on the high thickness of the porous layer was a consequence of the vapor stocked inside the porous body, and the difficulty to coalescence promoted the CHF. A similar flow pattern was visualized on the 2 mm thickness of the porous layer surface. Also, the CHF was reached due to the high trap ability on the high thickness of the porous layer. The bubbles that can escape from the porous body collapse immediately, and they do not coalesce with other tiny bubbles. The vapor activity was almost marginal on this surface, as shown in Figure 4.22e. The CHF was reached at 2000 kW· m^{-2}.

Table 4.4 shows a resume of heat flux enhancement using high-porosity sintered fibers in comparison with the bare surface at a wall superheat temperature $\Delta T_{sat} = 30$ K. In general, the lowest thickness of the porous layer (0.2 mm) surface showed a considerable enhancement in the heat flux and reduced the wall superheat temperature. The 1 mm and 2 mm thickness of the porous layer presented an enhancement in the heat flux. However, at high subcooling inlet temperature presented a faster CHF and an abrupt increment on the wall superheat that is dangerous for the cooling system operate conditions.

Figure 5.5 shows the maximum heat flux for each of the thickness of the porous layer;

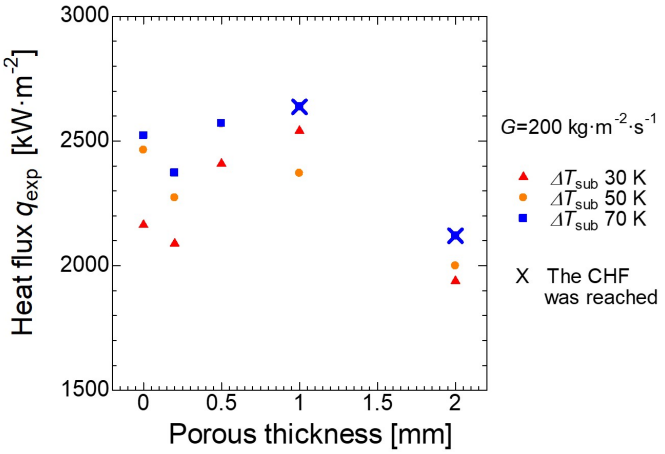

(a) Maximum heat flux reached for each thickness of the porous layer at low mass flux

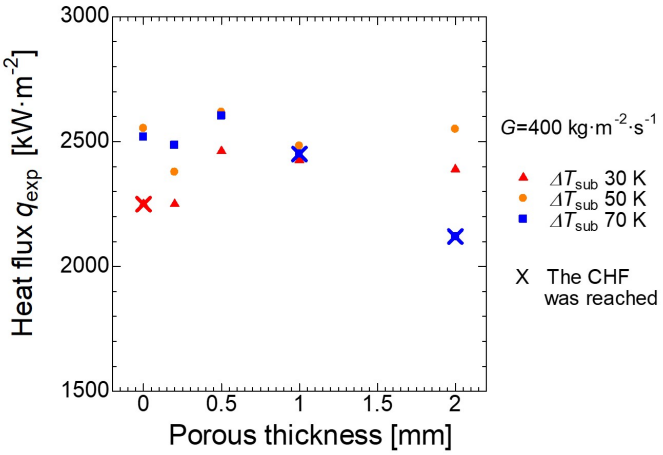

(b) Maximum heat flux reached for each thickness of the porous layer at medium mass flux

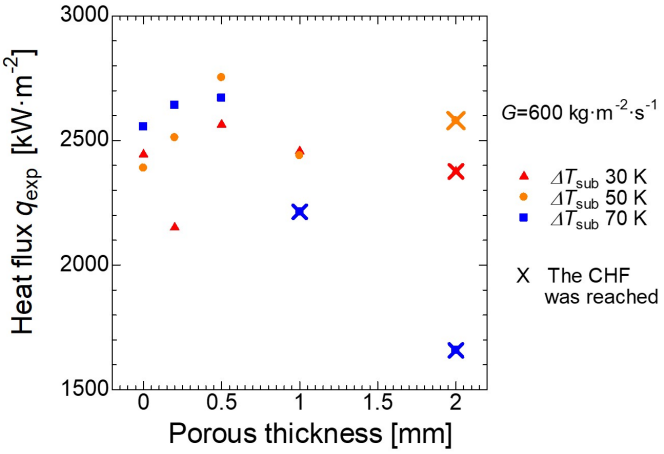

(c) Maximum heat flux reached for each thickness of the porous layer at high mass flux

Figure 4.23: High-porosity sintered fibers and bare surface heat flux performance.

the cross mark represents that the critical heat flux was reached before the 2500 kW·m $^{-2}$. It is evident that the CHF was reached at high mass flux and high subcooling temperature

when the high thickness of the porous layer was used, as shown in Figure 4.23c. The best performance on the heat flux was found for the low thickness of the porous layer; in addition to the lower wall superheat temperature, the CHF was not reached in any of the cases. The CHF was found for the bare surface at medium mass flux and low subcooling inlet temperature. However, for the rest of the cases, the CHF was not reached. The 1 mm thickness of the porous layer was a case for a CHF at high subcooling temperature and medium mass flux. The same case was found on the 2 mm thickness of the porous layer (see Figure 4.23b). Maximum heat flux for the low mass flux is plotted in Figure 4.23a. Here a considerable maximum heat flux reduction for the 2 mm thickness of the porous layer was found. In addition, the CHF was reached at a high subcooling temperature for both cases. Once again, the low thickness of the porous layer presented the best performance; in particular, the 0.5 mm thickness of the porous layer showed the higher heat flux at lower wall superheat temperature.

4.6 Flow bubble pattern comparison at the same heat flux

To compare the reduction of the wall superheat at the same heat flux, 0.2 mm was considered as the low thickness of the porous layer, and 2 mm was considered as the high thickness of the porous layer. For those two samples, in addition to the bare surface, the bubble flow pattern is analyzed.

Figure 4.24, 4.25, and 4.26 show the vapor bubble formation on the channel flow for the 0 mm, 0.2 mm, and 2 mm thickness of the porous layer, respectively. The flow bubble patter was recorded at an interval from 0.0 to 0.03 seconds. It is noticeable that the low thickness of the porous layer promotes bubble generation and increases the bubble formation and departure rate compared to the bare surface. The porous surface increases the number of nucleation sites, and the low porous thickness reduces the vapor trap ability, allowing the bubbles coalesce. The constant departure of generated bubbles allows the water to penetrate the porous body and keep the surface wet.

On the other hand, the use of high thickness of the porous layer reduces the bubble formation outside the porous body; this phenomenon is attributed to ability to trap vapor, so that, bubbles find it more difficult to escape from the porous body and the small bubbles that escape collapse rapidly. As a result, the wall superheat temperature increases. Figure 4.27 shows the ability to trap vapor and the bubble coalescence for low and high thickness of the

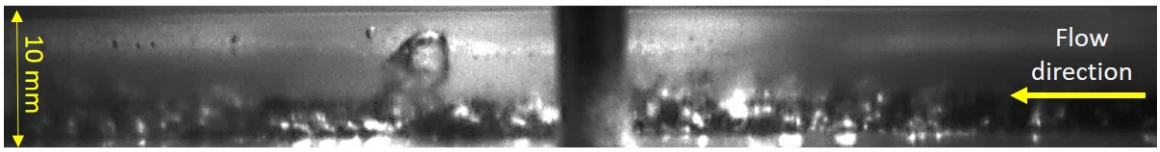

(a) Flow bubble pattern at maximum heat flux 2500 kW· m^{-2}, $\Delta T_{sat} \approx 60$ K, 0 seconds

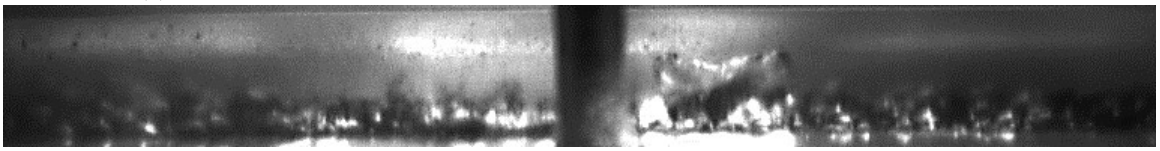

(b) Flow bubble pattern at maximum heat flux 2500 kW· m^{-2}, $\Delta T_{sat} \approx 60$ K, 0.02 seconds

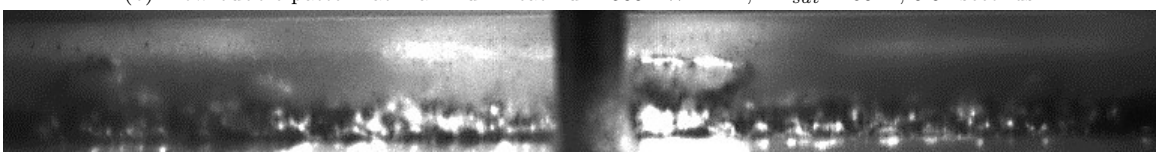

(c) Flow bubble pattern at maximum heat flux 2500 kW· m^{-2}, $\Delta T_{sat} \approx 60$ K, 0.03 seconds

Figure 4.24: Bubble flow pattern on the bare surface at the maximum heat flux, medium mass flux and medium inlet subcooling temperature.

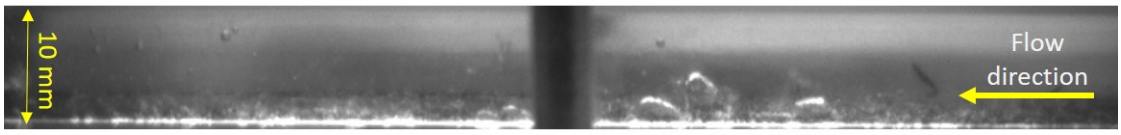

(a) Flow bubble pattern at maximum heat flux 2500 kW· m^{-2}, $\Delta T_{sat} \approx 40$ K, 0 seconds

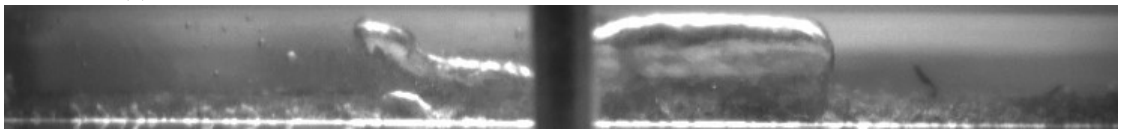

(b) Flow bubble pattern at maximum heat flux 2500 kW· m^{-2}, $\Delta T_{sat} \approx 40$ K, 0.02 seconds

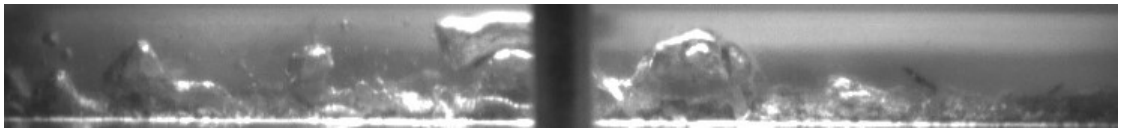

(c) Flow bubble pattern at maximum heat flux 2500 kW· m^{-2}, $\Delta T_{sat} \approx 40$ K, 0.03 seconds

Figure 4.25: Bubble flow pattern on the 0.2 mm thickness of the porous layer surface at the maximum heat flux, medium mass flux and medium inlet subcooling temperature.

porous layer promoted by the sintered fibers attached on the surface.

Figure 4.24 shows the flow bubble pattern on the bare surface. The picture shows a low bubble vapor generation and departure rate. In addition, coalescence and condensation of the bubbles is slow. Figure 4.24a shows the bubble departure from the surface, after 0.2 seconds (Figure 4.24b) the coalescence of the bubbles to a relatively small bubble that did not cover the flow channel. The collapse of the bubbles did not occur immediately, and the movement of the bubble in the flow is slow (Figure 4.24c). The bubble formation and departure rate was an improvement by the low porous thickness as shown in Figure 4.25 where small and

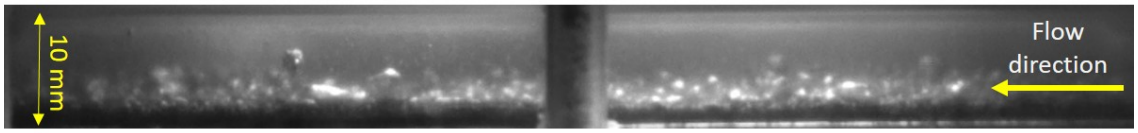

(a) Flow bubble pattern at maximum heat flux 2500 kW· m^{-2}, $\Delta T_{sat} \approx 75$ K, 0 seconds

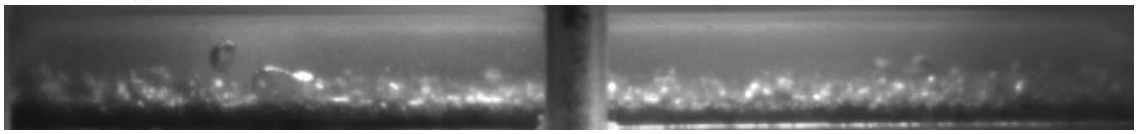

(b) Flow bubble pattern at maximum heat flux 2500 kW· m^{-2}, $\Delta T_{sat} \approx 75$ K, 0.02 seconds

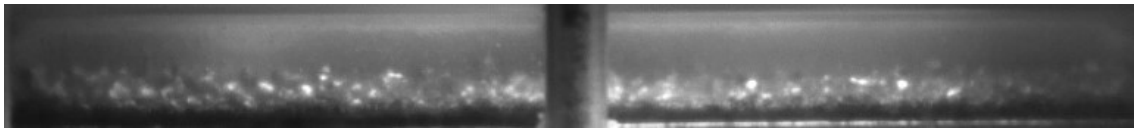

(c) Flow bubble pattern at maximum heat flux 2500 kW· m^{-2}, $\Delta T_{sat} \approx 75$ K, 0.03 seconds

Figure 4.26: Bubble flow pattern on the 2.0 mm thickness of the porous layer surface at the maximum heat flux, medium mass flux and medium inlet subcooling temperature.

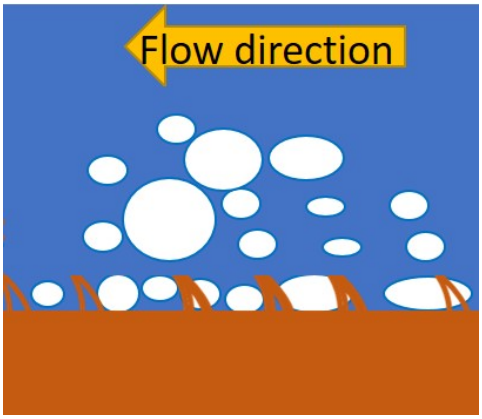

(a) Low thickness of the porous layer surface

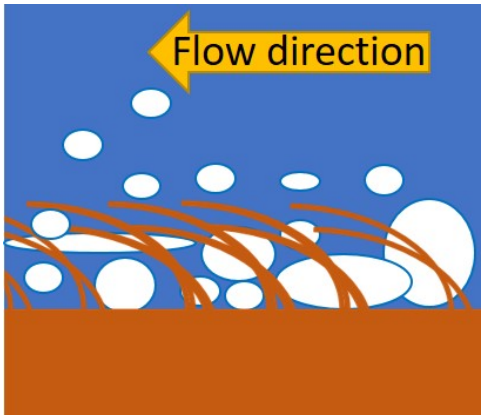

(b) High thickness of the porous layer surface

Figure 4.27: Mechanism which determined the ability to trap vapor for porous layers of low and high thickness of the porous layer.

medium-size bubbles escaped and departed from the surface; after 0.02 seconds, the bubbles increased their size and coalesced to a considerably bigger bubble in the center of the heating surface, see Figure 4.25b. Immediately after the big bubble is formed it collapses and allows a constant water supply, as shown in the Figure 4.25c.

Contrarily to the explained in the above paragraph, when the high thickness of the porous layer is used, the bubble formation and departure rate are almost marginal. It is difficult to identify the bubble flow pattern because the vapor is trapped in the porous layer. Most of the vapor stays inside the porous body, and just some small bubbles can escape. They collapse immediately, and they rarely form bigger bubbles. The accumulated vapor in the porous body blocks the inflow of cooled water and maintains a higher wall temperature than

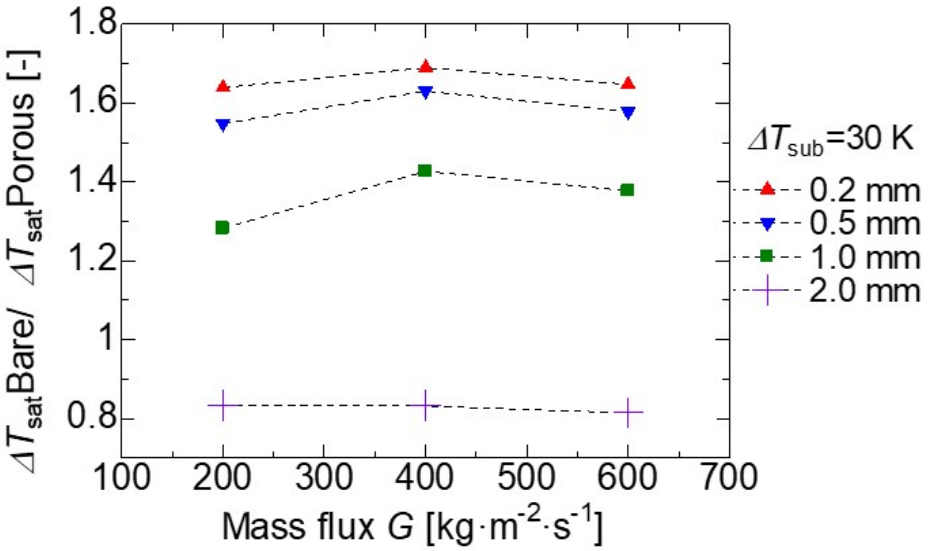

Figure 4.28: Ratio enhancement of the maximum ΔT_{sat} for the bare and the porous surface at low inlet subcooling temperature.

the bare surface, as shown in Figure 4.26.

4.7 Enhancement of the wall superheat

To summarize the effect of the thickness of the porous layer attached on the surface, the ratio of the maximum ΔT_{sat} for the bare and the porous surface under the three different inlet subcooling temperatures are plotted in the Figures 4.28, 4.29, and 4.30. The wall temperature was considered at the maximum heat flux that each surface reached, without consideration if the surface reached the CHF or not.

Figure 4.28 shows the ratio for the enhancement of the wall superheat temperature in comparison with the bare surface. The results show a noticeable reduction in the wall superheat temperature of around 1.6 times. The 1 mm thickness of the porous layer also presented an enhancement of around 40% higher than the bare surface. Contrary to the low thickness of the porous layer, the 2 mm thickness of the porous layer shows an increase of the wall temperature; the lowest performance was 17% lower than the bare surface. With the exception of the 2 mm surface, the enhancement ratio was lower than the medium and high mass flux at low mass flux. At medium mass flux, the enhancement ratio was 1.7, 1.6, and 1.4 times for the 0.2, 0.5, and 1 mm thickness of the porous layer, respectively. However, the highest porous layer thickness showed a reduction of 0.18 times in comparison with the bare surface. Finally, for the case of high mass flux, the wall superhat enhancement behavior was similar

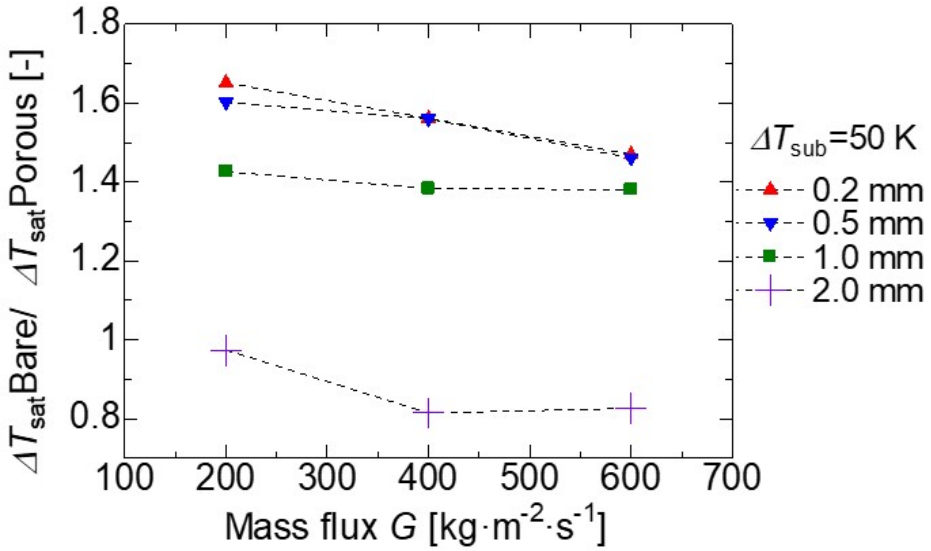

Figure 4.29: Ratio enhancement of the maximum ΔT_{sat} for the bare and the porous surface at medium inlet subcooling temperature.

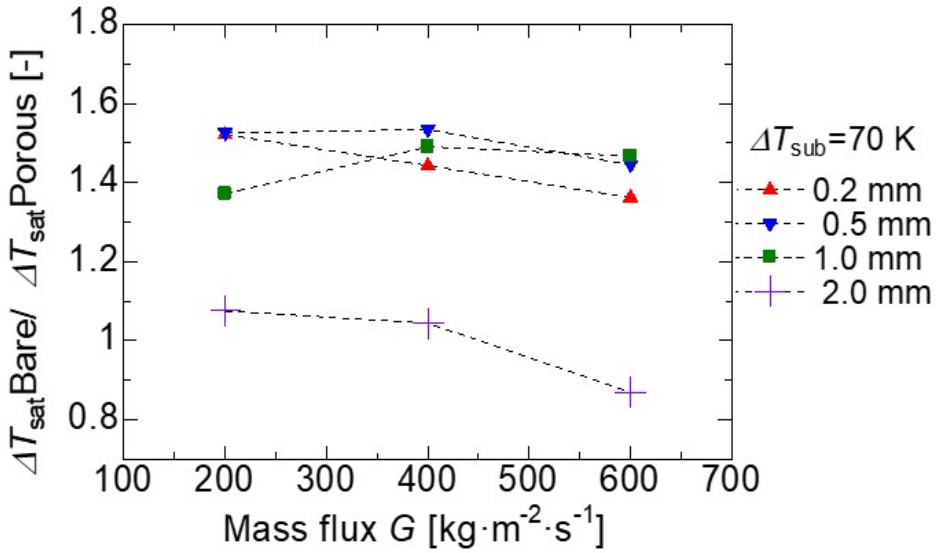

Figure 4.30: Ratio enhancement of the maximum ΔT_{sat} for the bare and the porous surface at high inlet subcooling temperature.

to the medium mass flux.

The subcooling degree plays a vital role in the wall superheat temperature. In Figure 4.29 is shown the wall superheat ratio of the different surfaces at medium subcooling inlet temperature. Here we can observe a small reduction on the wall superheat for the low thickness of the porous layer, in the other hand, an increment on the 1 mm and 2 mm thickness of the porous layer at low mass flux was found. At medium and high mass flux, the low thickness of the porous layer shows a similar ratio enhancement of around 60% and 50% respectively, higher than the surface. It can be concluded that at medium inlet subcooling temperature,

the enhancement increases at low mass flux. In the particular case of the 2 mm thickness of the porous layer surface, the ratio enhancement was again negative; this surface presented a reduction of around 0.2 times at high mass flux and almost a similar behavior at low mass flux.

The enhancement ratio at high inlet subcooling temperature is shown in Figure 4.30. One more time, the low thickness of the porous layer shows the best performance, where the 0.2 mm and 0.5 mm presented a reduction on the wall superheat of around 55% higher than the bare surface, slightly lower but also a temperature reduction was found for the 1 mm surface (around 38%). For the first time for all the parameters combinations, the 2 mm thickness of the porous layer presented a small enhancement of around 10% at low mass flux and high inlet subcooling temperature. At medium mass flux, the performance of the 2 mm surface was similar with respect to the low mass flux. However, for the case of low thickness of the porous layer and the 1 mm thickness of the porous layer, the enhancement ratio was between 45 and 58 %. At high mass flux and high subcooling inlet temperature, the enhancement of the porous thickness was similar for the three lowest porous thicknesses of around 0.45 times, higher than the 0 mm thickness of the porous layer. Nevertheless for the case of 2 mm thickness of the porous layer, an increment on the wall superheat temperature of around 0.15 times was found.

4.7.1 Wall temperature variation

In general terms and considering all the parameters combinations, the low thickness of the porous layer shows the best performance for the reduction of the wall superheat, the 1 mm thickness of the porous layer shows a relatively good performance. However, this surface promotes the critical heat flux at lower wall temperature degree. The 2 mm thickness of the porous surface promotes an increment in the wall temperature due to the saturation of vapor bubbles inside the porous body.

As mention in the section 2.3, the number of nucleation sites promotes the bubble vapor activity in the flow channel. However, the vigorous bubble activity can also increase the coalescence rate, and thus the pressure also increases. This vigorous activity promotes a vapor blanket on the surface that can be extended to the whole width of the channel, also

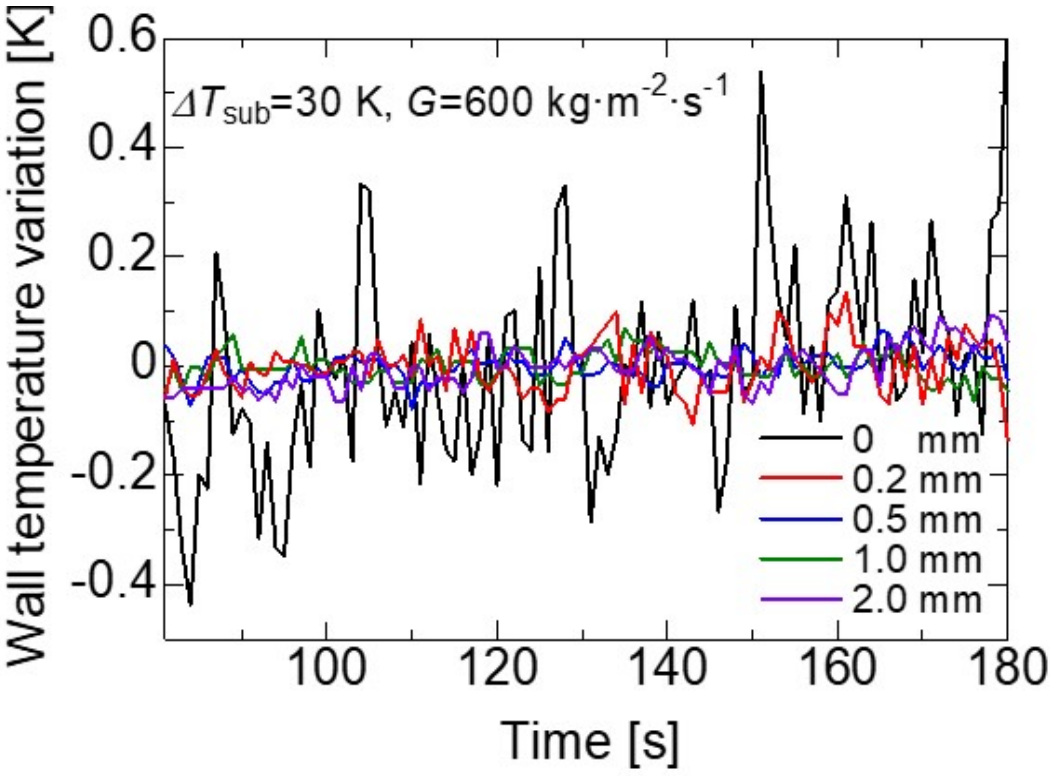

Figure 4.31: Wall superheat variation at high heat flux for all the thickness of the porous layer.

known as dryout point. The subcooled flow boiling condenses these vapor blankets, and the heating area is cooled. This heating and cooling activity generates a wall temperature variation that can cause damage to the cooling systems. This phenomenon is found at high heat flux, usually near to the CHF. In this subsection, the flow pattern at low inlet subcooling temperature and high mass fluxes are described. After analyzing the behavior of the low and high porous layer thickness, one surface of each group was selected (0.5, and 1 mm) arbitrarily to compare the surface cooling characteristics. The wall superheat variations are plotted in Figure 4.31. It was found that a more constant wall temperature on the porous thickness, this variation range is ± 0.1 K. On the other hand, the variations for the bare surface are considerably higher than for the porous surface; the variations are in the plotted range of ± 0.5 K. The slight variation in the wall temperature when the high-porosity sintered fibers surface is used was attributed to the constant water supply through the porous medium. Also the activation of a higher number of nucleation sites provides substitution of vapor bubbles and water near the heating surface. The data was recorded for three minutes during constant copper block B temperature.

The reduction of the wall superheat using the high-porosity sintered fibers is plotted

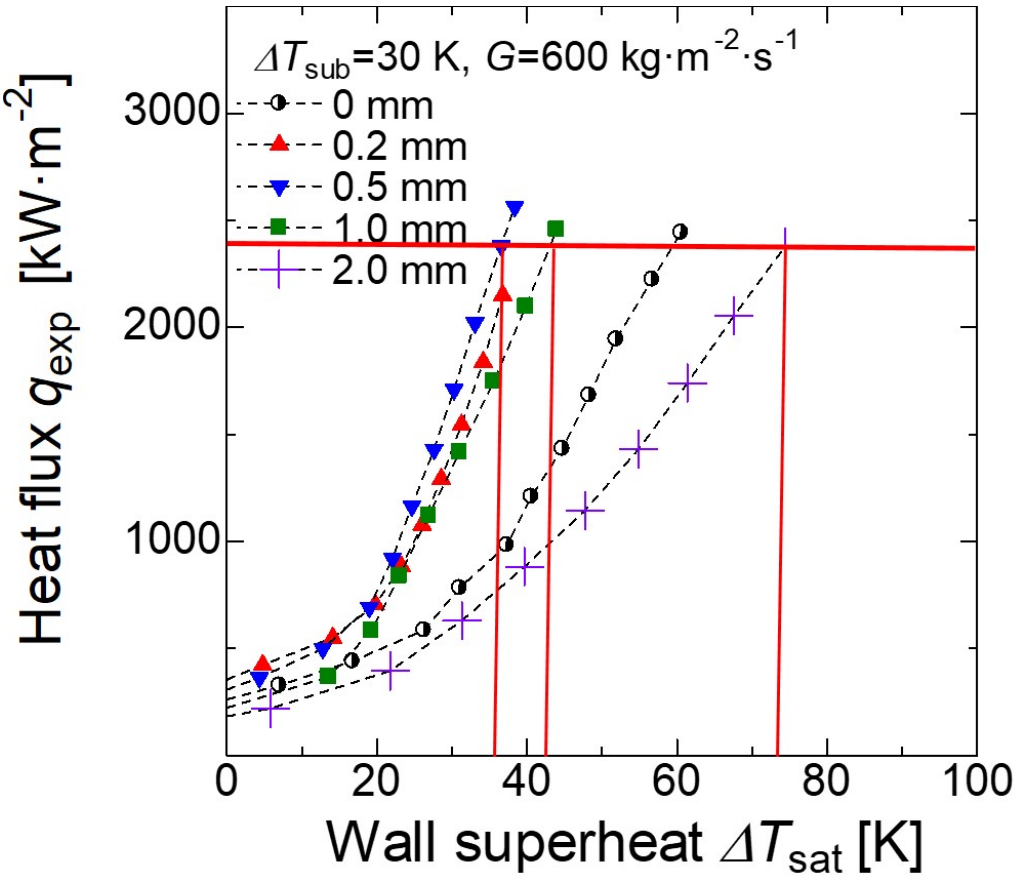

Figure 4.32: Comparison of the wall superheat at the same heat flux for all the thickness of the porous layer.

in Figure 4.32. A considerable reduction in the wall superheat temperature using the low thickness of the porous layer was confirmed. On the other hand, the high thickness of the porous layer presented an abrupt increment on the wall superheat. All the comparisons were made at a heat flux of around 2400 kW· m^{-2}.

Figure 4.33 shows the cycle of the vapor blanket generated on the 0mm thickness heating surface. The process starts with a thin vapor layer on the top of the surface (see Figure 4.33a). Then the small bubbles coalesce to a single big bubble that covers most of the surface; that effect produces the dryout followed by an abrupt increment of the wall temperature as shown in Figure 4.33b. The vapor blanket is condensed by the effect of the inlet subcooling temperature, producing a violent change in the pressure. Then the working fluid can flow and contact some parts of the heating surface, reducing again the wall superheat temperature. Then the cycle is restarted, and the variations on the wall temperature are constant during this part of the boiling process.

A relatively big bubble is generated on the low thickness of the porous layer. However, the

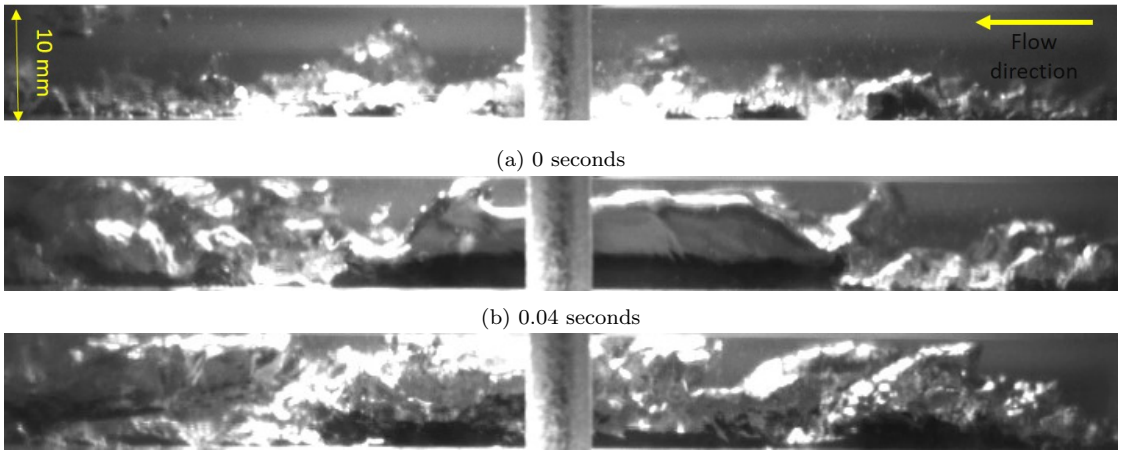

(a) 0 seconds

(b) 0.04 seconds

(c) 0.05 seconds

Figure 4.33: Flow bubble pattern on the bare surface at maximum heat flux 2400 kW· m^{-2}, $\Delta T_{sat} \approx 60$ K.

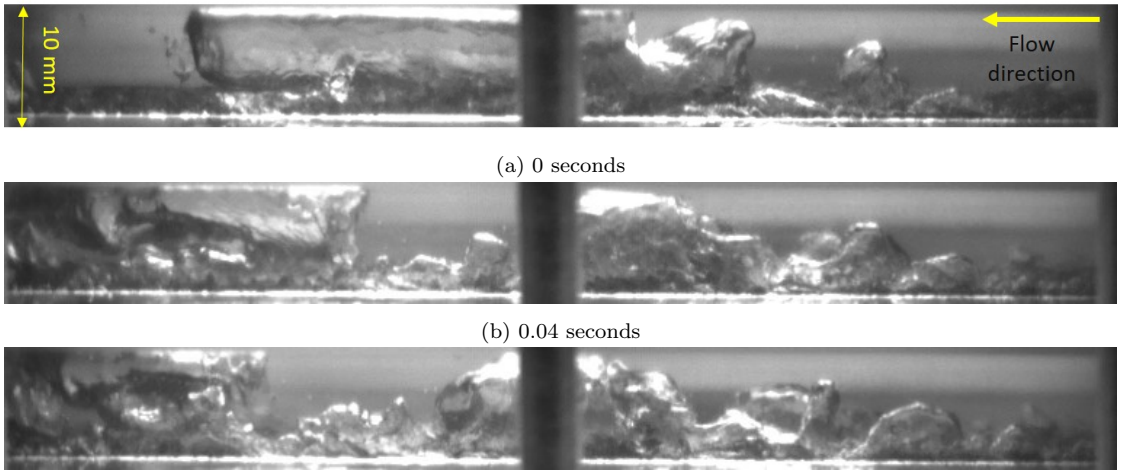

(a) 0 seconds

(b) 0.04 seconds

(c) 0.05 seconds

Figure 4.34: Flow bubble pattern on the 0.2 mm thickness of the porous layer at maximum heat flux 2400 kW· m^{-2}, $\Delta T_{sat} \approx 38$ K.

constant water supply through all the heating surfaces allows a rapid departure and bubble condensation. Figure 4.34 shows the bubble flow pattern on the 0.2 mm thickness of the porous layer.No dry-out occurs, unlike for the bare surface. Figures 4.34b and 4.34c show the condensation of the coalesced bubbles inside the flow channel.

The flow pattern using the low thickness of the porous layer is shown in Figure 4.35. Here, a constant water supply on the porous surface was observed, no vapor blanket was generated, unlike for the bare surface. Tiny bubbles escaped from the surface and coalescence at the outlet part of the flow channel as shown in Figure 4.35a. After 0.04 seconds, the bubbles coalesce to a big bubble and leave the porous surface, allowing the water supply to reach the heating surface. The coalesced bubble collapses slowly, and breaks into smaller bubbles. The

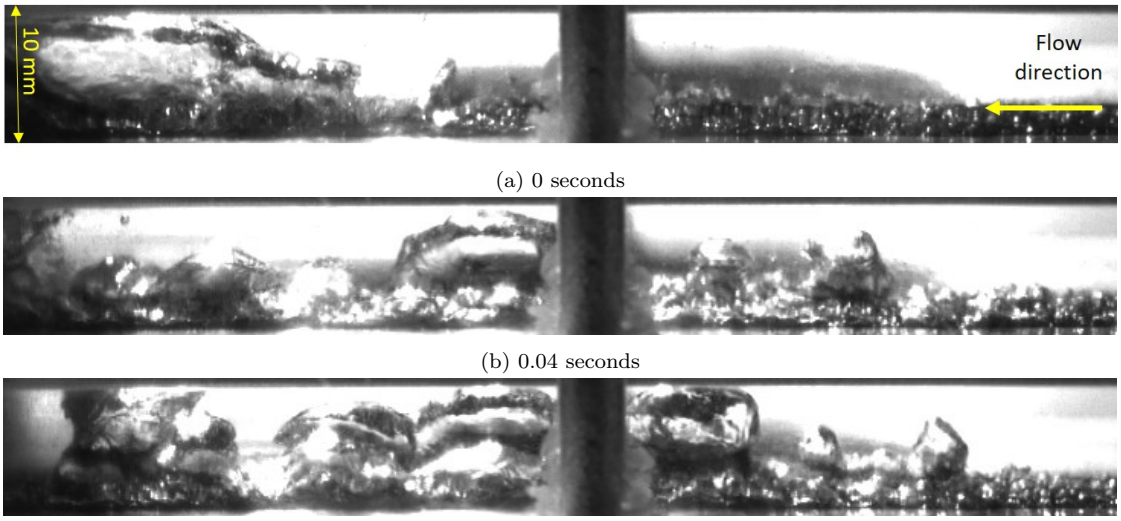

(a) 0 seconds

(b) 0.04 seconds

(c) 0.05 seconds

Figure 4.35: Flow bubble pattern on the 0.5 mm thickness of the porous layer at maximum heat flux 2500 kW· m^{-2}, $\Delta T_{sat} \approx 38$ K.

water flow is constant between the generated bubbles and the sintered fibers (Figure 4.35b).

The high wall superheat variation was also suppressed for the high thickness of the porous layer; this effect is attributed to the constant generation of small bubbles that coalesce outside the porous medium, and then are dragged by the water flow. A constant bubble generation and departure were recorded for the high thickness of the porous layer (see Figure 4.37). A constant water supply also was detected on the porous surface.

The high thickness of the porous layer surface also presents a similar bubble flow pattern. However, more small bubbles were recorded on top of the porous surface. The distribution of the small fibers promotes a continuous water flow through the heating surface area, and the flow turbulence above the porous medium promotes bubble formation and departure rate; thus, the porous medium keeps the heating surface at lower temperatures compared with the bare surface. The heating surface is higher for the porous surface than for the bare surface, and, due to this fact, the heat flux increases at the same wall temperature, and the film boiling presents a delay. The surface tension and the wickability keep the heating surface at lower temperatures for the porous surface. The effect mentioned above enhances the CHF in the porous surface. This had also been confirmed by Wang et al. [33]. They also reported that the CHF enhancement is directly related to supply water through the porous medium. On the bare surface, bubbles are generated, coalesce, and finally cover the heating area, thereby interrupting the water supply by promoting an abrupt increase in the wall temperature. On

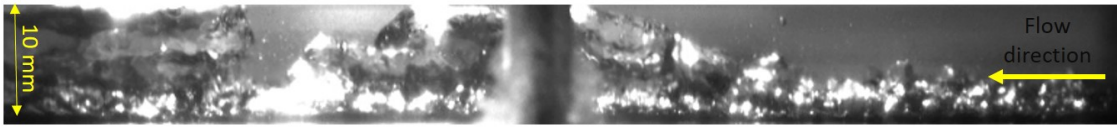

(a) 0 seconds

(b) 0.04 seconds

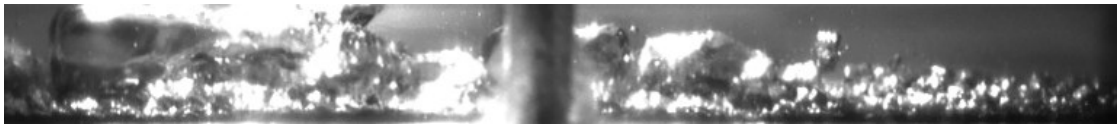

(c) 0.05 seconds

Figure 4.36: Flow bubble pattern on the 1 mm thickness of the porous layer at maximum heat flux 2500 kW· m^{-2}, $\Delta T_{sat} \approx 41$ K.

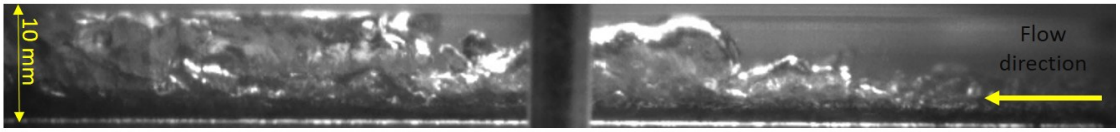

(a) 0 seconds

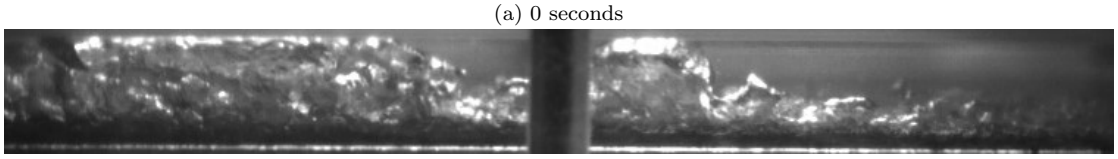

(b) 0.04 seconds

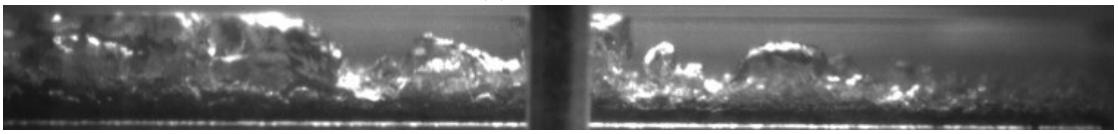

(c) 0.05 seconds

Figure 4.37: Flow bubble pattern on the 2 mm thickness of the porous layer at maximum heat flux 2500 kW· m^{-2}, $\Delta T_{sat} \approx 72$ K.

the other hand, in the case of the porous medium, the distribution of the small fibers promotes a continuous water flow through the heating surface area, and turbulence above the porous medium promotes the bubble formation and departure rate.

The influence of the high-porosity sintered fibers thickness directly influences the amount of heat flux, and the wall superheat temperature; also, and the onset nucleate boiling was shifted to lower wall superheat temperature using low porosity thickness. In general terms, the amount of heat flux was improved using the high-porosity sintered fibers at low thickness of the porous layer (0.2, and 0.5 mm).

5

Results from computational fluid simulation

The current chapter provides the results from the computational fluid dynamics (CFD) analysis. Due to the difficulties that boiling flow phenomena present for simulation analysis we decide to perform the simulation of the high-porosity sintered fibers heat transfer performance on the single-phase regime. The simulation results are compared based on the studies and results published by Watanabe et al. [89] who belong to the same research group. They reported an enhancement on the heat transfer coefficient by about a factor of seven and a heat exchange about five times higher when the high-porosity sintered fibers body was inserted on the heating pipe using air as working fluid. In addition, they found insignificant change in the results when a different tube diameter was used. For the CFD analysis, the novel software STREAM Version 2021 developed by HEXAGON and MSC software will be used [90] which perform the simulation using the Voxel method as the meshing method and the Finite Element Method (FEM) for the computational fluid dynamics analysis.

5.1 Previous considerations for the simulation

As mentioned above, the computational simulation for two-phase flow using high-porosity sintered fibers attached to the surface is extremely difficult to perform; the number of parameters and considerations that involve the boiling phenomena make the prediction of heat fluxes and the flow pattern highly complex, actually, a general computational subcooled flow boiling method to predict the heat transfer coefficient used in engineering applications does not yet exist and this fact is a limitation on the CFD. Due to the lack of appropriate models to predict the heat flux, some researchers proposed some previous considerations before the CFD such as the reduction of relevant phenomena on the simulation, the analysis on

the single-phase range to avoid the phase-change consideration, the analysis in 2-D instead complex 3-D models, the use of scale channels instead of the robustness for geometrically complex systems, etc. In conclusion, the main problem is that the empirical models given by the CFD analysis offer only a relative close value on the boiling heat flux in relation to the wall superheat temperature. [91–93]. Besides the limitations on the computational fluid dynamics, the simulation method needs an expensive computational time, in addition to a high spatial and temporal resolution.

The CFD simulation software provides information that helps to understand the boiling phenomena. However, they are so far to predict the real thermal and physic characteristics of the subcooled flow boiling. In conclusion, the CFD simulation results need to be confirmed by the experimental results. For this reason,the computational analysis on this research will be performed with air as a working fluid on the single-phase regime. The results will be compared with the experimental results obtained by Watanabe et al. [89], where the inlet and outlet temperature analysis will also be done under the single-phase consideration. The model technique used in this research was the VOXEL method; this model was selected due to the high accuracy on the creation of CAD models. Nevertheless, it usually needs to be combined with a previous 3D scan to create the models. Due to the complex geometry of the high-porosity sintered fibers body, the 3D model was created by a previous CT scan to form the porous body with the Vortex simulation model. The simulation was performed using a computer equipped with a ram memory DDR4 3000 MHz (p.c) with a graphic card NVIDIA RTX A400 (PCI-express Gen) and an Intel processor core i9-11900K 5.0 GHz (o.c).

5.1.1 Voxel method

As mention in section 3.5.2, the complex geometry inside the porous body makes difficult the modeling in 3D software's, due to this fact the voxel method was selected to create the 3D model of the high-porosity sintered fiber.

The mesh created by the common modeling mesh methods are created by a matrix of small squares on the surface of the model as shown in Figure 5.1. This method is used by many software's in the computational fluid simulation and in fact offer a relative good accuracy. Nevertheless, this meshing method is usually used when the 3D model geometry is not complex. A high complexity geometry or a simulation of a group of bodies assembled

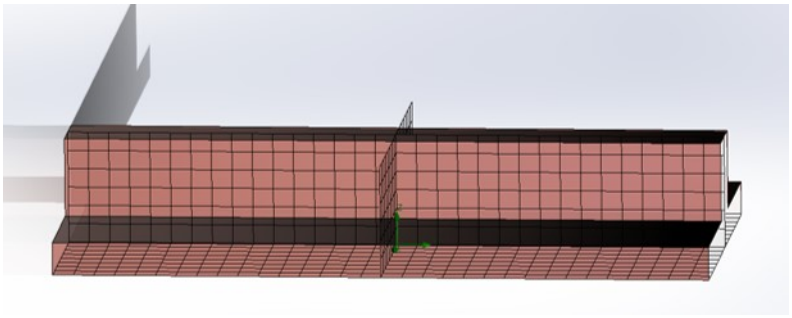

Figure 5.1: Common meshing 2D method on the Computational fluid dynamics.

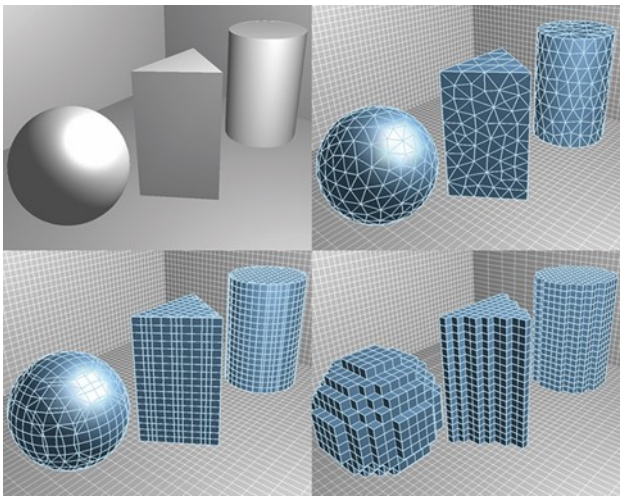

Figure 5.2: Voxel meshing method; creation of small finite cuboids [90].

tends to reduce the accuracy of the results and also increase the computational time of the analysis.

In the other hand, the Voxel meshing method is created by a division of the body in small finite cuboids, thus the distribution of the small cuboids made a grid that is used as a mesh, actually, Voxel method is usually called the “mesh-less method“.

The software STREAM also can create the partition of the 3D model in Cartesian or Polar coordinates allowing a high accuracy of the representation of the model on the simulation as shown in Figure 5.2.In addition, when the Voxel is used, the mesh can be overlapped on the model. STREAM software performs the simulation using the Finite Element Method.

5.1.2 Related studies to the high-porosity sintered fibers

High-porosity sintered fibers used as a passive method to enhance the heat flux was also studied by Watanabe et al. [89] (who also belong to the same research group of the author). They performed and experimental research to evaluate the heat transfer enhancement of the

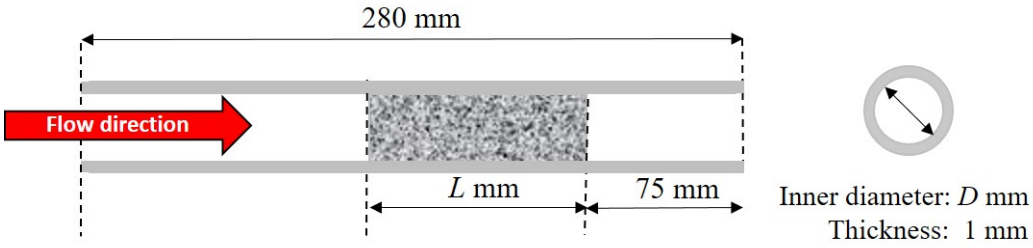

(a) Porous material location inside the pipe

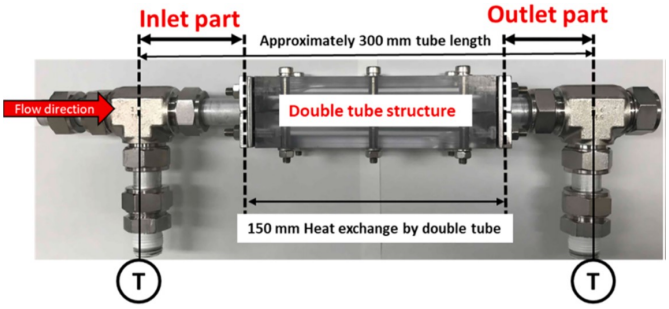

(b) Double tube exchanger photography

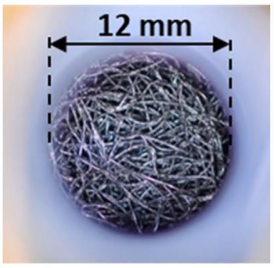

(c) High sintered fiber inserted on the pipe

Figure 5.3: Experimental pipe filled with the high-porosity sintered fibers used by Watanabe et al. [89].

the high-porosity sintered fibers inserted on a pipe. They use the high-porosity sintered fibers as the described in section 3.5.2, nevertheless selected material to machined the sintered fibers was aluminum. They use air as working fluid with an inlet temperature of 200 °C flowing through the pipe of 280 mm length and different diameters. The tube thickness was the same for all the porous pipes. They also tested different porous lengths inside the tubes. Outside the pipe isobutane with a temperature of 2 °C flown around the hot pipe on a double tube structure as shown in Figure 5.3a and 5.3b. The high-porosity sintered fibers body was made of aluminum intricately intertwined with a porosity of 80%, in order to reduce the thermal resistance, the pipe material also was aluminum, and the porous medium was sintered inside the pipe at 75 mm to the outside part of the tube. We performed a computer tomography scan to create a 3D model of the high-porosity sintered fibers.

5.2 Test section modeling

After performing the computational tomography, a 3D model of the pipe filled with high-porosity sintered fibers was designed and simulated on the computational fluid dynamics software "STREAM." The circular tube is shown in Figure 5.4a. The parameters are those

Table 5.1: Parameters and considerations for the simulation analysis.

Air density at 200 °C	$kg \cdot$ m^{-3}	0.73
Mass rate	$\dot{m}$ [g·s^{-1}]	0.5, 1.0, 1.4
Inlet temperature	T_{in} [°C]	200
Pipe outside temperature	T_{in} [°C]	2
Inner diameter	d_{in} [mm]	20.6
Outer diameter	d_{out} [mm]	18.5
Porous lenght	l [mm]	25.43

for an aluminum pipe filled with high-porosity sintered fibers also made of aluminum. This choice of using the same material parameters for the wall and the porous medium should significantly reduces the thermal resistance. The heat transfer tube filled with porous material improves the heat transfer due to the increase of the contact area with the fluid, at the same time reducing the thermal resistance.

The conditions of the pipe crated for the simulation are shown in Figure 5.4a and 5.4b. The inlet part of the test section is assigned a mass rate of 0.5, 1.0, and 1.4 g·s^{-1} at an inlet temperature of 200 °C. The average velocity of the working fluid is 1.5, 3.11, and 4.35 m $\cdot$ s $^{-1}$. The pressure boundary condition at the outlet part of the porous pipe was fixed to 0.0 Pa. The surrounding temperature (outside the pipe) was set to 2°C to simulate the isobutane flowing outside the pipe and confirm the results obtained by Watanabe et al. [89].

The 3D modeling of the porous pipe test section consists of a tube with an inlet diameter of 18.5 mm and an outlet diameter of 20.6 mm. The porous pipe is completely filled with the porous aluminum material; the porosity of the porous material is 80%, represented by the green part inside the pipe. The total height of the porous pipe is 25.43 mm. Detailed information of the modeling parameters and conditions are shown in Table 5.1.

5.3 Simulation results

The results obtained by the simulation are presented in this section. The mass rate was considered as a parameter and compared with the experimental results obtained by Watanabe et al. [89]. Three different mass rates were tested, the simulation was set to 1000 computational iterations for steady-state analysis which takes a total computational time of around 36 hours using the equipment described in section 5.1.

The results of the inlet and outlet temperature obtained for the simulation are shown in

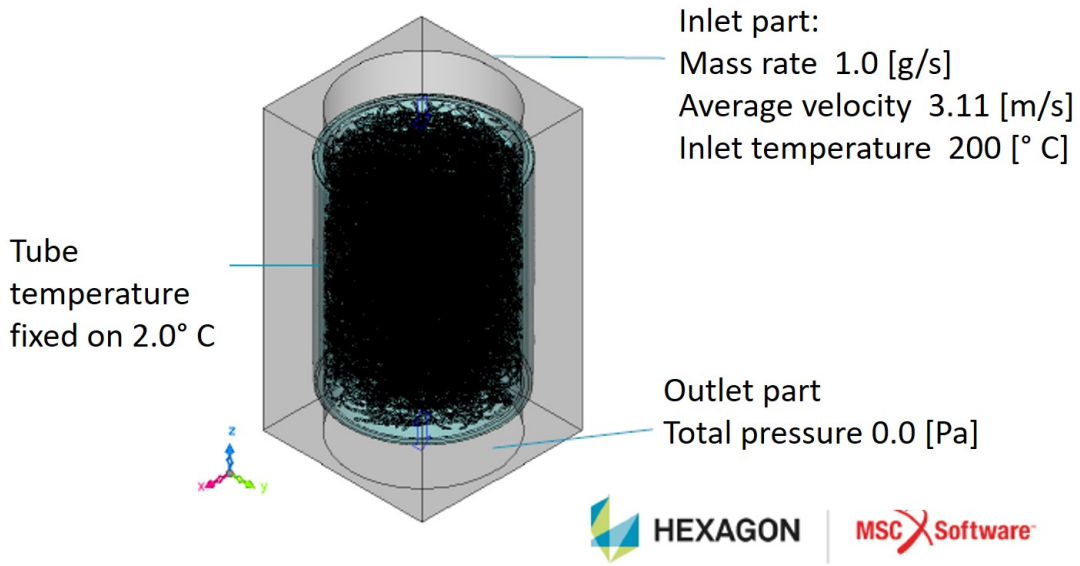

(a) Experiment conditions

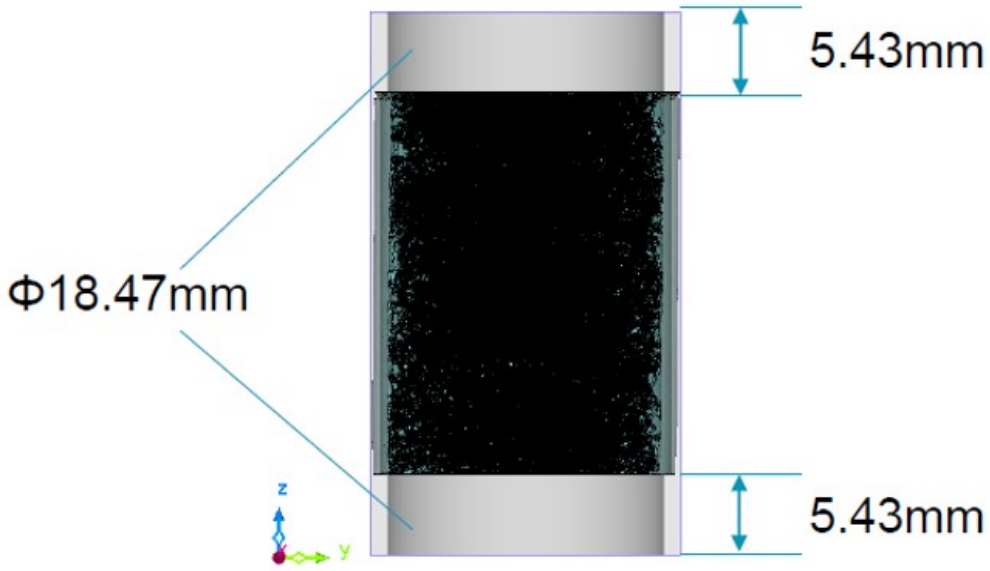

(b) Porous tube dimensions

Figure 5.4: Porous pipe dimensions and conditions for the computational analysis.

Figure 5.5a. A high reduction of the inlet temperature was found in the simulation. The inlet temperature of the fluid was reduced was reduced by about 196.2° C in comparison with the outlet temperature at low mass rate (0.5 g·s^{-1}). The low mass flow rate allows the outlet temperature to exchange a high amount of heat due to the small temperature and velocity profile. It was also confirmed that the temperature was drastically reduced in the inlet part of the tube over the first millimeters of the porous materials.

For the mass flow rate of 1.0 g·s^{-1}, the outlet temperature suffered an increased in com-

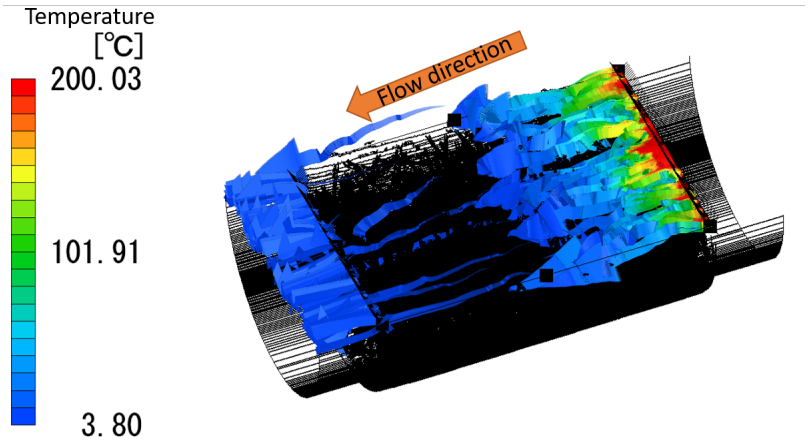

(a) Inlet and outlet temperature at 0.5 g·s^{-1}

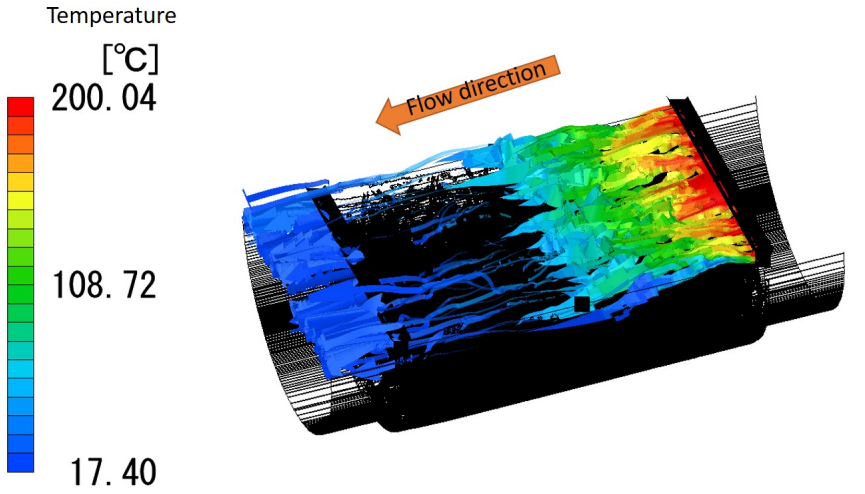

(b) Inlet and outlet temperature at 1.0 g·s^{-1}

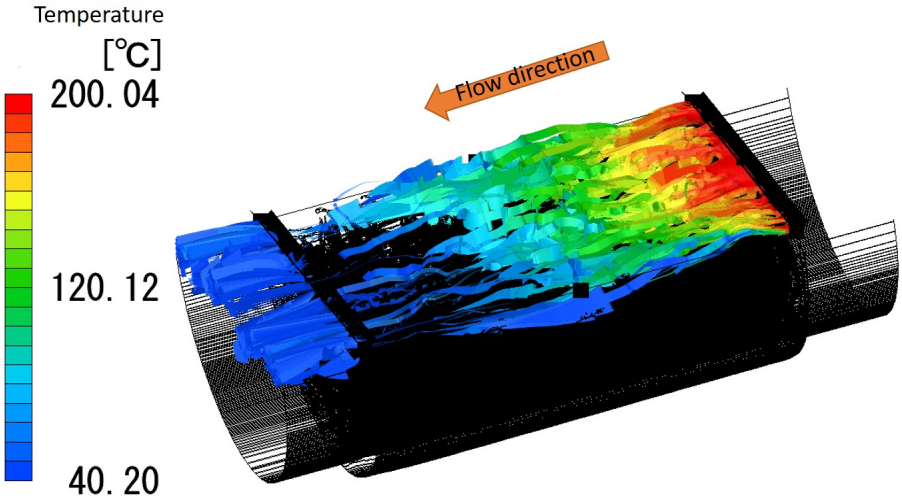

(c) Inlet and outlet temperature at 1.4 g·s^{-1}

Figure 5.5: High-porosity sintered fibers heat flux results from the simulation.

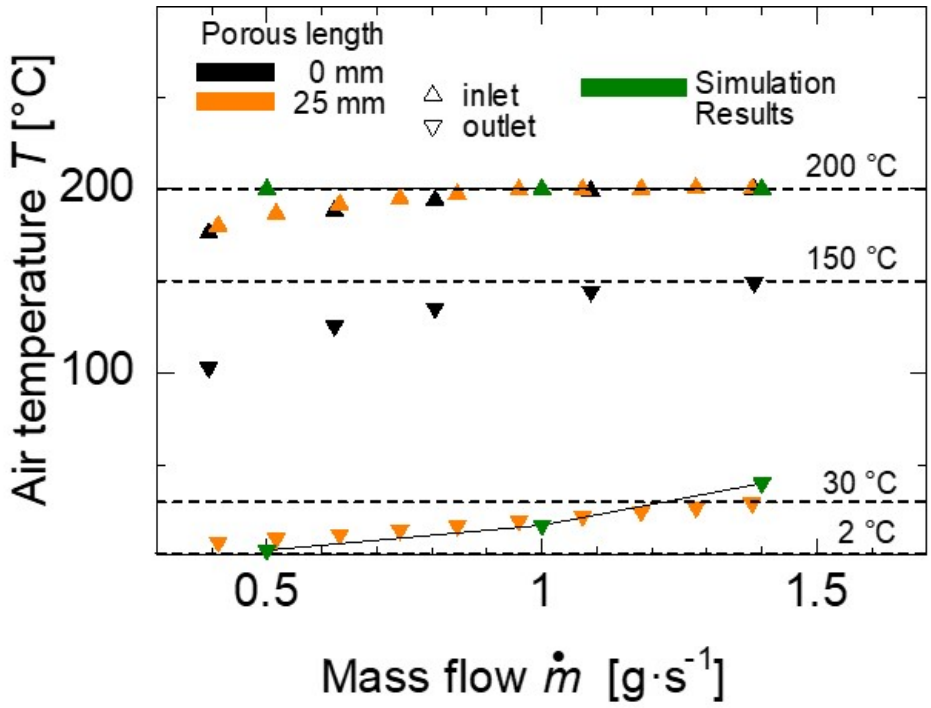

Figure 5.6: Comparison of the experimental results obtained by Watanabe et al. [89] and the present simulation results.

parison with the 0.5 g·s^{-1} case. This can be attributed to the increase in the velocity and temperature profile. However, the reduction of the temperature and heat exchange from the hot air to the outside part of the pipe was considerably high. A reduction of 182.6 °C was found as shown in Figure 5.5b.

Finally, the results of the cooling enhancement at a mass flow rate of 1.4 g·s^{-1} showed a higher outlet temperature than the 1.0 and 0.5 g·s^{-1} (see Figure 5.5c), once again, the low temperature reduction is due to the high velocity and temperature profile. The temperature was reduced to 160 °C, and this was the lower heat exchange found in the three cases.

The results of the heat transfer performance were compared with the results obtained in [89]. The results are shown in Figure 5.6; they tested four different porous lengths, including the non-filled porous pipe (0 mm). They found a similar behavior on all the porous lengths. A reduction of around 198 ° C for the best case was found on the 75 mm porous length. On the other hand, the 0 mm porous length temperature was reduced to around 100 ° C and changed according to the mass rate, increasing the outlet temperature of 150 ° C at the highest mass rate.

The CFD simulation results show a good agreement with the experimental results. The specific case of the 25 mm length presented the best agreement with the simulation results.

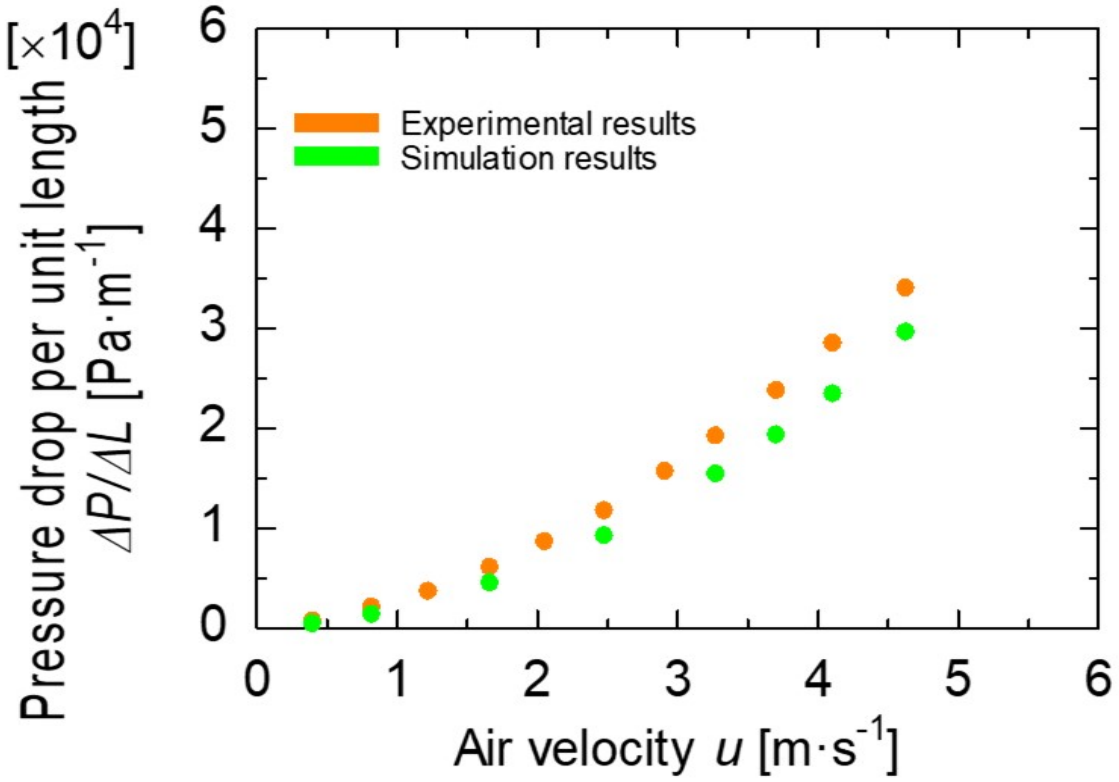

Figure 5.7: Pressure drop of the simulation and experimental results.

At a mass inlet rate of 0.5 g·s^{-1} the outlet temperature calculated by the CFD was around 3.8 ° and the experimental results show an outlet temperature of 3 °. In the case of 1.0 g·s^{-1}, the outlet temperature also presented an excellent agreement with the experimental results. The temperature was reduced to around 180 °. At a high mass rate (1.4 g·s^{-1}), the temperature was slightly higher on the simulation analysis. Nevertheless, the excellent agreement between the simulation and the experimental results were confirmed.

In order to confirm the accuracy of the heat flux simulation, also the pressure drop per unit length was calculated and is shown in Figure 5.7. It was found a high accuracy between the experimental and the simulation results. In the particular case of the low air velocity (lower than 2.5 m·s^{-1}) the results show the best agreement, however, as the air velocity increases, the accuracy of the simulation is lower. This slight difference is attributed to the number of cycles on the simulation, however, for practical cases the slight difference can be neglected.

6

Conclusions and Future Work

This chapter is devoted to a summary of the current work with the main findings and conclusions. The influence of the high-porosity sintered fibers attached to the heating surface and the parameters that involve any change in the heat flux are described in this section. Firstly a brief summary and the main conclusion are described in the section 6.1.

6.1 Summary and main conclusion

The high heat flux that numerous thermal engineering systems need to dissipate is the most crucial factor that engineers need to consider. Researchers have focused on the use of passive methods to develop high-performance cooling systems. New passive and actives technologies have been developed to increase the heat transfer performance. However,because active technologies need additional energy, more attention and effort goes into developing passive methods that do not require extra energy consumption. Recently, heating surface modifications have gained much attention from several researchers, particularly the use of porous materials.

The high-porosity sintered fibers attached to the surface was used as a passive method to increase the heat flux in some cooling systems. In this research, a high-porosity sintered fibers made by copper with a porosity of 86% was attached to the surface, four different thickness of the porous layer were tested and compared with the bare surface (0 mm thickness of the porous layer). Deionized water was selected as a working fluid to reduce the effects of the oxidation, also to warranty the absence of micro bubbles on the water, a degassing process was performed. The influence of the mass flux and the inlet subcooling temperature were also considered; both parameters were tested at a low and high level. In general terms, the following conclusion was obtained.

- The use of the high-porosity sintered fibers attached on the surface, in the particular

case of low porous layer thickness (0.2 and 0.5 mm) can increase the amount of heat flux considerably at the same wall superheat by a factor of 2.5 in comparison with the bare heating surface. Also, at the same heat flux, the abrupt increment of the wall temperature degree was avoided, and a reduction of up to 70% was found. Nevertheless, the high-porosity layer thickness (1 and 2 mm) presented a reduction on the heat flux enhancement and a increase on the wall superheat in comparisson with the bare surface. The vapor trap ability plays an essential role in the water supply, when a vapor blanket is formed and trapped inside the porous body, the contact bweteen the water and the heating surface is reduced; as a result, the heat transfer coefficient suffers a reduction. Due to the previously mentioned effects, the porous thickness needs to be considered in this passive cooling system technology design.

- The results from the CFD shown a good correspondence to the experimental results for the regime of single-phase flow. A considerable reduction in the fluid temperature at the inlet and outlet was found. As a result, an increase of the heat transfer coefficient by around a factor of seven could be confirmed with the simulation analysis. The pressure drop per unit length inside the porous medium was considerably higher than the bare surface and changed according to the mass rate.

The details of the enhancement on the heat flux and the considerable reduction of the wall superheat temperature are described in the following subsections.

6.1.1 Conclusions for the mass flux effect

Three different regimes for the mass flux were used as parameters (laminar, transition, and turbulent flow). The Reynolds number directly affects the heat flux performance, and in particular, the CHF is shifted to a higher heat flux. A summary of the finding is listed below.

- Independent of the inlet subcooling degree, at higher mass flux the ONB was shifted to a higher wall superheat temperature.
- The CHF was found at higher wall temperature in the high thickness of the porous layer at low mass flux.
- At higher mass flux, the production of bubbles is higher on the high-porosity sintered fibers, also aftee the NVG the wall temperature was reduced.

- In the single-phase regime, the mass flux affects the heat flux considerably when the porous material is used as the heating surface. In particular, the low thickness of the porous layer (0.2 and 0.5 mm) presented an enhancement on the heat flux due to the bubble generation rate; nevertheless, the high thickness of the porous layer showed a negative effect on the heat transfer performance due to the formation of a vapor blanket inside the porous body.

- The wall superheat temperature at the critical heat flux was found at lower heat flux and at higher mass flux. The abrupt increase on the wall superheat was not found on the high porous layer thickness due to the fact that the high mass flow velocity promotes a higher drag force on the bubble flow pattern, thus the bubbles are constantly removed from the surface.

The effect of the mass flux was study in the laminar, transition and turbulent flow. It was possible to compare the effect of mass flux on the heat transfer performance using different porous layer thickness. Nevertheless, it is necessary is further studies to consider mass fluxes at higher Reynolds numbers.

6.1.2 Conclusions for the inlet subcooling temperature effect

Similar to the mass flux parameter, the inlet subcooling temperature was tested under three different temperatures (low, medium, and high ΔT_{sub}). After the data analysis, the conclusions are listed below.

- In the single-phase regimen and independent of the mass flux, at higher inlet subcooling temperatures, higher heat flux was detected on the low thickness of the porous layer surfaces (0.2 and 0.5 mm). On the other hand, lower heat flux was measured at high thickness of the porous layer.

- In the two phases regime, at higher inlet subcooling temperature, the critical heat flux was reached when the high thickness of the porous layer (1.0 and 2.0 mm) surface was used. Abrupt increments on the wall superheat were detected at high inlet subcooling temperatures.

- Bubble formation and departure rate were clearly higher at low inlet subcooling temperature; the thickness of the porous layer surface also promotes the bubble formation

at a lower inlet subcooling degree. The condensation on the flow channels is faster at a high inlet subcooling degree.

6.1.3 Conclusions for the porous thickness surface effect

It is necessary to consider the thickness of the porous layer on the design of the surface modifications for cooling systems. Independent to the mass flux and the inlet subcooling temperature effect, the thickness of the porous layer plays the most crucial role in the heat flux enhancement. A similar behavior on the heat flux enhancement was detected in the single-phase and the two-phase on the high-porosity sintered fibers attached to the surface. The 0.5 mm thickness of the porous layer shown the best high cooling performance, followed by the 0.2 mm thickness of the porous layer. For these two porous layer surfaces no abrupt increment on the wall superheat temperature occurred, at the same time and enhancement on the heat flux was found. Slightly lower heat flux enhancement was found when the 1.0 mm thickness of the porous layer was attached to the surface. Nevertheless, a lower heat flux for a high subcooling temperature of the inlet was measured. Also, the CHF was easily reached when the 2 mm thickness of the porous layer was tested.

Unlike the characteristics described above, the 2.0 mm thickness of the porous layer showed the opposite effect. The CHF was easily reached was well as considerably higher wall temperature. This can be attributed to the ability to trap vapor and the lower water supply ability. In general terms, the use of porous materials attached to the surface reduces the wall temperature variations; as result, the pressure inside the channel flow also was reduced.

6.2 Future work

To continue the improvement of high-porosity sintered fibers as a passive method, future work needs to be conducted both for the experimental method as well as the CFD analysis.

In the particular case of the experimental research, is necessary to test different porosities, thickness of the porous layer, and porous materials. Also new flow channel geometries and mass rates must be consider in order to create a prediction method for the subcooled flow boiling heat flux and the critical heat flux.

To extend the applications of the passive cooling methods, the author also recommends

to perform an experimental analysis of the pool boiling to reach the CHF easily and flow boiling under considerably higher mass fluxes and saturation temperature. Consequently, the operating ranges and the number of cooling systems can be potentially increased.

As mention in section 5, although the difficulties that the two-phase boiling heat transfer simulation represents, the computational fluid dynamics simulation needs to be conducted according to the following steps.

1. Use water under different mass fluxes as working fluid on the CFD simulation using the software stream.

2. Simulate subcooled flow boiling simulation in the pipe filled with the high-porosity sintered fibers to confirm the repeatable enhancement on the heat transfer performance.

3. Simulate different geometries of the flow channel, porous thickness, and material to confirm the results described in section 4.

4. Analyze the bubble formation and departure using the CFD STREAM software.

5. Modeling and simulation of subcooled flow boiling heat transfer performance using high-porosity sintered fibers attached to the surface in the two-phase flow regime.

References

[1] G. Zhu, Q. Bi, J. Yan, T. Wang, J. Zhao. "Heat transfer characteristics of subcooled water in a hypervapotron under high mass fluxes and high heat fluxes", *International Journal of Heat and Mass Transfer,* vol. 129 pp. 580-590, October 2018.

[2] S. Rashidi, J.A Esfahani, A. Rashidi. "A review on the applications of porous materials in solar energy systems", *Renewable and Sustainable Energy Reviews,* vol. 73 pp. 1198-1210, February 2017.

[3] M. Dehghan, M.S Valipour, S. Saedodin. "Microchannels enhanced by porous materials: Heat transfer enhancement or pressure drop increment?", *Energy Conversion and Management,* vol. 110 pp. 22-32, 2016.

[4] B.J. Jones, S.V Garimella. "Surface roughness effects on flow boiling microchannels", *Journal of Thermal Science and Engineering Applications,* vol. 1 041007/1-9 December 2009.

[5] A. Lucic, M. Emans, F. Mayinger, C. Zenger. "Interferometric and numerical study of the temperature field in the boundary layer and heat transfer in subcooled flow boiling", *International Journal of Heat and Fluid Flow,* vol. 25 pp. 180-195, 2004.

4444

[6] Y. Yang, X. Ji, J. Xu. "Pool boiling heat transfer on copper foam covers with water as working fluid", *International Journal of Thermal Sciences,* vol. 49 pp. 1227-1237, February 2010.

[7] M. Shojaeian, A. Kosar. "Pool boiling and flow boiling on micro- and nanostructured surfaces", *Experimental Thermal and Fluid Science,* vol. 63 pp. 45-73, January 2015.

[8] C.Y. Zhao. “Review on thermal transport in high porosity cellular metal foams with open cells”, *International Journal of Heat and Fluid Flow,* vol. 55 pp. 3618-3632, April 2012.

[9] J. Qin, Q. Chen, C. Yang, Y. Huang. “Research process on property and application of metal porous materials”, *Journal of Alloys and Compounds,* vol. 654 pp. 39-44, 2016.

[10] S. Mori, K. Okuyama. “Enhancement of the critical heat flux in saturated pool boiling using honeycomb porous media”, *International Journal of Multiphase Flow,* vol. 35 pp. 946-951, 2009.

[11] G.S. Hwang, M.Kaviany. “Critical heat flux in thin, uniform particle coatings”, *International Journal of Heat and Mass Transfer,* vol. 49 pp. 844-849, 2006.

[12] G.S. Day, H.F. Drake, H. Zhou, M.R. Ryder “Evolution of porous materials from ancient remedies to modern frameworks”, *Communications Chemistry,* vol. 4 114, 2021.

[13] D. Cooke, S.G Kandlikar. “ Effect of open microchannel geometry on pool boiling enhancement,” *International Journal of Heat and Mass Transfer,* vol. 55 pp. 1004-1013, 2012.

[14] S.G. Liter, M.Kaviany. “Pool-boiling CHF enhancement by modulated porous-layer coating: theory and experiment”, *International Journal of Heat and Mass Transfer,* vol. 44 pp. 4287-4311, January 2001.

[15] W. Nakayama, H. Daikoku, H. Kuwahara, K. Kakizaki, M.H Kim, H.S. Park. “High-performance heat transfer surface THERMOEXCEL”, *Hitachi Review ,* vol. 24 No. 8 1975.

[16] S.H Kim, G.C. Lee, J.Y. Kang, K. Moriyama, M.H Kim, H.S. Park. “Boiling heat transfer and critical heat flux evaluation of the pool boiling on micro structured surface”, *International Journal of Heat and Mass Transfer,* vol. 91 pp. 1140-1147 September 2015.

[17] M.S. Sarwar, Y.H. Jeong, S.H Chang. “ Subcooled flow boiling CHF enhancement with porous surface coatings”, *International Journal of Heat and Mass Transfer,* vol. 50 pp. 3649-3657, 2007 .

[18] S.G Kandlikar, J.N Chung. “Multiphase flow handbook”, *Taylor and francis group,* Chapter 3, boiling and condensation, 2006 .

[19] C.M. Kruse, T. Anderson, C. Wilson, C.Zuhlke, D. Alexander, G. Gogos, S. Ndao. "Enhanced pool-boiling heat transfer and critical heat flux on femtosecond laser processed stainless steel surfaces", *International Journal of Heat and Mass Transfer,* vol. 82 pp. 109-116, 2015.

[20] L. Lin, M.A. Kedzierski. "Review of low-GWP refrigerant pool boiling heat transfer on enhanced surfaces", *International Journal of Heat and Mass Transfer,* vol. 131, pp. 1279-1303, November 2018.

[21] Theodore L.Bergman. *Fundaments of Heat and Mass Transfer,* 7th edition John Wiley Sons. USA 2011.

[22] Y. Cengel. *Heat and Mass Transfer,* 3rd edition Mc Graw Hill. USA 2007.

[23] S. Nukiyama. "The maximun and minimum values od the heat Q transmitted from metal to boiling water under atmospheric pressure", *Journal Japan Soc. Mech. Engrs,* vol. 9, pp. 367-374, 1934.

[24] S. G Kandlikar. "Heat transfer characteristics in partial boiling, fully developed boiling, and significant void flow regions on subcooled flow boiling", *Journal of Heat Transfer,* vol. 120, pp. 395-401, May 1998.

[25] X. Chen, X. Xia, C. Sun, X. Yan. "Transient thermal analysis of the coupled radiative and convective heat transfer in a porous filled tube exchanger at high temperatures", *International Journal of Heat and Mass Transfer,* vol. 108, pp. 2472-2480, February 2017.

[26] M. Jakob. "Heat transfer in evaporation and condensation-I", *Mech. Eng. Am. Soc. Mech. Eng,* vol. 58, pp. 643–660, 1936.

[27] G. Wang, P. Cheng. "Subcooled flow boiling and microbubble emission boiling phenomena in a partially heated microchannel", *International Journal of Heat and Mass Transfer,* vol. 52, pp. 79-91, January 2009.

[28] H. Steiner, A. Kobor, L. Gebhard. "A wall heat transfer model for subcooled boiling flow", *International Journal of Heat and Mass Transfer,* vol. 48, pp. 4161-4173, February 2005.

[29] X. Fang, Y. Yuan, A. Xu, L. Tian, Q. Wu. "Review of correlations for subcooled flow boiling heat transfer and assessment of their applicability to water", *Fusion Engineering and Design,* vol. 122, pp. 52-63, September 2017.

[30] X. Fang, C. Chen, Q. Wu, L. Tian. "A method for developing correlations for subcooled flow boiling heat transfer and its application to water", *Fusion Engineering and Design,* vol. 129, pp. 286-290, February 2018.

[31] Shoukat A. Khan , Muataz A. Atieh, Muammer Koç. "Micro-Nano Scale Surface Coating for Nucleate Boiling Heat Transfer: A Critical Review", *Energies,* vol. 11, 3189, November 2018.

[32] Manglick, R.M. *Heat transfer Enhancement. In Heat Transfer Handbook,* Bejan, A., Kraus, A.D., Eds.; John Wiley and Sons, Inc.: Hoboken, NJ, USA, 2003; pp. 1029–1130. ISBN 0-471-39015-1.

[33] L.Wang, A.R. Khan, N. Erkan, H. Gong, K. Okamoto. "Critical heat flux enhancement on a downward face using porous honeycomb plate in saturated flow boiling", *International Journal of Heat and Mass Transfer,* vol. 109, pp. 454-461, February 2017.

[34] T. Inoue, N. Kawae, M. Monde. "Effect of subcooling on critical heat flux during pool boiling on a horizontal heated wire", *International Journal of Heat and Mass Transfer,* vol. 33, pp. 481-488, April 1998.

[35] B. Liu, J. Liu, J. Zhou, B. Yuan, Y Zhang, J. Weia, W. Wang. "Experimental study of subcooled boiling pool heat transfer and its "hook back" phenomenon on micro/nanostructured surfaces", *International Communications in Heat and Mass Transfer,* vol. 100, pp. 73-82, February 2019.

[36] Y. Otomo, E. Santiago Galicia, K. Enoki. "Enhancement of Subcooled Flow Boiling Heat Transfer with High Porosity Sintered Fiber Metal", *Applied Sciences,* vol. 11, 1237, January 2021.

[37] E. Santiago Galicia, Y. Otomo, T. Saiwai, K. Takita, K. Orito, K. Enoki. "Subcooled Flow Boiling Heat Flux Enhancement Using High Porosity Sintered Fiber", *Applied Sciences,* vol. 11, 5883, June 2021.

[38] M.C. Paz , M. Conde, E. Suárez, M. Concheiro. "On the effect of surface roughness and material on the subcooled flow boiling of water: Experimental study and global correlation", *Experimental Thermal and Fluid Science,* vol. 64, pp. 114-124, February 2015.

[39] F. W. Dittus L. M. K. Boelter. "Heat Trasnfer in Automobile Radiators of the Tubular Type", *Int. Comm. Heat and Mass Transfer,* vol. 12, pp. 3-22, 1985.

[40] T.L Bergman, A.D Lavine, F.P Incropera, D.P Dewitt. "Fundamentals of heat and mass transfer", *John wiley songs,* seventh edition, pp. 662.

[41] Y. Katto, C. Kurata. "Critical heat flux of saturated convective boiling uniformly heated plates in parallel flow", *International Journal of multiphase flow,* vol. 6, pp. 575-582, 1980.

[42] N. Zuber."Film Boiling and the Minimum Film Boiling Point", *Trans. Am. Soc. Mech. Eng.*, vol. 80, pp. 711-720, 1958.

[43] P. J. Berenson. "Film-Boiling Heat Transfer From a Horizontal Surface", *International Journal of multiphase flow,* vol. 83, pp. 351-356, August 1961.

[44] Leidenfrost, J. G. "De Aquae Communis Nonnullis Qualitatibus Tractatus", Germany: Duisburgi ad Rhenum. 1756.

[45] R. Maurus, T. Sattelmayer. "Bubble and boundary layer behaviour in subcooled flow boiling", *International Journal of thermal sciences,* vol. 45, pp. 257-268, May 2004.

[46] P.Jayaramu, S. Gedupudi, S.K. Das. "An Experimental Investigation on the Influence of Copper Ageing on Flow Boiling in a Copper Microchannel", *Heat transfer engineering,* vol. 41, pp. 333-350, Jan 2019.

[47] M.C. Vlachou, J.S. Lioumbas, K. David, D. Chasapis, T.D. Karapantsios. "Effect of channel height and mass flux on highly subcooled horizontal flow boiling", *Experimental thermal and fluid science,* vol. 83, pp. 157-168, January 2017.

[48] K. Hata, N. Noda. "A general correlation for heat transfer during subcooled boiling in pipes", *ASHRAE TRANS,* vol. 83, pp. 202-217, January 1977.

[49] S.S. Papell. "Subcooled boiling heat transfer under forced convection in a heated tube", *NASA Technical Note D-1583, Lewis Research Center, Cleveland, OH,,* 1963.

[50] K. Hata, N. Noda. "Turbulent heat transfer for heating of water in a short vertical tubes", *J. Power Energy Syst,* vol. 1, pp. 318-329, January 2008.

[51] K. Hata, S. Masuzaki. "Critical heat fluxes of subcooled water flow boiling in a short vertical tube at high liquid Reynolds number", *Nucl. Eng. Des,* vol. 10, pp. 3145–3157, October 2010.

[52] P.K. Baburajan, G.S. Bisht, S.K. Gupta, S.V. Prabhu. "Measurement of subcooled boiling pressure drop and local heat transfer coefficient in horizontal tube under LPLF conditions", *Nucl. Eng. Des,* vol. 255, pp. 169–179, February 2013.

[53] J. Lee, I. Mudawar. "Fluid flow and heat transfer characteristics of low temperature two-phase micro-channel heat sinks Part 2. Subcooled boiling pressure drop and heat transfer", *Int. J. Heat Mass Transfer,* vol. 9, pp. 4327–4341, August 2008.

[54] W.M. Rohsenow. "Heat transfer with evaporation", *Proc. Heat Transfer—A Symposium Held at the University of Michigan During the Summer of 1952,* vol. 9, pp. 101–150, 1953.

[55] D. Butterworth. "The correlation of cross flow pressure data by means of a permeability concept", *UKAEA Report AERE-R9435,* 1979

[56] J.C. Chen. "Correlation for boiling heat transfer to saturated fluids in convective flow", *Ind. Eng. Chem. Process Des. Dev,* vol. 3, pp. 322-329, 1966.

[57] J. Yan, Q. Bi, Z. Liu, G. Zhu, L. Cai. "Subcooled flow boiling heat transfer of water in a circular tube under high heat fluxes and high mass fluxes", *Fusion Eng. Des,* vol. 100, pp. 406–418, 2015.

[58] K.E. Gungor, R.H.S. Winterton. "General correlation for flow boiling in tubes and annuli", *Int. J. Heat Mass Transfer,* vol. 100, pp. 351–358, 1986.

[59] S. Hua, R. Huang, Z. Li, P. Zhou. "Experimental study on the heat transfer characteristics of subcooled flow boiling with cast iron heating surface", *Appl. Therm.Eng,* vol. 77, pp. 180–191, February 2015.

[60] S.S. Kutateladze. " Boiling heat transfer", *Int. J. Heat Mass Transfer,* vol. 4, pp. 31–45, December 1961.

[61] Z. Liu, R.H.S. Winterton. "A general correlation for saturated and subcooled flow boiling in tubes and annuli, based on a nucleate pool boiling equation", *Int. J. Heat Mass Transfer,* vol. 34, pp. 2759–2766, November 1991.

[62] A.E. Bergles, W.M. Rohsenow. "Correlation of forced convection boiling heat transfer data", *Int. J. Heat Mass Transfer,* vol. 25, pp. 753–757, August 1964.

[63] R.W. Bjorg, G.R. Hall, W.M. Rohsenow. "The determination of forced-convection surface- boiling heat transfer", *Journal of Heat Transfer,* vol. 86, pp. 365–372, June 1982.

[64] W.H. McAdams, W.E. Kennel, C.S. Minden, R. Carl, P.M. Picornell, J.E. Dew. "Heat transfer at high rates to water with surface boiling", *Ind. Eng. Chem,* vol. 41, pp. 1945–1953, September 1942.

[65] W.H. Jens, P.A. Lottes. "Analysis of Heat Transfer, Burnout, Pressure Drop and Density Date for High-pressure Water", *Argonne National Lab. Report, ANL-4627,* May 1951.

[66] J.R.S. Thom, W.M. Walker, T.A. Fallon, G.F.S. Reising. " Boiling in subcooled water during flow up heated tubes or annuli", *Presented at the Symposium on Boiling Heat Transfer in Steam Generating Units and Heat Exchangers, Institute of Mechanical Engineers,* 1965.

[67] Y.S. Muzychka, M.M. Yovanovich. "Laminar forced convection heat transfer in the combined entry region of non-circular ducts", *J. Heat Transfer,* vol. 126, pp. 54-61, February 2004.

[68] J.R. Thome, V. Dupont, A.M. Jacobi. "Heat transfer model for evaporation in microchannels. Part I: presentation of the model", *Int. J. Heat Mass Transfer,* vol. 47, pp. 3375–3385, March 2004.

[69] S. Tzeng , W. Ma. "Experimental investigation of heat transfer in sintered porous heat sink", *Int. Commun. Heat Mass Transfer,* vol. 6, pp. 827–836, 2004.

[70] W. Gao , X. Xu , X. Liang. "Flow boiling of R134a in an open-cell metal foam mini-channel evaporator", *Int J Heat Mass Transfer,* vol. 126, pp. 103–115, April 2018.

[71] D. Deng , Y. Tang , D. Liang , H. He , S. Yang . “Flow boiling characteristics in porous heat sink with reentrant microchannels”, *Int J Heat Mass Transfer,* vol. 70, pp. 463–477, January 2014.

[72] D. Deng , L. Zeng, W.Sun. “A review on flow boiling enhancement and fabrication of enhanced microchannels of microchannel heat sinks”, *Int J Heat Mass Transfer,* vol. 175, 12332, May 2011.

[73] Z.G. Qu , Z.G. Xu , C.Y. Zhao , W.Q. Tao. “Experimental study of pool boiling heat transfer on horizontal metallic foam surface with crossing and single-directional V-shaped groove in saturated water”, *Int. J Multiphas Flow,* vol. 41, pp. 44–55, 2012.

[74] A. Jaikumar , S.G. Kandlikar. “Enhanced pool boiling heat transfer mechanisms for selectively sintered open microchannels”, *Int J. Heat Mass Transfer,* vol. 88, pp. 652–661, 2015.

[75] B. He , X. Luo , F. Yu , J. Zhou , J. Zhang. “Flow boiling characteristics in bi-porous minichannel heat sink sintered with copper woven tape”, *Int. J. Heat Mass Transfer,* vol. 158, 119988, May 2020.

[76] Y. Sun , L. Zhang , H. Xu , X. Zhong . “Flow boiling enhancement of FC-72 from microporous surfaces in minichannels”, *Exp. Therm. Fluid Sci,* vol. 35, pp. 1418–1426, 2011.

[77] Z.G. Xu , C.Y. Zhao. “Pool boiling heat transfer of open-celled metal foams with V-shaped grooves for high pore densities”, *Exp. Therm. Fluid Sci,* vol. 52, pp. 128–138, 2014.

[78] F. Yu, F. Li, B. Zhang, H. Li, L. Sun. “Efficient electrocatalytic water oxidation by a copper oxide thin film in borate buffer”, *American Chemical Society,* vol. 5, pp. 627-630, 2015.

[79] R. Svoboda, D.A Palmer. “Behaviour of Copper in Generator Stator Cooling-Water Systems”, *ICPWS XV,* Berlin, September 8–11, 2008

[80] M. Moliere, Y. Verdier, C. Leymonie. “Oxidation of copper in high purity water at 70 °C: Application to electric generator operator”, *Corrosion Science,* vol. 30, pp. 183-188, 1990.

[81] J. Kim, S. Jun, J. Lee, J. Godinez, S.M. You. "Effect of surface roughness on pool boiling heat transfer of water on a superhydrophilic aluminum surface", *Int. Journal of heat transfer,* vol. 139, pp. (101501)1-9, October 2017.

[82] K. Wang, N. Erkan, K. Okamoto. "Oxidation effect of copper on the downward-facing flow boiling CHF under atmospheric condition", *International Journal of Heat and Mass Transfer,* 000 (2020) 119866, April 2020.

[83] E.Santiago Galicia, Y. Otomo, K. Enoki. "The Effect of the Copper Oxidation on the Subcooled Flow Boiling Heat Transfer", *Japan Society of Refrigerating and Air Conditioning Engineers,* September 8-10, 2021 Tokyo Institute of Technology (Tokyo, Tech. Japan)

[84] TM Swagelok company. "An Installer's Pocket Guide for Swagelok", *available online,* https://www.swagelok.com/downloads/webcatalogs/en/ms-13-151.pdf

[85] Yokogawa Electric Corporation. *Data Acquisition System GM* https://www.yokogawa.com/

[86] E. W. Lemmon and and Ian H. Bell and M. L. Huber and M. O. McLinden. *NIST Standard Reference Database 23: Reference Fluid Thermodynamic and Transport Properties-REFPROP, Version 10.0, National Institute of Standards and Technology,* Standard Reference Data Program, Gaithersburg, 2018.

[87] Central Research Institute, Mitsubishi Materials Co., Ltd. *1-600 Kitabukurocho, Omiya, Saitama 330-0835, Japan* https://www.mmc.co.jp/corporate/en/index.html

[88] B.N Taylor, C.E Kuyatt. "Guidelines for Evaluation and Expressing the Uncertainty of NIST Measurement Results", *National Institute of Standards and Technology,* Gaithersburg, M.D, 1994.

[89] R. Watanabe, T. Kobayashi, Y.Otomo, A. Akisawa, Y. Ueda, K. Koji. "Experimental investigation into the heat transfer and pressure drop performance of sintered high porosity media", *Applied Thermal Engineering,* 196 (2021) 117284, July 2021.

[90] Hexagon, MSC Software corporation. *5161 California Ave. Suite 200 Irvine, CA 92617* https://www.mscsoftware.com/

[91] F. Krause, S. Schuttenberg, U. Fritsching. " Modeling and simulation of flow boiling heat transfer", *International journal of numerical method for heat & fluid flow,* vol. 20, pp. 312-331, July 2009.

[92] S. Lo, J. Osman. "CFD Modeling of boiling flow in PSBT 5x5 bundle", *Science and technology of nuclear installations,* vol. 2012, (795935), May 2012.

[93] X. Yuan, L. Yang, Z. Tian, S. Han, H. Lu. "Numerical simulation of flow boiling in small channel of plate OTSG", *Frontiers in energy research,* 7:161

List of Publications

Journal paper:

1. **Edgar Santiago Galicia**, Yusuke Otomo, Toshihiko Saiwai, Kenji Takita, Kenji Orito, Koji Enoki. "Subcooled Flow Boiling Heat Flux Enhancement Using High Porosity Sintered", *Applied Sciences*, Vol. 11, 5883, 2021 **DOI**: 10.3390/app11135883

International conference papers:

1. **Edgar Santiago Galicia**, Otomo Yusuke, Yaningshi Indri, and Koji Enoki "Critical heat flux enhancement using a high porosity sintered fiber attached on the heated surface ," in *The 31st International Symposium on Transport Phenomena*, 13-16 October 2020, Honolulu USA.

2. **Edgar Santiago Galicia**, Yusuke Otomo, and Koji Enoki. "Effect of mass flux on high porosity sintered fiber on subcooled flow boiling," in *The 2nd ASEAN-UEC Workshop on Energy and AI*, 21 November 2020, Bandung, Indonesia.

3. **Edgar Santiago Galicia**, Kosuke Kumatori, Yusuke Otomo, and Koji Enoki. " The Effect of the High Porosity Sintered Fiber on the Surface in Subcooled Boiling Heat Transfer Enhancement," in *GL 2020 14th IIR-Gustav Lorenzen Conference on Natural Refrigerants*, 7-9 December 2020, Kyoto **DOI**: 10.18462/iir.gl.2020.1193

Other publication:

1. **Edgar Santiago Galicia**, Yusuke Otomo, and Koji Enoki. "The Effect of the Copper Oxidation on the Subcooled Flow Boiling Heat Transfer" in 2021 年度日本冷凍空調学会年次大会 , Tokyo, Japan, 2021, September 10.